

# Synthesis, Characterization and Application of ZnO Nanomaterials

A Dissertation  
Presented to  
The Academic Faculty

by

Wenjie Mai

In Partial Fulfillment  
of the Requirements for the Degree  
Doctor of Philosophy in the  
School of Materials Science and Engineering

Georgia Institute of Technology  
May 2009

# Synthesis, Characterization and Application of ZnO Nanomaterials

Approved by:

Dr. Zhong Lin Wang, Advisor  
School of Materials Science and  
Engineering  
Georgia Institute of Technology

Dr. Ching-Ping (C.P.) Wong  
School of Materials Science and  
Engineering  
Georgia Institute of Technology

Dr. C.F. Jeff Wu  
School of Industrial and Systems  
Engineering  
Georgia Institute of Technology

Dr. Robert L. Snyder  
School of Materials Science and  
Engineering  
Georgia Institute of Technology

Dr. Kenneth A. Gall  
School of Materials Science and  
Engineering  
Georgia Institute of Technology

Date Approved: [March 30, 2009]

To my entire family

# ACKNOWLEDGEMENTS

I would like to express my deepest love, respect, and admiration to my entire family for their unconditional support, understanding, and dedication throughout these years. My grandparents were high school and primary school teachers. They poured their love and time to me after their retirement, took good care of me and guided me through my youth. My parents provided the best education opportunities that they could offered, and thus, I had never need to worry about anything besides study with all their support until I left my motherland China to US for higher education.

I also would like to thank my advisor Professor Zhong Lin Wang for his guidance and support. During the Ph.D. period, I had been through numerous difficulties. I had felt frustrated, and I had felt depressed. Without Professor Wang's encouragements and helps, I would not have been able to come to this moment. The impact of Professor Wang's attitude and devotion to science on me will be far-reaching.

Furthermore, my group members had been always friendly and helpful. We studied together in classes and collaborated together in lab in the past several years. I would say this lab is the most pleasant place that I have even work at, and the lab mates are the friendliest persons I have even live with. Wish our friendship lasts forever.

Last but not least, I would like to thank my wife. She always wants to stay with her family and friends, but still she made a difficult decision, came to US right after her graduation and has been taking good care of me even since. Having her love and supports means invaluable to me.

# TABLE OF CONTENTS

	Page
ACKNOWLEDGEMENTS .....	iv
LIST OF TABLES .....	viii
LIST OF FIGURES .....	ix
SUMMARY .....	xvi
CHAPTER 1 INTRODUCTION .....	1
1.1 Nanoscience and Nanotechnology .....	1
1.1.1 History .....	1
1.1.2 One-Dimensional Nanomaterials .....	1
1.2 Research on ZnO Nanomaterials .....	2
1.2.1 Basic Properties of ZnO .....	2
1.2.2 Synthesis and Characterization of ZnO Nanomaterials .....	3
1.2.3 Mechanical Properties of ZnO Nanowires .....	5
1.2.4 Electrical Properties of ZnO Nanowires .....	6
1.2.5 Optical Properties of ZnO Nanowires .....	8
1.2.6 Field Effect Sensing Properties of ZnO Nanowires .....	12
1.2.7 Electromechanically-Coupled Nanodevice Theory .....	13
CHAPTER 2 SYNTHESIS OF NANOMATERIALS .....	18
2.1 High Temperature Vapor Deposition Method .....	18
2.1.1 Experimental Setup .....	18
2.1.2 Underlying Mechanism .....	23

2.1.3 Vertically-Aligned Nanowire Arrays on SiC and GaN substrates.....	25
2.1.4 Randomly-Oriented Nanowires .....	31
2.1.5 Superlattice-Structured Nanohelices.....	33
2.2. Low Temperature Wet Chemical Method .....	37
2.2.1 Procedure of Experiment .....	37
2.2.2 Approaches to Controlled Growth.....	40
CHAPTER 3 MANIPULATION METHODS .....	43
3.1 Electron Beam Lithography.....	43
3.2 Dielectrophoresis .....	44
3.3 Direct Manipulation Technique .....	45
3.3.1 Example 1: Manipulation and Mechanical Measurement on Silicon Nanowires .....	49
3.3.2 Example 2: Electrical Measurement on ZnO Tetrapod Nanostructures .....	57
CHAPTER 4 MACHANICAL PROPERTIES OF NANOHELICES.....	62
4.1 Motivation.....	62
4.2 Young's Modulus Measurements .....	63
4.3 Fracture Mechanism.....	69
4.4 Super-elasticity .....	73
CHAPTER 5 QUANTIFYING ELASTIC DEFLECTION OF BRIDGED NANOWIRES .....	78
5.1 Motivation.....	78
5.2 Experimental Details.....	79
5.3 Physical Modeling .....	83

5.4 Discussions .....	85
5.5 Statistical Adjustment for Better Estimation .....	90
CHAPTER 6 ELECTRICAL PROPERTIES AND DEVICE APPLICATIONS OF BRIDGED NANOWIRES.....	95
6.1 Enhanced Electrical Properties of ZnO Nanowires .....	95
6.2 UV Sensors .....	102
6.3 Strain Sensors.....	105
CHAPTER 7 CONCLUSION.....	114
REFERENCES .....	116

# LIST OF TABLES

	Page
Table 1: Electrical nature of ideal MS contacts .....	8
Table 2: Calculated effective spring constant on different circles of nanohelices. ....	69
Table 3: Characteristic parameters of nanohelix used for transverse fracture measurements by AFM. ....	72
Table 4: Elastic modulus derived from the two models as a function of deviation in defining the true middle point along the suspended portion of the NB. ....	89
Table 5: Comparison of estimators from the previous FFBM and the new SPAR.....	93



# LIST OF FIGURES

	Page
Figure 1: ZnO wurtzite crystal structure.....	3
Figure 2: A collection of ZnO nanostructures. (a) nanobelts, (b) nanohelices, (c) nanorings, (d) nanowire array.....	4
Figure 3: In-situ TEM on a ZnO nanobelt at (a) stationary, (b) the first harmonic resonance in x direction, and (c) the first harmonic resonance in y direction. (d) An enlarged image of the nanobelt and its electron diffraction pattern (inset). (e) The FWHM of the resonance peak measured from another ZnO nanobelt. <sup>27</sup> .....	6
Figure 4: (a) An AFM image of a ZnO nanobelt after nanoindentation experiment. (b) Nanoindentation experiments indicate that hardness of ZnO nanobelts is $\sim 5$ GPa. <sup>28</sup> .....	6
Figure 5: Photoluminescence (PL) spectra acquired from an aligned ZnO nanowires arrays as a function of the angle between the detector and a direction normal to the substrate. The inset shows the experimental setup. <sup>35</sup> .....	9
Figure 6: (a) Photoconduction in a ZnO nanowires photodetectors. (a) Schematic of the photodetector. Upon illumination with photon energy above $E_g$ , electron-hole pairs are generated and holes are readily trapped at the surface. Under an applied electric field, the unpaired electrons are collected at the anode, which leads to the increase in conductivity. (b and c) Trapping and photoconduction mechanism in ZnO nanowires: the top drawing in (b) shows the schematic of the band diagrams of a nanowires in dark, indicating band-bending and surface trap states. VB and CB are the valance band and conduction band, respectively. The bottom drawing shows oxygen molecules adsorbed at the nanowires surface that capture the free electron present in the n-type semiconductor forming a low-conductivity depletion layer near the surface. (c) Under UV illumination, photogenerated holes migrate to the surface and are trapped, leaving behind unpaired electrons in the nanowires that contribute to the photocurrent. In ZnO nanowires, the lifetime of the unpaired electrons is further increased by oxygen molecules desorption from the surface when holes neutralize the oxygen ions. <sup>36</sup> .....	10
Figure 7: (a) I-V characteristics of a single nanowires photodetector as a function of light intensity; from top to bottom, the curves were measured at the following intensity: $4 \times 10^{-2}$ W/cm <sup>2</sup> (black), $4 \times 10^{-3}$ W/cm <sup>2</sup> (red), $4 \times 10^{-4}$ W/cm <sup>2</sup> (green), $1.3 \times 10^{-4}$ W/cm <sup>2</sup> (blue), $4 \times 10^{-5}$ W/cm <sup>2</sup> (cyan), $1.3 \times 10^{-5}$ W/cm <sup>2</sup> (magenta), $6.3 \times 10^{-6}$ W/cm <sup>2</sup> (yellow), and in dark (brown). Inset is the SEM image of a typical ZnO nanowires device (obtained at 45° tilted angle); the spacing between the interdigitated electrodes is 2 $\mu$ m. (b) The I-V curves presented in (a) are replotted on a natural logarithmic scale. <sup>36</sup> .....	11

Figure 8: (a) I-V characteristics from single ZnO nanowire in dark and under illumination from a 366nm Hg lamp. (b) Time dependence of photocurrent as the 366nm light source is modulated. <sup>37</sup>	12
Figure 9: (a) AFM image of a ZnO nanobelt based FET. (b) Schematic of the FET. <sup>39</sup>	13
Figure 10: Source-drain current versus gate bias for a ZnO FET in ambient. <sup>39</sup>	13
Figure 11: (a) Aligned ZnO nanowire array grown on Al <sub>2</sub> O <sub>3</sub> substrates. (b) AFM output voltage image of nanowire array. (c) Experimental setup and procedures for generating electricity by deforming a ZnO nanowire with a conductive AFM tip. (d) Line profiles from the topography (red) and output voltage (blue) images across a nanowire. <sup>8</sup>	15
Figure 12: Current variation with a continuous releasing and bending process of the ZnO nanowire; insets are the three typical bending cases in stage I, II, and III, respectively. (b, c) SEM images of the contacting point between the ZnO nanowire tip and the tungsten needle surface when the nanowire was bent and released. (d) A finite element simulation of the strain distribution along the ZnO nanowire when it is bent. (e) The carrier trapping effect. (f) The creation of a charge depletion zone. <sup>44</sup>	17
Figure 13: Schematic of the tube furnace.	18
Figure 14: Temperature profile measured inside the alumina tube furnace (from the center to the outside of the furnace) for different source temperatures (1475 °C, 1400 °C, 1300 °C, 1100 °C, 950 °C, and 800 °C).	21
Figure 15: Schematic of gas and pressure control system.	23
Figure 16: (a, b) The growth frond/end of ZnO nanobelts, showing no visible catalytic particles at the ends. (c-g) A possible vapor-solid growth process for the formation of nanobelt. <sup>46</sup>	24
Figure 17: (a) 30° tilted and cross-sectional SEM images of vertically aligned ZnO nanowires arrays grown on SiC (0001) substrate with 1μm scale bar; (b) 30° tilted and cross-sectional SEM images of vertical aligned ZnO nanowire arrays grown on GaN (0001) substrate with 1μm scale bar; (c) TEM image of a ZnO nanowire grown along (0001) direction with Au catalyst sphere, and the inset shows the corresponding TEM diffraction pattern; (d) x-ray diffraction pattern of the same sample in (a), and the inset is EDS analysis.	28
Figure 18: (a) Temperature distribution, (b) percentage of vertical aligned nanowires, (c) length distribution, (d) diameter distribution, (e) aspect ratio distribution of sample A-F, and (f) growth speed derived from length vs. time relationship.	30
Figure 19: (a) The SEM image shows nanawalls connecting individual vertically aligned nanowire; (b) the TEM image and diffraction pattern of a triangular nanosheet, which is	

the early stage of nanowalls; (c) schematic diagram demonstrating the growth mechanism of nanowalls. ....	31
Figure 20: Randomly oriented ZnO nanowires grown on (a) Si, (b) polycrystalline Al <sub>2</sub> O <sub>3</sub> , (c) SiC and (d) GaN substrates. ....	32
Figure 21: Typical SEM image of the left- and right-handed ZnO nanohelices. ....	34
Figure 22: TEM images of ZnO nanohelices.....	36
Figure 23: Detailed structural analysis of ZnO nanohelices.....	36
Figure 24: Thickness and width change at the joining interface between initial nanoribbon and the nanohelix. ....	37
Figure 25: cage-like structure Haxamine.....	38
Figure 26: (a) Equal amount of Zinc Nitrate and Haxamine are mixed in DI water. (b) Substrate with seed layer is placed face down on mixture solution surface. (c) Beaker is transferred to box furnace and heated up to 70-90°C. (d) ZnO nanowires nucleate and grow on the seed layer at elevated temperature. ....	39
Figure 27: (a) low and (b) high magnification of ZnO nanowires on Si substrate. (c) low and (d) high magnification of ZnO nanowires on fluorine doped tin oxide (FTO) glass. ....	39
Figure 28: Two different patterning schemes. (a) is characterized with patterned individual Au features. (b) is characterized with patterned PMMA hollow features that are exposing the corresponding features on a layer of Au underneath. ....	41
Figure 29: Patterned individual Au features on Si substrate. Features are 100nm diameter Au circles with 1µm distance.....	41
Figure 30: (a) Vertical view and (b) tilted view of the patterned growth of nanowire arrays on GaN substrate without seed layer. <sup>61</sup> .....	42
Figure 31: schematic diagram of the EBL procedures. <sup>63</sup> .....	44
Figure 32: Schematic of the dielectrophoresis process. <sup>63</sup> .....	45
Figure 33: Photo of Nova dual beam focus ion beam machine.....	46
Figure 34: Photo of the micro-manipulator and the control electronic system from Kleindiek.....	46
Figure 35: Controller and 4 probe manipulator system S100 from Zyvex.....	47

Figure 36: Schematic of transferring a single nanowire from sample substrate to between two electrodes. ....	48
Figure 37: TEM image of the SiNW with a 5-10 nm native oxide layer (scale bar 100nm). Inset: Selected area electron diffraction pattern.....	50
Figure 38: Schematic diagram illustrating the experimental setup before (a) and after (b) the manipulation.....	51
Figure 39: a-f) A series of snapshot SEM images showing the continuous buckling of the SiNW. g) Corresponding curve of the applied force $F$ vs. change in chord length $ L-L_0 $ when the NW was buckled. h) Calculated stress-strain curve of the buckling of the NW. Inset: Schematic diagram of the deformation approximation.....	52
Figure 40: A comparison of the experimental results and the calculated curve of strain vs. change in chord length $ L-L_0 $ . Inset: schematic model of the nanowire under buckling. The calculation was carried out for the middle point of the chord: $I = L_0/2$ .....	54
Figure 41: Plot of the critical $P_{cr}$ vs. $I_0/L^2$ for several NWs that have been manipulated. ....	55
Figure 42: a) Schematic diagram illustrating the principle of bending and the setup. b-f) A series of snapshot SEM images showing the manipulation and deflection of a SiNW. g) Corresponding force-deflection distance curve of the NW. ....	56
Figure 43: ZnO tetrapod nanostructures were dispersed on a clean 200nm-SiO <sub>2</sub> coated Si substrate. ....	58
Figure 44: (a) three tungsten probes were directly placed on three legs of a ZnO tetrapod nanostructure, respectively. (b) the three legs had been modified by FIB-induced deposition of a 200 nm thick Pt, and three tungsten probes were placed on the Pt pads connecting to the legs of the tetrapod nanostructure. ....	59
Figure 45: A typical I-V curve obtained by directly placing tungsten probes on a ZnO tetrapod nanostructure.....	60
Figure 46: Three I-V curves measured at ZnO/Pt/W contacts.....	60
Figure 47: $I_2$ - $V_2$ curves when $V_1$ remains 0V and $V_3$ follows -0.10, -0.05, 0, 0.05, 0.10V steps.....	61
Figure 48: Schematic of the AFM. ....	64
Figure 49: Typical calibrated sensitivity measurement curves on silicon substrate (blue) and ZnO nanohelix (red).....	67

Figure 50: Manipulation of a nanohelix and measurement of its elastic properties. (A) SEM image of a nanohelix that was cut by a FIB microscope shows the preservation of the rigid geometrical shape after the cut, which suggests there is minimal stored elastic energy. (B) AFM contact mode measurement of the sensitivity ( $S$ ) of the photodetector for the silicon substrate and the four turns of a ZnO nanohelix, as indicated by 1 to 4 in the inserted AFM image. The sensitivity  $S$  of the photodetector is the inverse of the slope of the voltage-extension curve, which is directly related to the elastic property. The measurement was done by positioning the tip on the surface of the upmost middle point of the turn of the helix. Each dot represents one measurement. The sensitivity  $S_{Si}$  for silicon is substantially lower than that for the ZnO nanohelix ( $S_{Helix}$ ). (C) Fracture of the nanohelix at two consecutive turns of the nanohelix by the AFM tip, showing a preservation of helical shape in the sectioned region. .... 68

Figure 51: AFM images of the same nanohelix (a) before and (b) after fracture. Scale bar indicates 400nm. .... 70

Figure 52: Two-step fracture process of nanohelices upon transversal compression by an AFM tip. a) and b) are, respectively, an AFM topography image after the tip-induced fracture over a nanohelix and the corresponding SEM image of the fractured part. (c) Force displacement curves for 7 nanohelices recorded during AFM tip compression and fracture process. (d) A schematic model of the two-step fracture process of the nanohelix upon transverse compression by an AFM tip. .... 71

Figure 53: Manipulation process of a nanohelix upon an extremely large axial stretching and shape-recovery process. The nanohelix was deposited on silicon substrate. (a) One end of a nanohelix was welded with Pt onto a tungsten nanoprobe. (b) An attempt for extracting the welded nanohelix out of the entangled nanohelices. (c) An enlarged SEM image showing the extremely stretched nanohelix. (d) Continued extraction led to an initial release of the welded nanohelix from the entangled point and a recovery of the nanohelix shape. (e) A complete restoring of the nanohelix shape after the manipulation in b and c, suggesting a superelasticity (shape memory) behavior. .... 75

Figure 54: Compressed deformation process of a nanohelix induced by the nanoprobe. The compression-led shortening and twisting are indicated by arrowheads, starting from (a) a half-turn of the nanohelix; (b) one and half turns; (c) two turns; and (d) two and a half turns. (e) The nanohelix elastically jumped away from the contact point with the other end free because of an overload by the probe. (f) The nanohelix eventually restored its original shape, suggesting an elastic deformation during the compression. .... 76

Figure 55: (a) Low-magnification SEM image of a silicon substrate with parallel trenches. Long nanobelts (NBs) are lying on the trenches. (b) SEM image of one NB bridged over a trench (c) and the corresponding AFM image of the bridged NB over the trench. (d) The corresponding SEM image of the same NB in (b) after depositing Pt pads at the two ends. .... 80

Figure 56: (a) As-received AFM image profiles of one suspended NB under different load forces in contact mode. (b) The normalized AFM image profile after removing the surface roughness by subtracting the image acquired at 106 nN from the data in (a). The force is also normalized in reference to the “zero setting point” of 106 nN.....	82
Figure 57: Schematic diagrams of the (a) clamped-clamped beam model (CCBM) and (b) the free-free beam model (FFBM).....	84
Figure 58: (a) Curve fitting using the CCBM and FFBM for the image profiles of NB 1 acquired under normalized force of 183 nN. (b) The bending modulus from the FFBM fitted curves under different load forces. The error bars are introduced with consideration of the uncertainty in curve fitting. The dimensions of NB 1 are 1.270 $\mu\text{m}$ in length, 90 nm in width, and 70 nm in thickness; the dimensions of NB 2 are 1.253 $\mu\text{m}$ in length, 115 nm in width, and 95 nm in thickness; and the dimensions of NB 3 are 1.232 $\mu\text{m}$ in length, 125 nm in width, and 115 nm in thickness. ....	88
Figure 59: Another set of deflection curves with large deviation.....	92
Figure 60: (a) Curve fitting results with only FFBM. (b) Curve fitting results with the SPAR model, which introduces the statistical approach to capture the bias/noise.....	93
Figure 61: (a) The SEM image of the nanowire bridging between two electrodes; inset is the overall image of nanowire device after the Pt deposition by FIB. (b) The I-V curve obtained before the Pt deposition. (c) The I-V curve obtained after the Pt deposition.....	97
Figure 62: Schematic diagrams of molecules: MBA, ODT and MDA.....	98
Figure 63: Procedure of SAM coating.....	99
Figure 64: (a) Contact angle measurement of the SAM coated Au surface. (b) FT-IR results of the simulated experiment, confirming the bonding between SAM and ZnO nanowires. ....	100
Figure 65: Histogram of the conductance of the devices, which shows the MDA and ODT treated samples have a better electrical conductivity than the control samples.....	101
Figure 66: Perfect linear Ohmic behavior of the nanowire with Pt deposition on both ends. ....	102
Figure 67: UV sensing properties of the Ohmic type device.....	103
Figure 68: (a) Original and (b) normalized UV sensing properties of the Schottky back-to-back ZnO nanowire devices. ....	105
Figure 69: (a) Schematic of a single ZnO PFW based strain sensor device. (b) Optical image of a strain sensor. (c) Schematic of the measurement system to characterize the	

performance of the strain sensor. (d) Proposed electric circuit diagram for the strain sensor. .... 109

Figure 70: (a) Typical I-V characteristics of the strain sensor at different strain. (b) Logarithm plot of the current under positive bias by using the data in (a)..... 110

Figure 71: Energy band diagram illustrates the asymmetric Schottky barrier heights at the source and the drain contacts of a PFW, where the offset by the applied drain-source voltage  $V$  was not included for easy discussion. (b) Fitting the  $\ln I$ - $V$  data using the thermionic emission – diffusion theory at a given strain for a reversely biased Schottky barrier. The black dotted are experimental data points from Figure 70(a) for stain=0, and the red line is the theoretical fit. (c) The derived change in SBH based on the thermionic emission – diffusion model, as a function of strain at a drain-source bias of  $V=1.5V$  and  $2.0V$ , respectively. (d) Logarithm plot of the current (in unit of A) at fixed bias of  $V=1.5V$  and  $2.0V$  as a function of strain. .... 113

# SUMMARY

One-dimensional (1-D) nanomaterials have drawn a lot of attention because of their novel and unique properties and a wide range of applications. ZnO nanomaterials are among the most important 1-D nanomaterials due to their semiconductive, piezoelectric, and biocompatible properties. In addition, ZnO exhibits a wide range of morphologies such as nanowires, nanobelts, nanorings, nanohelices, which are potential building blocks for fabricating nanodevices.

In this thesis, high temperature vapor deposition method has been extensively used to synthesize nanomaterials. One of the as-synthesized nanostructures is superlattice-structured nanohelix, which is made of two types of alternating and periodically distributed long crystal strips. The manipulation of the nanohelix showed super-elasticity and special fracture mechanism, suggesting possible applications in micro-electro-mechanical systems (MEMS) and nano-electro-mechanical systems (NEMS). The other widely studied nanomaterial is vertically aligned ZnO nanowire array, which is epitaxially grown on GaN and SiC substrates. Several manipulation methods such as e-beam lithography (EBL), dielectrophoresis, and in situ direct manipulation, have been developed, so that the mechanical and electrical properties of a single nanowire can be characterized, which provide essential references for fabricating bridged nanowire based MEMS/NEMS devices. Specifically, an improved atomic force microscope (AFM) based method has been developed to accurately measure the elastic modulus of bridged ZnO nanowires. Bridged nanostructure is an extremely important configuration in planar MEMS/NEMS devices and this new approach provides insights to



the importance of boundary conditions. Novel physical and statistical models have been firstly developed to obtain better estimate of elastic modulus. For electrical properties of bridged nanowires, it is found that the direct contact of ZnO nanowire and Au electrodes displays a back-to-back Schottky behavior. Self-assembled monolayer (SAM) can improve the mechanical contact and tune the work function of metal electrode to a small extent, thus increase the contact area and lower the barrier height, in turn increase the conductance. These devices with Schottky contacts show much better UV sensing performance than the ones with Ohmic contacts. Barrier height change is believed to play an important role in a lot of sensors. A thermionic emission-diffusion model is deduced to successfully explain the current change in a strain sensor.

This thesis clearly exhibits the unique properties of ZnO nanomaterials and provides deeper understanding to methodologies as well as the phenomena. With further exploration, ZnO nanomaterials should be able to be better understood and utilized, and come close to the next step of commercialization.

# **CHAPTER 1**

## **INTRODUCTION**

### **1.1 Nanoscience and Nanotechnology**

#### **1.1.1 History**

The concept of nanoscience and nanotechnology was firstly introduced since the Nobel Price Winner Richard Feynman's talk "There's plenty of room at the bottom" at Caltech on December 29, 1959. He described a process by which the ability to manipulate individual atoms and molecules might be developed, using one set of precise tools to build and operate another proportionally smaller set, so on down to the needed scale. About 20 years later, people finally obtained the ability to realize Feynman's prediction and started the new era of nanoscience and nanotechnology with the invention of the scanning tunneling microscope (STM) and high resolution transmission microscope (HRTEM), which led to the discovery of fullerenes in 1985 and carbon nanotubes (CNT) in 1991.<sup>1, 2</sup> In another development, the synthesis and properties of semiconductor nanomaterials including quantum dots and nanowires are widely studied, and numerous breakthroughs and achievements in nanoscience and nanotechnology have been made.<sup>3-10</sup>

#### **1.1.2 One-Dimensional Nanomaterials**

Since the start of studying carbon nanotubes (CNTs)<sup>2</sup>, people have realized that one-dimensional (1-D) nanomaterials could exhibit dramatically different or enhanced

properties than bulk materials. For example, CNTs are found to be the strongest and stiffest materials on earth so far, in terms of tensile strength and elastic modulus respectively, and both are about 10 times larger than those of stainless steel.<sup>11-13</sup> 1D nanomaterials are believed to be the promising building blocks for Micro-Electro-Mechanical systems (MEMS) and future Nano-Electro-Mechanical systems (NEMS). In order to pave the path for further industrial applications, the need to characterize the physical, chemical, and other properties of 1-D nanomaterials becomes urgent and important in current research.

## **1.2 Research on ZnO Nanomaterials**

### **1.2.1 Basic Properties of ZnO**

ZnO is one of the most important nanomaterials that have been widely studied. The crystal structure of ZnO at nanoscale is wurtzite structure with lattice parameters of  $a=0.3296\text{nm}$  and  $c=0.52065\text{ nm}$  (see Figure 1). It is composed of a number of alternating planes with tetrahedrally-coordinated  $\text{O}^{2-}$  and  $\text{Zn}^{2+}$  ions, stacked alternately along the  $c$ -axis. Along the  $c$ -axis, the positively charged Zn-(0001) polar surface and negative charged O-(000 $\bar{1}$ ) polar surface are the strongest polarity surfaces. The polar surfaces contribute to the variety of ZnO nanostructures by surface reconstruction to maintain a stable structure. When a stress force is applied, the non-central symmetric structure will lead to the separation of the central point of positive charges and that of negative charges, resulting in a polarization. This is called piezoelectricity, a significant property of ZnO. Furthermore, ZnO is an important semiconductor with a large direct band gap of 3.37 eV.

Due to the difference in the work functions  $\Phi$  between contact metal and ZnO, the ZnO nanowire-based devices can operate as Ohmic or Schottky devices. The nanowire-based nanogenerators and force sensors that were discovered in 2006 can be explained by the coupling effect of piezoelectric and semiconducting properties.<sup>8, 14</sup> All these predominant properties make ZnO a great potential in the applications of nanoscience and nanotechnology.

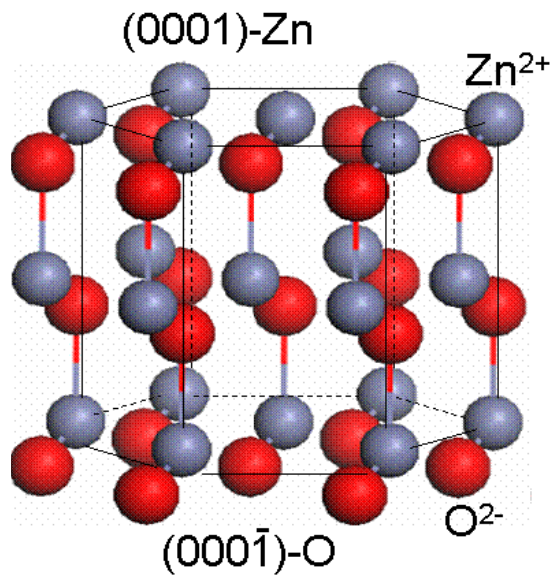


Figure 1: ZnO wurtzite crystal structure.

### 1.2.2 Synthesis and Characterization of ZnO Nanomaterials

Since the discovery of nanobelt in 2001, ZnO nanostructures (see Figure 2) have been commonly prepared by a high temperature furnace method. By precisely controlling the pressure, flow rate, temperature and synthesis time, a wide variety of ZnO nanostructures can be synthesized at the substrates at the downstream of the tube furnaces.

Transmission electron microscopy (TEM) experiment shows that ZnO has three fast growth directions:  $\langle 0001 \rangle$ ,  $\langle 01\bar{1}0 \rangle$  and  $\langle 2\bar{1}\bar{1}0 \rangle$ , and two  $\pm(0001)$  polar-surfaces.

A variety of unusual structure configurations can be synthesized under different growth conditions such as nanowires<sup>15</sup>, nanobelts<sup>16</sup>, nanopropellers<sup>17</sup>, and nanocombs<sup>18</sup>. In order to minimize the total energy, which is composed of elastic energy and electrostatic energy, nanobows<sup>19</sup>, nanohelices<sup>20-22</sup>, nanorings<sup>23</sup> could be the favorable morphology of ZnO at nanoscale.

This research will just focus on the quasi 1-D nanomaterials including nanowires, nanobelts, and nanohelices. Nanobelts have a rectangular cross-section, which is a result of the minimization of surface elastic and electric energies. Though from crystallographic point of view, nanobelts are different with the common nanowires, which have a circular or hexagonal cross-section and a different growth direction, they have similar physical and chemical properties, thus sometimes they are not distinguished in my research.

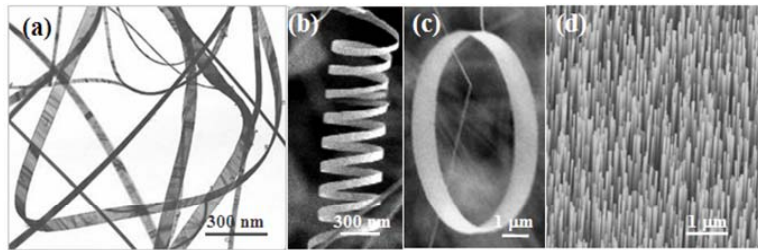


**Figure 2: A collection of ZnO nanostructures. (a) nanobelts, (b) nanohelices, (c) nanorings, (d) nanowire array.**

Recently, the research focus has been placed on the synthesis of vertically aligned nanowire arrays and their application as high density electronic devices and energy transducers. Currently, the aligned ZnO nanowires have been achieved by various methods, such as vapor-solid-solid process<sup>24</sup>, metal-organic chemical vapor deposition (MOCVD)<sup>25</sup>, and sol-gel process<sup>26</sup>.

### **1.2.3 Mechanical Properties of ZnO Nanowires**

Elastic modulus of 1-D nanomaterials is one of the most important properties that dictate their applications in nanotechnology. The elastic constants reflect the stress-strain relation of materials. Strictly speaking, because materials are normally anisotropic and properties of a material depend on direction, the elastic constant of material is a 4th rank tensor. For simplicity, the ZnO nanowires can be regarded as a homogeneous isotropic material, and a scalar constant Young's modulus (or elastic modulus) is used to indicate the elasticity of the material.

Various methods have been developed for quantifying the mechanical properties of 1-D nanomaterials. One of the most popular approaches is based on dynamic resonance of a 1-D nanostructure that is affixed at one end and free at the other; the mechanical resonance is excited by an externally applied oscillating electrical field, and the observation is made through electron microscope.<sup>11</sup> Previous research based on this in-situ TEM resonance method (see Figure 3) has measured the Young's modulus of ZnO nanobelts to be ~52 GPa.<sup>27</sup> Also, the hardness has been determined to be ~5 GPa from nanoindentation experiments (see Figure 4).<sup>28</sup> This thesis further investigates the mechanical measurements on 1-D ZnO nanomaterials, and serves as the first step to electromechanical measurements and applications.

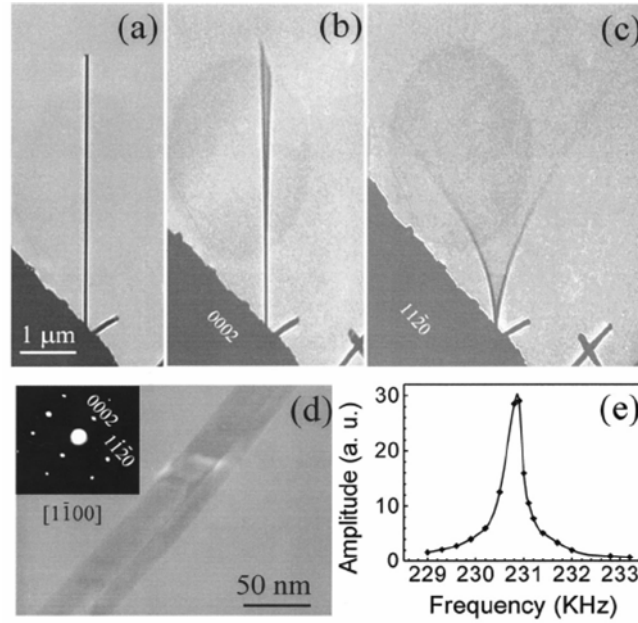


**Figure 3:** In-situ TEM on a ZnO nanobelt at (a) stationary, (b) the first harmonic resonance in x direction, and (c) the first harmonic resonance in y direction. (d) An enlarged image of the nanobelt and its electron diffraction pattern (inset). (e) The FWHM of the resonance peak measured from another ZnO nanobelt.<sup>27</sup>

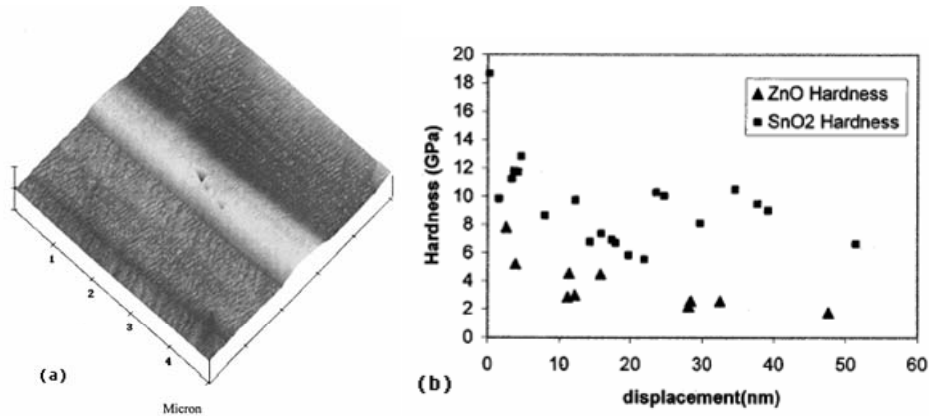


**Figure 4:** (a) An AFM image of a ZnO nanobelt after nanoindentation experiment. (b) Nanoindentation experiments indicate that hardness of ZnO nanobelts is  $\sim 5$  GPa.<sup>28</sup>

### 1.2.4 Electrical Properties of ZnO Nanowires

Normally, ZnO is an n-type semiconductor, which means electrons are the main carrier charges. The frequently observed unintentional *n*-type conductivity has often been

attributed to oxygen vacancies and zinc interstitials. One oxygen vacancy or zinc interstitial is always accompanied by two electrons in order to keep the charge balance.  $O_O^x \leftrightarrow \frac{1}{2}O_2(g) + V_O^{\bullet\bullet} + 2e'$  and  $Zn_O^x \leftrightarrow Zn_i^{\bullet\bullet} + 2e'$ . Different synthesis methods for ZnO nanowires will induce different levels of oxygen vacancies and zinc interstitials so that the conductivity of ZnO nanowires will vary. It is still controversial which kind of defects dominates in contributing electron carriers since the point defects are hard to directly observe.

One main issue related to electrical transport of ZnO nanowires is the complicity in the contact between the ZnO and electrode.<sup>29</sup> The metal-semiconductor (MS) contact plays a very important role in all solid-state devices. Two kinds of contacts can be formed at metal-semiconductor junction, one is Ohmic contact, and the other is Schottky contact. An Ohmic contact is a region on a semiconductor device that has been prepared so that the current-voltage (I-V) curve of the device is linear and symmetric. If the I-V characteristic is non-linear and asymmetric, the contact can instead be termed a Schottky contact. Reliable and controllable rectifying electric characteristics are essential in solid-state circuits.

Under ideal MS contact conditions, the intrinsic character of the contact is determined by the type of semiconductor and the difference between the work functions  $\Phi$  of metal and semiconductor. The ideal contact has the following properties<sup>30</sup>: (1) the metal and semiconductor are assumed to be in intimate contact on an atomic scale; (2) there is no interdiffusion or intermixing of the metal and the semiconductors; (3) there are no adsorbed impurities or surface charges at the interface. The electrical nature of ideal MS contacts is listed in Table 1.<sup>30</sup>



**Table 1: Electrical nature of ideal MS contacts**

	n-type Semiconductor	p-type Semiconductor
$\Phi_M > \Phi_S$	Schottky	Ohmic
$\Phi_M < \Phi_S$	Ohmic	Schottky

The work function  $\Phi$  of n-type ZnO is 4.53 eV. According to Table 1, the contact between ZnO and Au ( $\Phi=5.1$  eV) or Pt ( $\Phi=6.1$  eV) has Schottky behavior, while the contact between ZnO and Ti ( $\Phi=3.9$  eV), Ag ( $\Phi=4.2$  eV) or Al ( $\Phi=4.2$  eV) has Ohmic behavior.

Both kinds of contacts are important to modern microelectronic industry and the main challenge is to produce reliable and repeatable electronic devices. After achieving reliable Ohmic devices, by alternating the electric field of ZnO nanowire surfaces, ZnO can work as a field-effect transistor (FET), being able to detect the different gases, cells, viruses.<sup>31-34</sup>

### 1.2.5 Optical Properties of ZnO Nanowires

ZnO is not only a wide band gap ( $E_g = 3.37\text{eV}$ ) semiconductor, but also room temperature and high temperature luminescence materials with high exciton binding energy as 60 meV. Due to these two promising properties, people believe ZnO has tremendous applications in optoelectronics application, and a great amount of effects have been placed on ZnO nanowires for UV sensors, photodiodes, etc.

Photoluminescence (PL) spectrum of vertical aligned ZnO nanowires displays a peak at wavelength of 380 nm (see Figure 5). The intensity of the spectrum increases as the detector rotates closer to the vertical aligned direction along the nanowires.

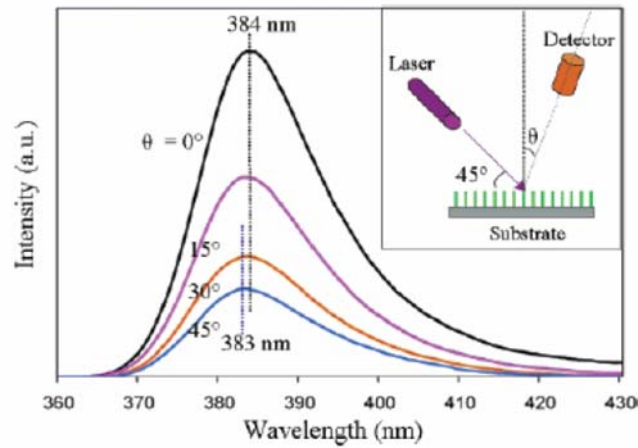


**Figure 5: Photoluminescence (PL) spectra acquired from an aligned ZnO nanowires arrays as a function of the angle between the detector and a direction normal to the substrate. The inset shows the experimental setup.<sup>35</sup>**

ZnO nanowires have been applied as UV sensors because the band gap is larger than the energy of visible light photons. Because of the high surface to volume ratio, trapping at surface states drastically affects the transport and photoconduction properties of the nanowires.<sup>36</sup> Figure 6 shows a schematic diagram explaining photoconduction mechanism in ZnO nanowires. It has been previously known that oxygen molecules are absorbed on the nanowires surface and capture the free electrons presented in n-type ZnO nanowires.  $O_2(g) + e^- \rightarrow O_2^-(ad)$ . When the UV light illuminates the ZnO nanowires, it generates many electron-hole pairs.  $h\nu \rightarrow e^- + h^+$ . The holes migrate to the surface, and then recombine with negatively charged adsorbed oxygen ions, and photodesorb oxygen molecules, leaving behind unpaired electrons, which increase the conductivity of the nanowires.  $O_2^-(ad) \rightarrow O_2(g) + e^-$ .

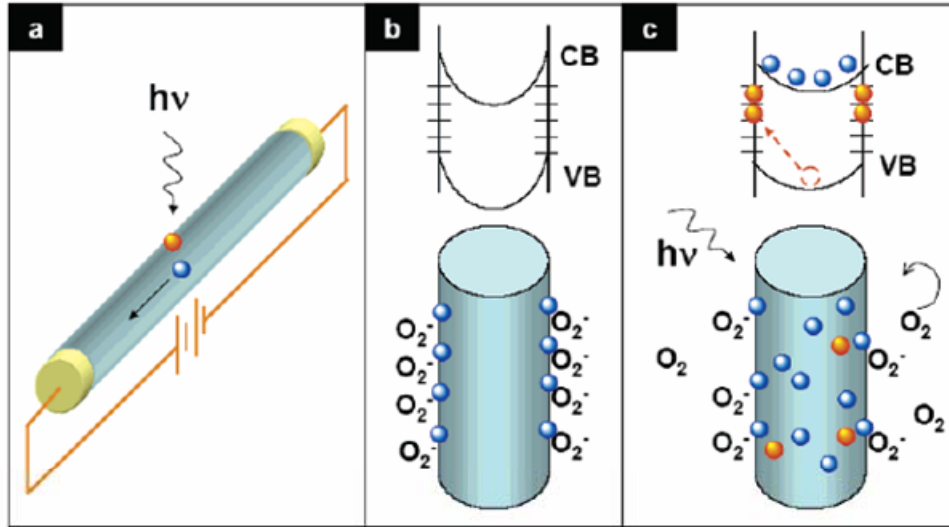


**Figure 6: (a) Photoconduction in a ZnO nanowires photodetectors. (a) Schematic of the photodetector. Upon illumination with photon energy above  $E_g$ , electron-hole pairs are generated and holes are readily trapped at the surface. Under an applied electric field, the unpaired electrons are collected at the anode, which leads to the increase in conductivity. (b and c) Trapping and photoconduction mechanism in ZnO nanowires: the top drawing in (b) shows the schematic of the band diagrams of a nanowires in dark, indicating band-bending and surface trap states. VB and CB are the valence band and conduction band, respectively. The bottom drawing shows oxygen molecules adsorbed at the nanowires surface that capture the free electron present in the n-type semiconductor forming a low-conductivity depletion layer near the surface. (c) Under UV illumination, photogenerated holes migrate to the surface and are trapped, leaving behind unpaired electrons in the nanowires that contribute to the photocurrent. In ZnO nanowires, the lifetime of the unpaired electrons is further increased by oxygen molecules desorption from the surface when holes neutralize the oxygen ions.<sup>36</sup>**

The UV sensing properties have been reported by several groups. In Soci's paper<sup>36</sup>, the current increases significantly under illumination, and a calculated photoconductive gain of  $G \sim 10^8$  is achieved. To better illustrate the dramatic change, a natural logarithmic scale of the photocurrents has been drawn in Figure 7. But Heo's and others' papers<sup>37, 38</sup>, a relatively low sensitivity (less than 10) and long decay time (more than 10s) have been reported. The inconsistency means the existence of some unknown factors.

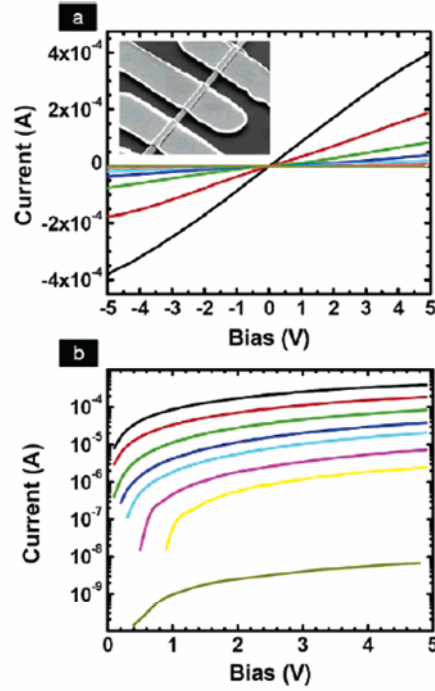
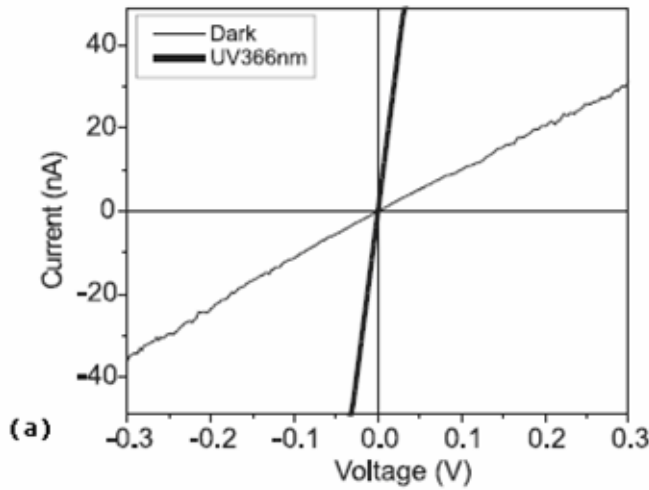


Figure 7: (a) I-V characteristics of a single nanowires photodetector as a function of light intensity; from top to bottom, the curves were measured at the following intensity:  $4 \times 10^{-2} \text{ W/cm}^2$  (black),  $4 \times 10^{-3} \text{ W/cm}^2$  (red),  $4 \times 10^{-4} \text{ W/cm}^2$  (green),  $1.3 \times 10^{-4} \text{ W/cm}^2$  (blue),  $4 \times 10^{-5} \text{ W/cm}^2$  (cyan),  $1.3 \times 10^{-5} \text{ W/cm}^2$  (magenta),  $6.3 \times 10^{-6} \text{ W/cm}^2$  (yellow), and in dark (brown). Inset is the SEM image of a typical ZnO nanowires device (obtained at  $45^\circ$  tilted angle); the spacing between the interdigitated electrodes is 2  $\mu\text{m}$ . (b) The I-V curves presented in (a) are replotted on a natural logarithmic scale.<sup>36</sup>



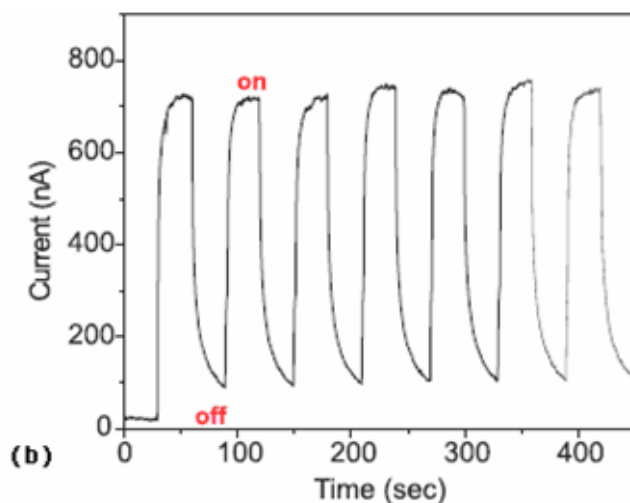


Figure 8: (a) I-V characteristics from single ZnO nanowire in dark and under illumination from a 366nm Hg lamp. (b) Time dependence of photocurrent as the 366nm light source is modulated.<sup>37</sup>

### 1.2.6 Field Effect Sensing Properties of ZnO Nanowires

M. S. Arnold, et al., firstly reported ZnO nanowire based field effect transistor (FET) in 2003 (see Figure 9).<sup>39</sup> They observed switching ratio as large as 6 orders of magnitude and conductivity as high as  $15 (\Omega \text{ cm})^{-1}$ , as illustrated in Figure 10.

The electrical conductivity of ZnO nanowires strongly depends on the species and concentration of surface adsorbed molecules. Therefore, ZnO nanowires are ideal for the fabrication of electrical signal based sensors for chemical and biological detection, which are better than the bio-detection because of in-situ and real-time nature. Up to now, ZnO nanowires have been demonstrated as a good candidate in detecting oxygen, hydrogen, ethanol, biological objects, etc.<sup>40, 41</sup>

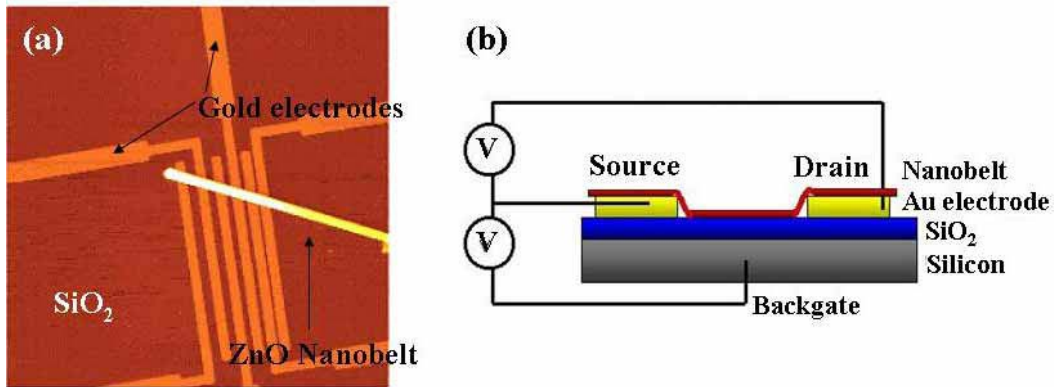


Figure 9: (a) AFM image of a ZnO nanobelt based FET. (b) Schematic of the FET.<sup>39</sup>

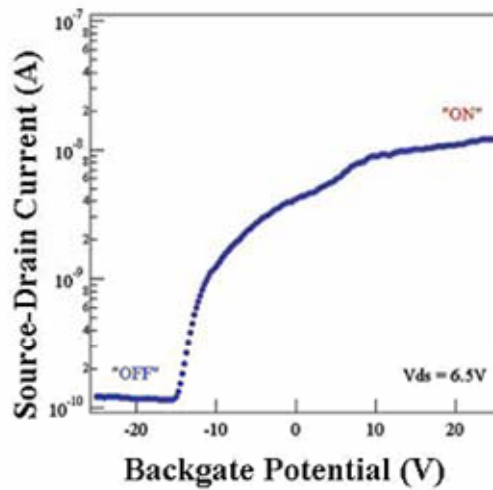


Figure 10: Source-drain current versus gate bias for a ZnO FET in ambient.<sup>39</sup>

### 1.2.7 Electromechanically-Coupled Nanodevice Theory

Electromechanism combines the science of electric engineering and mechanics. It includes piezoelectric effect, converse piezoelectric effect and coupling effect of piezoelectric and semiconducting properties. Piezoelectricity is the ability of crystals to generate a voltage in response to an applied mechanical stress. The materials exhibit piezoelectric effect will also exhibit converse piezoelectric effect, in which the materials

can change shape by a small amount when subjected to an externally applied voltage. The piezoelectric and converse piezoelectric effects find useful applications such as the production and detection of sound, generation of high voltages, electronic frequency generation, and microbalance. Strictly speaking, the piezoelectric coefficients are a 3rd rank tensor, and ZnO has 3 independent coefficients, reflecting the relation between polarization and strain or stress. The piezoelectric coefficients of ZnO bulk materials have been theoretically calculated and experimentally measured, which are about 1/3 of those of the commercialized piezoelectric PZT material. Currently, the practical difficulty remains in identifying the inhomogeneous properties on a nanoscale object. Only one paper about ZnO nanobelt piezoelectric coefficient  $d_{33}$  measured in AFM has been published and frequency-related piezoelectric phenomenon has been reported.<sup>42</sup> The methodology to measure the other two coefficients of ZnO nanowires is still in progress.

Some interesting and exciting piezoelectric and semiconducting coupled phenomena in ZnO nanowires have been newly discovered and electromechanically-coupled nanodevice theory has been proposed to explain these new phenomena. The first exciting discovery is the demonstration of nanogenerators.<sup>8</sup> When aligned ZnO nanowires are deflected with a conductive AFM tip in contact mode, the coupling of piezoelectric and semiconducting properties in ZnO creates a strain field and charge separation across the nanowire as a result of its bending. The mechanical energy is preserved as electric energy because of the Schottky barrier formed between the metal tip and the ZnO nanowire. The charges are released and output voltage is captured when the tip passes the top of the nanowire and touches the compressed side of the nanowires (see Figure 11 c). This approach has the potential of converting mechanical, vibrational and

hydraulic energy into electricity for powering nanodevices. For a long time, people believed that the applications of nanodevices would be greatly limited by their macroscopic battery or other power systems. The last discovery is believed to be a milestone in nanotechnology, which opened a new field in producing the nanoscale battery to support the nanodevices. In 2007, a new design with zigzag metal electrodes was developed to replace the AFM tip.<sup>14</sup> The new nanogenerator was fabricated with vertically aligned ZnO nanowire arrays that were placed beneath the zigzag electrodes. The piezoelectric-semiconducting coupling process converted the mechanical energy from an ultrasonic wave to direct current. Recently, Z.L.Wang's group has demonstrated the harvest of low frequency vibrational energy and conversion to electricity by a microfibre-nanowire hybrid structure.<sup>43</sup>

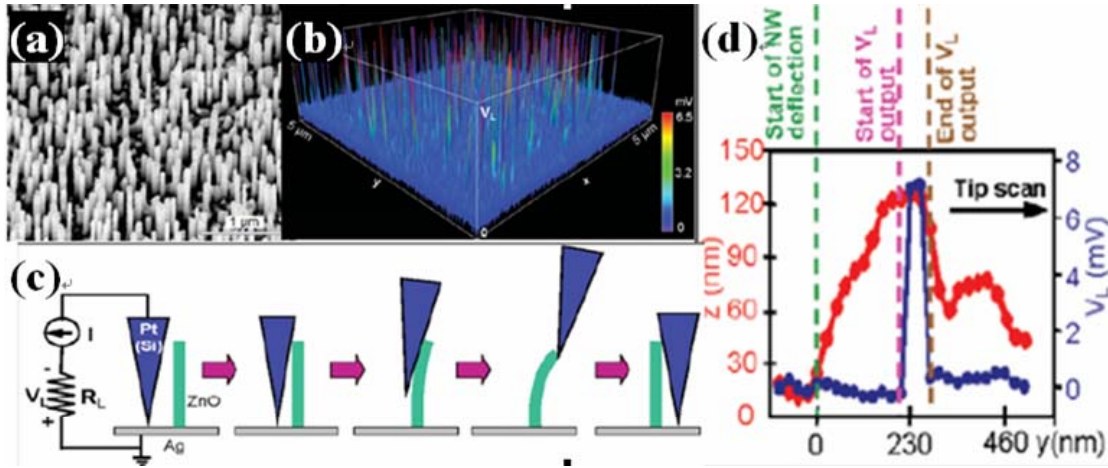


**Figure 11:** (a) Aligned ZnO nanowire array grown on  $\text{Al}_2\text{O}_3$  substrates. (b) AFM output voltage image of nanowire array. (c) Experimental setup and procedures for generating electricity by deforming a ZnO nanowire with a conductive AFM tip. (d) Line profiles from the topography (red) and output voltage (blue) images across a nanowire.<sup>8</sup>

The conductance change in a bending ZnO nanowire<sup>44</sup> can also be explained by the coupling effect of piezoelectric and semiconducting properties. When a ZnO



nanowire is attached between two electrodes inside a SEM chamber and a fixed voltage is applied along it, the current passing through the ZnO nanowire is approximately inversely proportional to its bending curvature (see Figure 12). Experiments have already shown that the electric current of ZnO nanowire will decrease when the nanowire bends, and the current will increase when the nanowire straightens, and the whole process is reversible.<sup>44</sup> The piezoresistance is the ability of crystal to change electric resistance in response to applied mechanical stress, and the previous phenomenon can be called as one kind of piezoresistance. The traditional piezoresistive effect involves several possible mechanisms. The first is the geometrical piezoresistive effect. The piezoresistive effect of metal sensors is only due to the change of the sensor geometry resulting from applied mechanical stress. The piezoresistive effect of semiconductor materials can be several magnitudes larger than the geometrical piezoresistive effect in metals and is present in materials like germanium, polycrystalline silicon, silicon carbide, and single crystal silicon. The resistivity change in semiconductor Si is mainly due to the mobility change in charge carriers. The mechanism in ZnO nanowire piezoresistive effect is suggested to be different from the previous two. When the piezopotential appears across the bent nanowire, some free electrons in the n-type ZnO nanowire may be trapped at the positive side surface and become non-movable charges, thus lowering the effective carrier density in the nanowire. On the other hand, even if the positive potential side could be partially neutralized by the trapped electrons, the negative potential remains unchanged. Hence, the piezo-induced electric field is retained across the width of the nanowire. The free electrons will be repulsed away around the compressed side. Consequently, the width of conducting channel in the ZnO nanowire becomes smaller and smaller while the

depletion region becomes larger and larger with the increase of bending. In summary, at the time of bending, contributions from the carrier trapping effect and depletion zone increased with the bending curvature are suggested to produce a quick drop of the conductance.

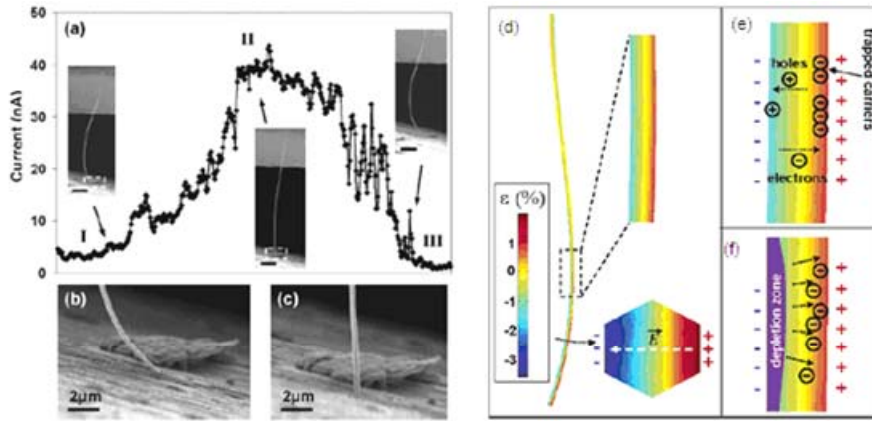


**Figure 12: Current variation with a continuous releasing and bending process of the ZnO nanowire; insets are the three typical bending cases in stage I, II, and III, respectively. (b, c) SEM images of the contacting point between the ZnO nanowire tip and the tungsten needle surface when the nanowire was bent and released. (d) A finite element simulation of the strain distribution along the ZnO nanowire when it is bent. (e) The carrier trapping effect. (f) The creation of a charge depletion zone.<sup>44</sup>**

# CHAPTER 2

## SYNTHESIS OF NANOMATERIALS

### 2.1 High Temperature Vapor Deposition Method

#### 2.1.1 Experimental Setup

Currently, this research has mainly involved high temperature physical vapor deposition method to synthesize ZnO nanomaterials. In the high temperature method, a tube furnace has been set up and optimized to grow well-controlled ZnO nanomaterials. The schematic diagram of the furnace system is showed below (see Figure 13).

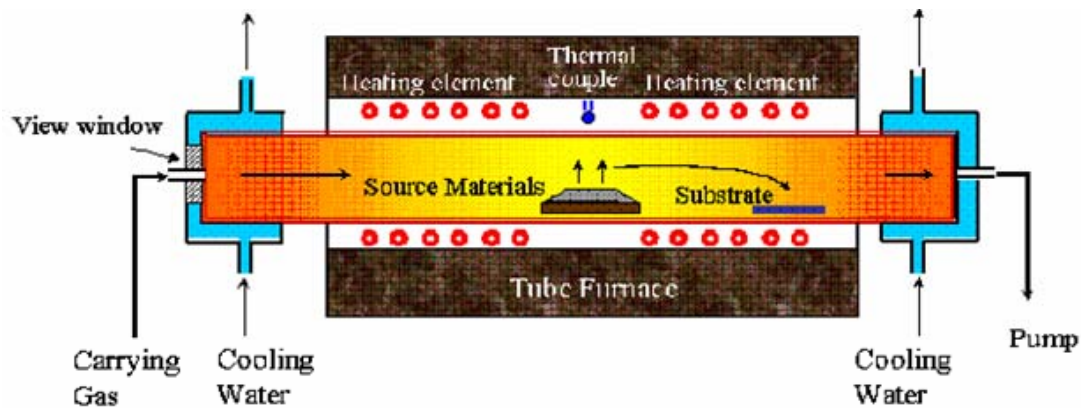


Figure 13: Schematic of the tube furnace.

The core part of the system is the single zone tube furnace whose model number is Thermolyne 793000. Exposed heating element coils embedded into ceramic fiber insulation provided the capability of rapidly increasing the temperature up to 1500 °C in 30 minutes. A digital programmable controller with one stored program of eight

segments controls the heating of the furnace. Each segment of the program consists of three parts: a ramp rate (ranging from 1 °C/min to 60 °C/min), a temperature set point (ranging from 100°C to 1500°C), and a dwell time (ranging from 0.1 min to 999.9 min). An alumina tube with 30” in length, 1.75” in outer diameter and 1.50” in inner diameter is placed inside the tube furnace. Because the furnace chamber is only 24” in length, the alumina tube protruded six inches on either side of the furnace. Both ends of the tube are covered by stainless steel end caps and sealed with O-rings. Cooling water with constant temperature is circulated inside the cover caps to form a reasonable temperature gradient in the tube. One end cap is fitted with a gas inlet connection for introducing the inert carrier gas into the system as carrying gas and a quartz window is also embedded on this end cap to monitor the evaporation process inside the tube or as a transparent window. Another end cap is connected to the pressure system to exhaust the waste gases into a hood.

In the system, the alumina tube acts as the reaction chamber for evaporation and deposition. Generally, source powders loaded in an alumina boat are located in the middle of the furnace, the highest temperature region. The desired nanomaterials are deposited on substrates placed a certain distance away from the source in the downstream direction of the carrier gas.

Several parameters are influencing the morphology of the final products. The temperature control is one of the most important parameters for synthesis. The temperature for the furnace system related with this dissertation is measured by a thermal couple placed at the center of the furnace chamber, but outside and on the top of the alumina tube. As a single zone furnace, the temperature readout is the only feedback

available to control the temperature inside the furnace. Therefore, it is essential to know the temperature gradient along the horizontal direction because the local deposition temperature is coupled for the distance from the substrate to tube center where the highest temperature is. As a result, the temperature gradients for several different furnace temperatures are measured. An S-type thermocouple element (Platinum 10% Rhodium) sheathed in an alumina sleeve, is inserted into the furnace under a 300mbar vacuum. A series of data points are taken at various positions within the alumina tube which is centered in the furnace, so that the temperature gradient across the entire furnace could be extrapolated. Although all of the data for the measured temperature gradients are taken using a 300 mbar chamber pressure, previous unpublished studies demonstrated no obvious change in the temperature gradient with varied chamber pressure, which is to be expected. Figure 14 shows the data for six distinct source temperatures and their corresponding temperature gradients. A best-fit curve is calculated for each. These curves were then used to extrapolate the local substrate temperature with the corresponding source temperatures for synthesis.

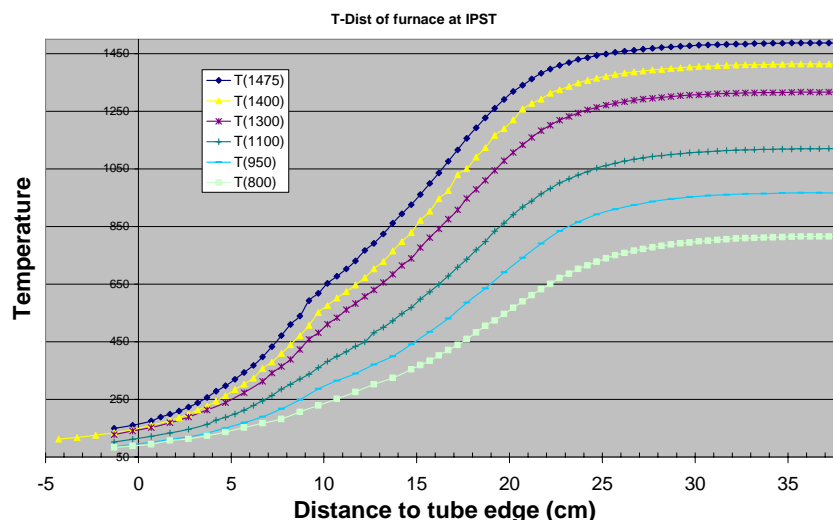


Figure 14: Temperature profile measured inside the alumina tube furnace (from the center to the outside of the furnace) for different source temperatures (1475 °C, 1400 °C, 1300 °C, 1100 °C, 950 °C, and 800 °C).

Another most important parameter in synthesizing nanomaterials is carrier gas pressure. The pressure system is made of three distinct parts. Following the direction of the gas flow, they are carrier gas module, pressure monitor and control, and pump, as shown in Figure 15. The carrier gas module is comprised by gas cylinders and mass flow controllers. The gases used in the system include N<sub>2</sub>, Ar, and O<sub>2</sub>, and each is individually connected to an Aalborg mass flow controller to regulate the gas flow rate through the chamber. The maximum flow rates of N<sub>2</sub>, Ar and O<sub>2</sub> are 200, 100 and 10 standard cubic centimeter per minute (sccm) respectively, and are controlled to within 2% of their maximum flow rate. All of the outlets of the mass flow controllers are joined via 1/4" plastic tubing, and are connected to the gas inlet port of the end cap.

The pressure monitor and control module is connected to the outlet of the furnace system. For the sensitivity reason, the pressure is monitored by two gauges: high vacuum gauge; low vacuum gauge. The high vacuum conditions are measured by a BOC Edwards

analog Pirani vacuum gauge series 500 which has a working range from 100 to  $10^{-3}$  mbar. The low vacuum level is detected by a BOC Edwards analog dial vacuum gauge series CG16K over the pressure range from 10 to 1000 mbar. In addition to monitoring the chamber pressure, two valves are incorporated in order to control the chamber pressure with coarse and fine adjustments. The coarse valve is a BOC Edwards diaphragm isolation valve. The primary purpose of this valve is to fully open the system to the mechanical pump and purge the chamber. A fine adjustable Cole-Palmer multi-turn needle valve is then used during synthesis to make small pressure adjustments and to achieve and maintain a stable reaction chamber pressure. The additional advantage of using double valves is that the needle valve makes vacuum gradually without sucking the power source to the pump system.

A BOC Edwards RV8 Hydrocarbon rotary vacuum pump is used to maintain the vacuum of the system. The mechanical pump has a pumping rate of 8.0 m<sup>3</sup>/h and an ultimate vacuum of  $2 \times 10^{-3}$  mbar. Despite the fact that excess oxygen content can have an adverse effect on deposition, this system is found to be sufficient. The mechanical pump is connected to the vacuum controlling module by a 3-ft, 2-inch-wide flexible stainless steel tube and the outlet is directly connected to the hood exhausting system.

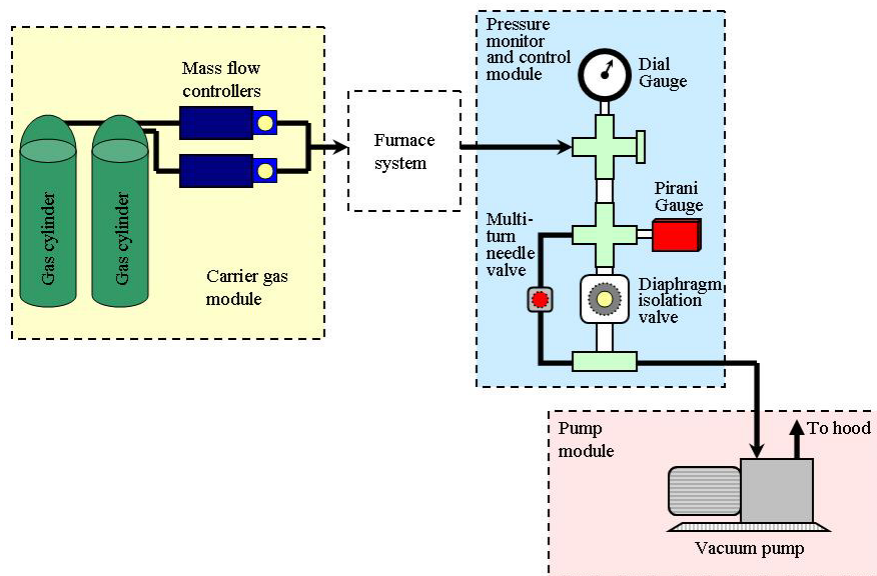


**Figure 15: Schematic of gas and pressure control system.**

### 2.1.2 Underlying Mechanism

The growth mechanism of ZnO nanowires in high temperature furnace is still not fully understood. There are three possible growth mechanisms in the formation of ZnO nanowires, vapor-solid process, vapor-liquid-solid process and vapor-solid-solid process.

Vapor-solid (VS) process involves no catalyst and it has been explored by many researchers to synthesize 1-D nanomaterials because of a self-catalyst effect.<sup>45</sup> The process to grow ZnO nanowires usually occurs at a higher temperature such as 1000-1400° C at the deposition zone. After the nucleus form on the substrate, the newly arrived cations and anions have a very high mobility and accumulate at the growth front or the edges of nanowires, resulting a growth in length as well as cross section, as illustrated in Figure 16.<sup>46</sup>



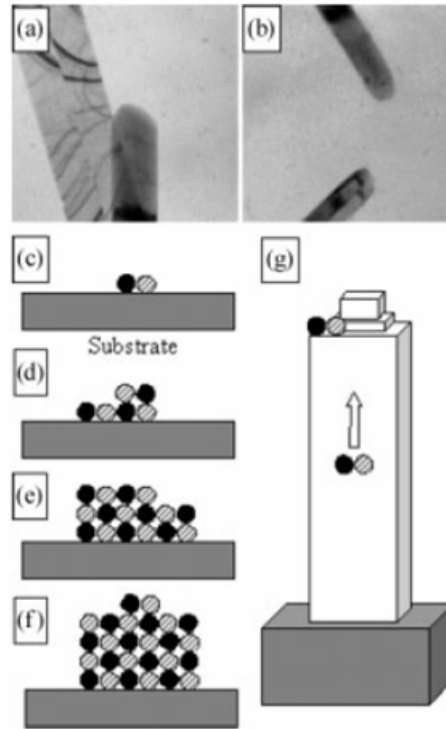


**Figure 16: (a, b) The growth frond/end of ZnO nanobelts, showing no visible catalytic particles at the ends. (c-g) A possible vapor-solid growth process for the formation of nanobelt.<sup>46</sup>**

Usually, catalyst, such as Au, can be used to lower the growth temperature and to control the morphology of ZnO nanowires. Catalyst layer is coated on the substrates by thermal evaporation or sputtering. At some high temperature 900-1400 ° C, the deliberately selected catalyst melts into liquid spheres, which absorb the ZnO vapor and form a liquid alloy. The liquid spheres become supersaturate with more ZnO vapor absorbed and ZnO can separates out underneath the liquid sphere. Thus the whole process is called vapor-liquid-solid (VLS) process. The VLS process was originally proposed by Wagner, et al, to produce silicon whiskers in 1964, and later adopted to 1-D nanostructure growth by other research groups.<sup>47-50</sup> The catalyst acts as the preferential sites for the growth of nanowires. The thickness of the catalyst layer somehow determines the size and density of the liquid sphere, in turn determines the diameter and

density of the nanowires.<sup>51</sup> With further control of the catalyst as a pattern by electron beam lithography, the accurate control of dimension, location, and density is possible, and this is an essential step for the actual application.

However, new experiment results showed strong evidence that the growth process of ZnO nanowire arrays in high temperature furnace is a vapor-solid-solid (VSS) process. Recently, M.Mirkham discovered that Au catalyst remains its original lattice and has not found as an alloy with Zn by XRD technique in their experimental conditions.<sup>52</sup> Besides, the growth of ZnO nanowire with Au as catalyst happen at 800~950°C, much lower than the melting point (~1031 °C) of 33 nm pure Au nanoparticles.<sup>53</sup> It is believed that the growth of ZnO nanowires with Au catalyst could be a VSS process and it only involves the surface diffusion rather than the bulk diffusion. Actually, VSS process has been reported in Al-catalyzed Si nanowires<sup>54</sup>, Au-catalyzed InAs<sup>55</sup> and GaAs<sup>56</sup> nanowires.

### **2.1.3 Vertically-Aligned Nanowire Arrays on SiC and GaN substrates**

The vertically aligned ZnO nanowire arrays on different substrates are of practical importance for various applications. For one, these arrays can work as the basis for fabricating vertical FETs. Vertical FET is a key concept in 3 dimensional electrical circuits, which can highly enhance the density of transducers per unit area and minimize the overall size of the electrical board. Further, this kind of morphology has been discovered the capability of converting the environmental mechanical energy into electrical energy.<sup>8</sup> The previous studies have been focused on the growth of ZnO nanowires on substrates such as Al<sub>2</sub>O<sub>3</sub> and GaN<sup>8, 50, 57, 58</sup>, by systematically changing the growth conditions such as vapor pressure, oxygen partial pressure, and the thickness of

catalyst layer. In this section, we report our study on the growth of ZnO nanowires on some of the technologically important substrates such as SiC and GaN for light emitting diodes, laser devices and light detectors.<sup>59, 60</sup> The dependence of length, aspect ratio and percentage of the vertically aligned NWs on synthesis conditions have been studied. This study is important because it gives the conditions under which the well-aligned NWs can be grown for application in optical sensors, nanogenerators and field emissions.

All syntheses were performed in our high temperature tube furnace. Equal amount (by weight) of ZnO and graphite powder (0.6g each) were loaded in an alumina boat located at the center of an alumina tube, which was later placed in a single-zone tube furnace. Argon was used as carrier gas at a flow rate of 49sccm with additional 1sccm oxygen to facilitate the reaction. Substrates were coated with a thin layer (7-8nm) of Au as catalyst and placed 7~12cm downstream from the center of the tube. The source materials were heated to 970°C at a rate of 50 °C/min, and the temperature was held at the peak temperature for 30-90 min, which mainly influence the length of the nanowires, under a pressure of 160 Torr, while the local temperature of the substrates was between 930-970°C. All previous parameters were chosen after careful optimization.

The morphology of the as-grown products was examined using scanning electron microscopy (SEM, LEO 1530 and LEO 1550). Vertically aligned nanowire arrays were found covering the whole SiC (0001) and GaN (0001) substrates (size is ~ 0.3 x 0.3 cm<sup>2</sup>), as illustrated in Figure 17 a, b. The energy dispersive spectroscopy (EDS) experiment confirmed the nanowires to be ZnO (see inset in Figure 17 d). However, for CdTe and Si substrates, even after a series of designed experiments, only a few of random ZnO nanowires were detected on these substrates, and the rest area either was bare or covered

with ZnO particles. Thus, we just concentrate on discussing the experiments about ZnO nanowire arrays growth on SiC and GaN substrates. The best nanowire growth in term of high percentage of vertically aligned nanowires and uniform length was located around 960°C for both SiC and GaN substrates, and detailed statistical analysis will be discussed later. The product was also characterized using transmission electron microscopy. The growth orientation of ZnO nanowires was along (0001), and a tiny Au catalyst sphere was found at the growth front (see Figure 17 c). Although EDS can barely show the elemental composition of SiC and GaN substrate due to the short sampling depth, strong peaks of substrates can be detected in x-ray diffraction (XRD) curves (see Figure 17 d), indicating the high orientation of ZnO nanowires and substrates. The experiments showed that perfect vertically aligned ZnO nanowire arrays (wurtzite,  $a=0.3249\text{nm}$ ,  $c=0.5207\text{nm}$ ) only occur on SiC (0001) (wurtzite,  $a=0.3076\text{nm}$ ,  $c=0.5048\text{nm}$ ) and GaN (0001) (wurtzite,  $a=0.3189\text{nm}$ ,  $c=0.5185\text{nm}$ ) substrates. ZnO (0001) plane has small lattice mismatch (<6%) with SiC (0001) and GaN (0001) planes, and has significant mismatch with other substrates that we have tried. The small lattice mismatch between the nanowires and substrates is believed to play a key role in heteroepitaxial growth of vertically aligned arrays. For nanowires, which have a significant surface to volume ratio, the surface energy dominates nanowires' growth process, especially at their nucleation and initial growth stage. The bigger lattice mismatch results in higher strain energy. Higher strain energy state becomes unstable and other lower strain energy states associated with other ZnO planes can occur, effectively reducing the total energy of the system. However, at our synthesis condition, ZnO nanowires prefer [0001] direction as the fastest growth direction. Thus, if the (0001) plane of ZnO is not the boundary with the

lowest energy, ZnO nanowires would have higher possibility to lose the coherence with the substrates, and the fastest (0001) growth direction could point to any random direction. Therefore, vertical aligned ZnO nanowire array is much easier to achieve when there is a small lattice mismatch between ZnO nanowires and substrates.

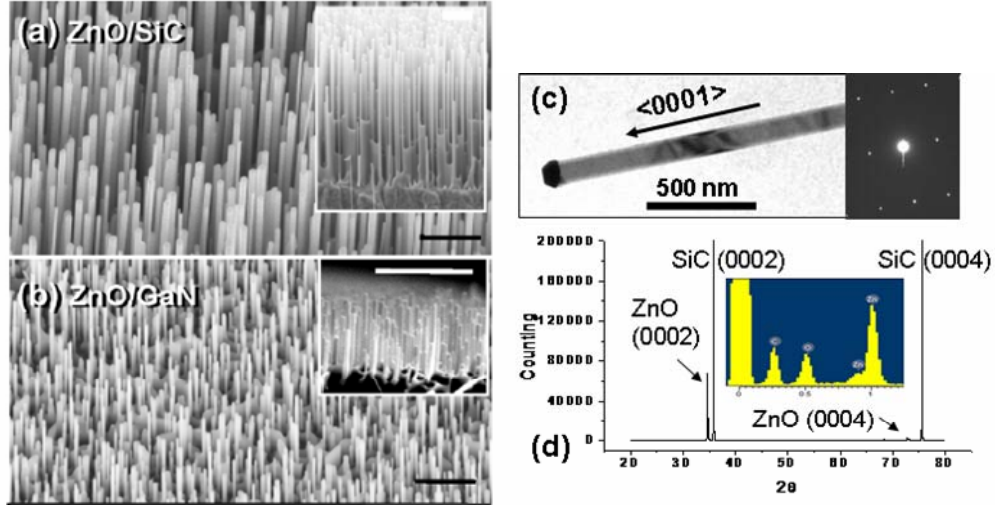


**Figure 17: (a) 30° tilted and cross-sectional SEM images of vertically aligned ZnO nanowires arrays grown on SiC (0001) substrate with 1μm scale bar; (b) 30° tilted and cross-sectional SEM images of vertical aligned ZnO nanowire arrays grown on GaN (0001) substrate with 1μm scale bar; (c) TEM image of a ZnO nanowire grown along (0001) direction with Au catalyst sphere, and the inset shows the corresponding TEM diffraction pattern; (d) x-ray diffraction pattern of the same sample in (a), and the inset is EDS analysis.**

Typical samples A-F were obtained on SiC substrates at 970, 965, 960, 953, 946 and 937 °C temperature region (see Figure 18 a), respectively, after 30 min synthesis, and their spatial distance between closest two samples was 1cm. The following discusses the synthesis results by using statistical method. Five random locations ( $10 \times 2 \mu\text{m}^2$ ) were chosen for each sample; percentage of vertical aligned nanowires, length, diameters, aspect ratio of nanowires were measured and calculated for all nanowires on the chosen locations. Nanowires were regarded as vertical if their axial direction is within 5° deviation of vertical line of the substrate. The length of nanowire was measured from the

growth end to the nanowall that underlies of the nanowires, since it is practically impossible to precisely determine the original substrate surface, if the surface is away from the edges and has interconnecting nanowalls on it. The aspect ratio of length to diameter was also calculated. In order to accurately obtain these parameters, sometimes the samples were tilted to  $30^\circ$  or close to  $90^\circ$ . The statistical results showed that sample B has almost 100% vertically aligned nanowires, while this percentage drops sharply below 50% at  $5^\circ\text{C}$  or even lower temperature zone (see Figure 18 b). The length of nanowires of sample B is  $447\pm 10\text{nm}$ , and corresponding aspect ratio of length to diameter is  $8.0\pm 2.8$  (see Figure 18 c,d), in which errors indicate statistical standard deviation. This means that nanowires in sample B location are probably the best for device application since they have relatively highest uniformity, which is required for reliable nanodevices. The linear fitting (see Figure 18 f) indicates that the nanowires grew at a rate of  $54\text{nm/min}$ . Theoretically, nanowire arrays with any length can be achievable as long as the catalyst particle is still active and the synthesis time increases according to previous discovery. However, in practice, a poisoning of the catalyst particles limits the length of vertical nanowires.

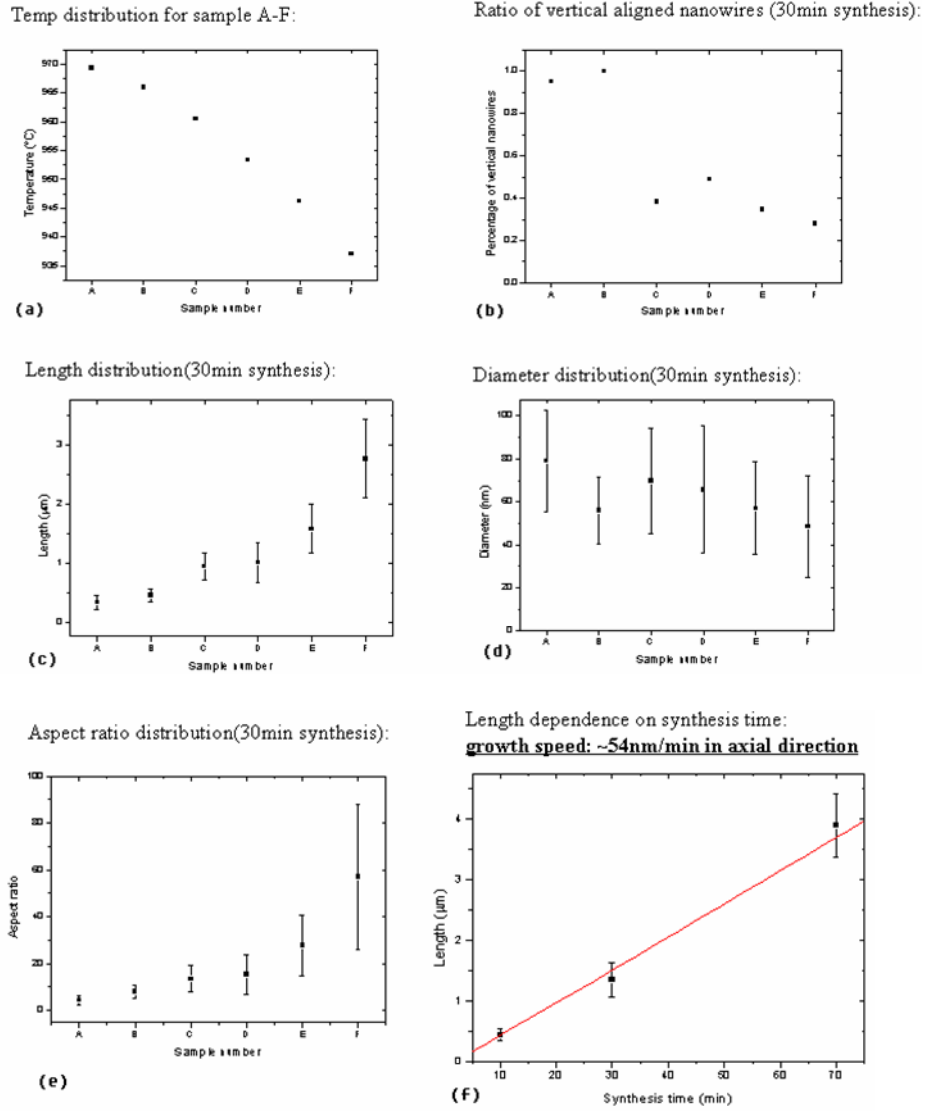


**Figure 18: (a) Temperature distribution, (b) percentage of vertical aligned nanowires, (c) length distribution, (d) diameter distribution, (e) aspect ratio distribution of sample A-F, and (f) growth speed derived from length vs. time relationship.**

Generally, the vertically aligned nanowires are not separated from one another and they are connected by nanowalls (see Figure 19 a). Through SEM and TEM, we found that the residue Au catalyst at the bottom of aligned nanowires induced the sides (01-10) of ZnO nanowires to grow into triangular nanosheets (see Figure 19 b and c). These triangular nanosheets could meet another nanosheets or nanowires and became

interconnected nanowalls. This proposed growth mechanism has been visually explained in a schematic diagram shown in Figure 19 d. These conductive nanowalls are indispensable for some device applications, especially when nanowire arrays are grown on the nonconductive substrates. The electric signals can only be transported to each aligned nanowire through the interconnected nanowalls instead of the underlying substrates.

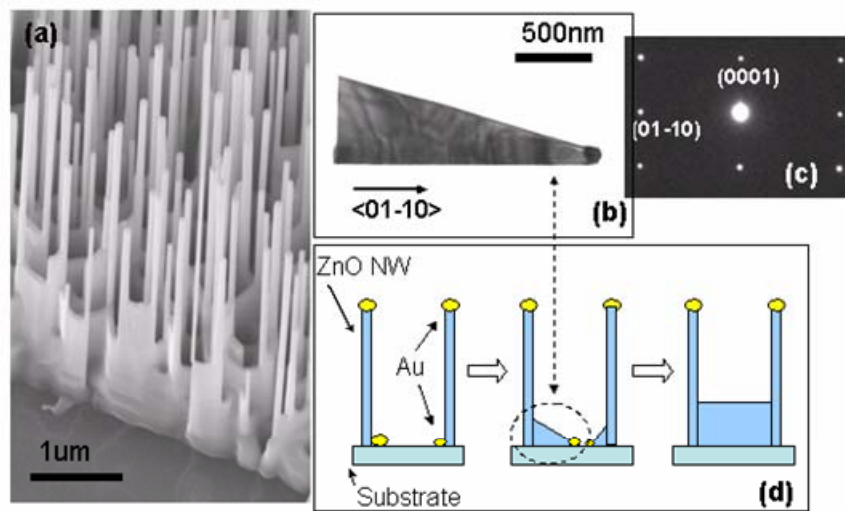


**Figure 19:** (a) The SEM image shows nanowalls connecting individual vertically aligned nanowire; (b) the TEM image and diffraction pattern of a triangular nanosheet, which is the early stage of nanowalls; (c) schematic diagram demonstrating the growth mechanism of nanowalls.

#### 2.1.4 Randomly-Oriented Nanowires

Randomly oriented nanowires are relatively easier to obtain than vertical nanowires because randomly oriented nanowires can grow on various substrates and in a large range of temperature and pressure. As we discuss in the previous session, the vertical aligned nanowires have a narrow range of temperature and pressure. When the temperature or pressure changes, the kinetics of ZnO nanowires deposition change a lot, and this variation means two scenarios might happen: one is that the fastest growth



orientation might switch from [0001] to other directions; the other is that the lowest strain energy interface might no longer be (0001) . Therefore, the growth of nanowires will lose their coherence with the substrates, inducing the random growth of ZnO nanowires. In addition, when the synthesis time increases and in turn leads to the extension of the length of nanowires, the gravity might drag the nanowires off the vertical direction and cause them to forfeit the uniformity. Figure 20 shows randomly oriented nanowires obtained on Si, polycrystalline Al<sub>2</sub>O<sub>3</sub>, SiC and GaN substrates. Generally, among all the randomly oriented nanowires can find two major kinds of nanowires. One kind of nanowires has [0001] growth direction with a hexagonal cross section; the other kind of nanowires, strictly nanobelts, has (0001) polar surfaces as the dominant surfaces.

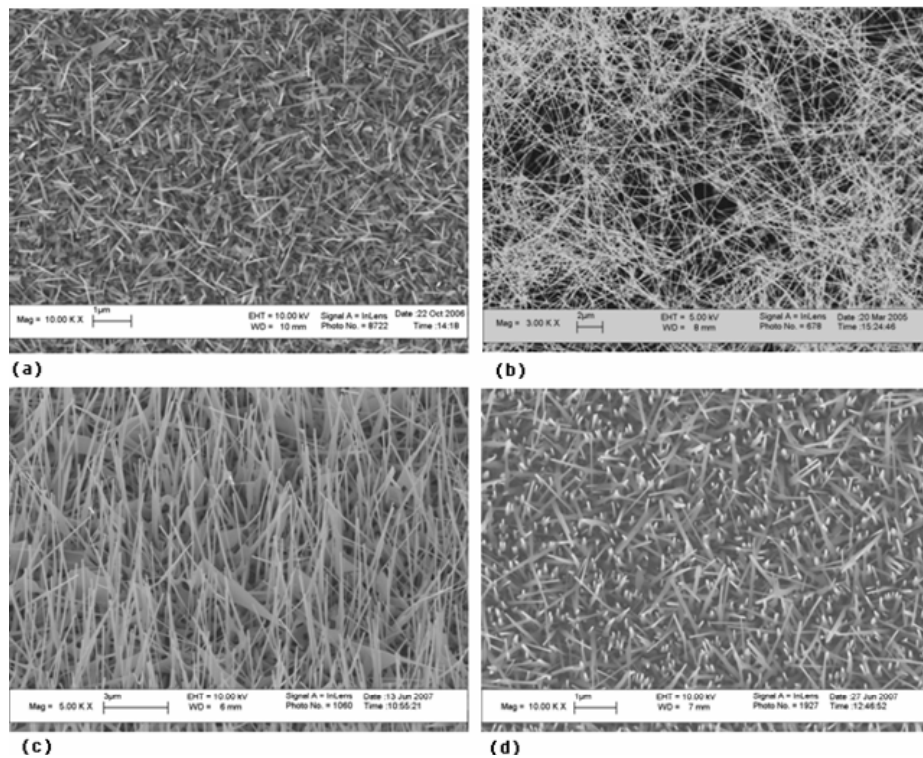


**Figure 20: Randomly oriented ZnO nanowires grown on (a) Si, (b) polycrystalline Al<sub>2</sub>O<sub>3</sub>, (c) SiC and (d) GaN substrates.**

### 2.1.5 Superlattice-Structured Nanohelices

The ZnO superlattice-structured nanohelices were firstly discovered in 2006.<sup>21</sup> The ZnO nanohelices were grown at a high reproducibility by this PVD method too. Two grams of commercial (Alfa Aesar) ZnO powder was compacted and loaded in an alumina boat and positioned at the center of the alumina tube as the source material. The system was pre-pumped to  $\sim 2 \times 10^{-2}$  mbar first. The ramp rate was controlled at 20-25 °C/min when the temperature was raised from room temperature to 800 °C and at 20 °C/min from 800 to 1400 °C. A 20-min holding was introduced at 800 °C. After the temperature reached to 950 °C, argon carrier gas was introduced to raise the pressure from  $\sim 2 \times 10^{-2}$  mbar to the desired synthesis pressure of 260-340 mbar within  $\sim 2.5$  minutes. The physical vapor deposition was carried out at 1400 °C for  $\sim 2$  hours under a pressure of 260-340 mbar. The Ar carrier gas was kept at a flow rate of 50 sccm (standard cubic centimeters per minute). The as-grown nanohelices of ZnO were deposited onto a polycrystalline Al<sub>2</sub>O<sub>3</sub> substrate in a local temperature of 700-800 °C. The as-synthesized samples were characterized and manipulated by scanning electron microscopy (SEM) (LEO 1530 FEG at 5 & 10 kV), high-resolution transmission electron microscopy (TEM) (Hitachi HF-2000 at 200 kV and JEOL 4000EX at 400 kV).

The as-synthesized sample is composed of a significant percentage of freestanding nanohelices. SEM images recorded at high-magnification clearly present the perfect shape and superior uniformity of the nanohelices, which can be left-handed (see Figure 21 A, B) and right-handed (see Figure 21 C, D), and their population ratio is close to 1:1. The diameters of the nanohelices are in the range of 300-1000 nm, the widths of

the nanobelts are 100-500 nm, but the pitch distances are rather spread from 500 – 3000 nm, as seen from a few typical images presented in Figure 21.

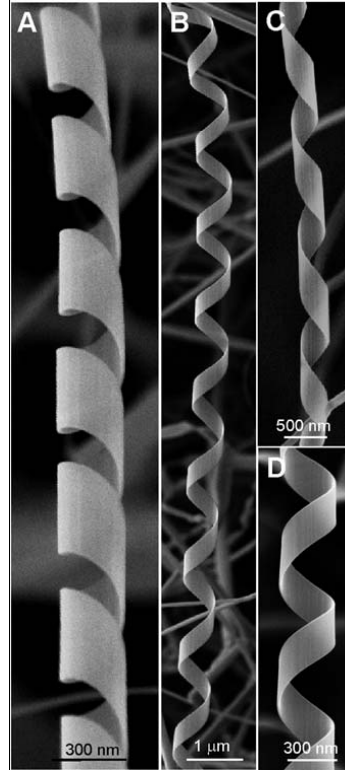


**Figure 21: Typical SEM image of the left- and right-handed ZnO nanohelices.**

TEM analysis shows that a nanohelix is composed of superlattice-structured stripes. The superlattice is made of two types of crystalline nano-stripes oriented epitaxially in the following orientation relationship: Stripe I: growth direction  $[0\bar{1}10]$ , top and bottom surfaces  $\pm(0001)$  (polar-surfaces), and side surfaces  $\pm(\bar{2}110)$ ; Stripe II: growth direction  $[0001]$ , top and bottom surfaces  $\pm(01\bar{1}0)$  (non-polar-surfaces), and side surfaces  $\pm(\bar{2}110)$ . The growth directions of the two types of stripes have a small rotation of  $\alpha \approx 4^\circ$ . This small misorientation may result in a small twist in the geometrical arrangement of the two adjacent stripes. In crystallography, the wurtzite structured ZnO

crystal is described schematically as a number of alternating planes composed of tetrahedral coordinated  $O^{2-}$  and  $Zn^{2+}$  ions, stacked alternatively along the c-axis. The oppositely charged ions produce positively charged (0001)-Zn and negatively charged  $(000\bar{1})$ -O polar-surfaces (c-planes). The polar charges are preserved on the surface during the growth under conditions of high temperature and inert environment. As reported previously<sup>20, 23</sup>, the existence of the polar-surfaces results in the formation of ZnO nanosprings and nanorings. If the width of the nanoribbon is rather large, the electrostatic energy of the polar-surfaces diverges with the extension of its length. A possible way of reducing the electrostatic energy is to transform the polar-surface into a non-polar-surface, provided the interface mismatch energy is reasonably low. A possible way is to form superlattice-structured stripes almost parallel to the growth direction of the nanobelt, one of which preserves the same orientation of the stiff-nanoribbon with c-plane dominated surfaces (stripe I), and the other has  $(01\bar{1}0)$  (a-plane) non-polar-surfaces (stripe II). The two stripes have a coherent and epitaxial interface possibly with low mismatch energy.

In summary, the formation of the nanohelix is a rigid structural alteration caused by the stripes in the superlattice, and the formation of superlattice is likely to be a charge induced structural transformation.

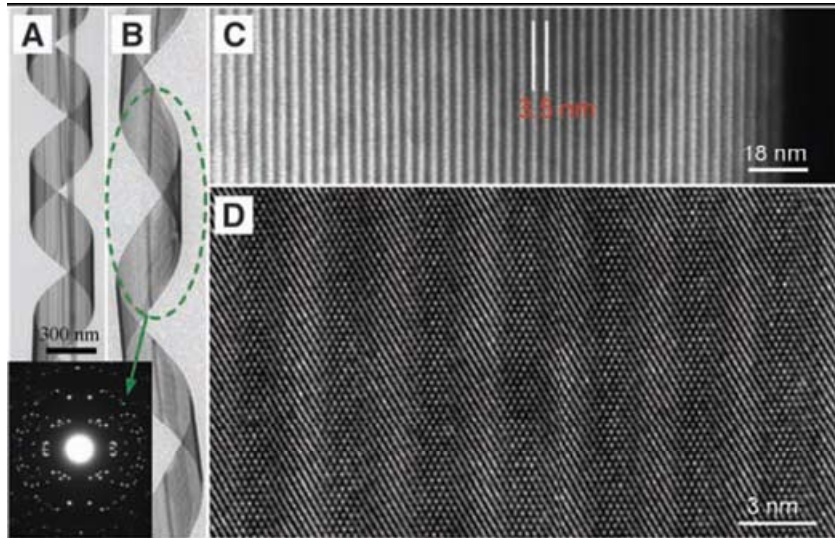


Figure 22: TEM images of ZnO nanohelices

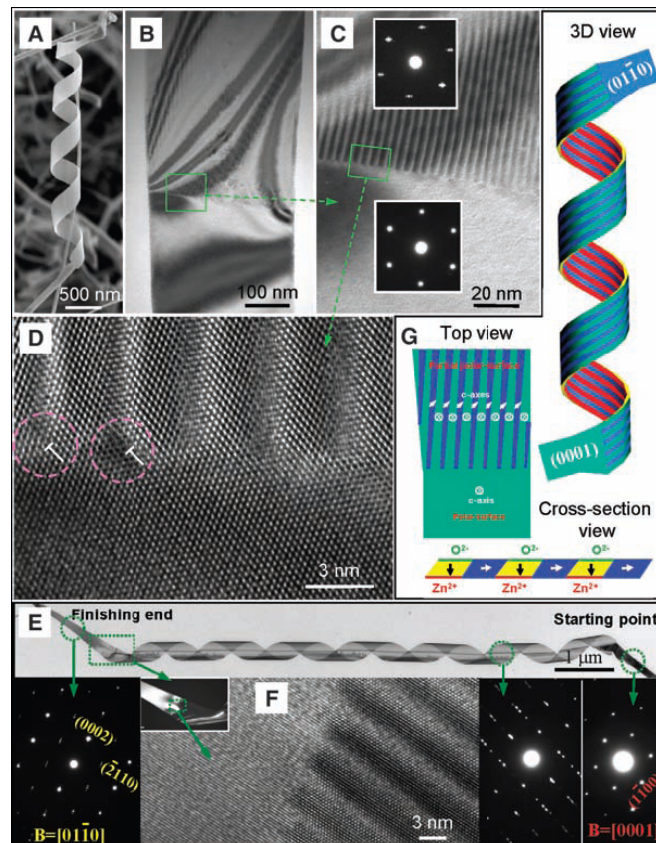
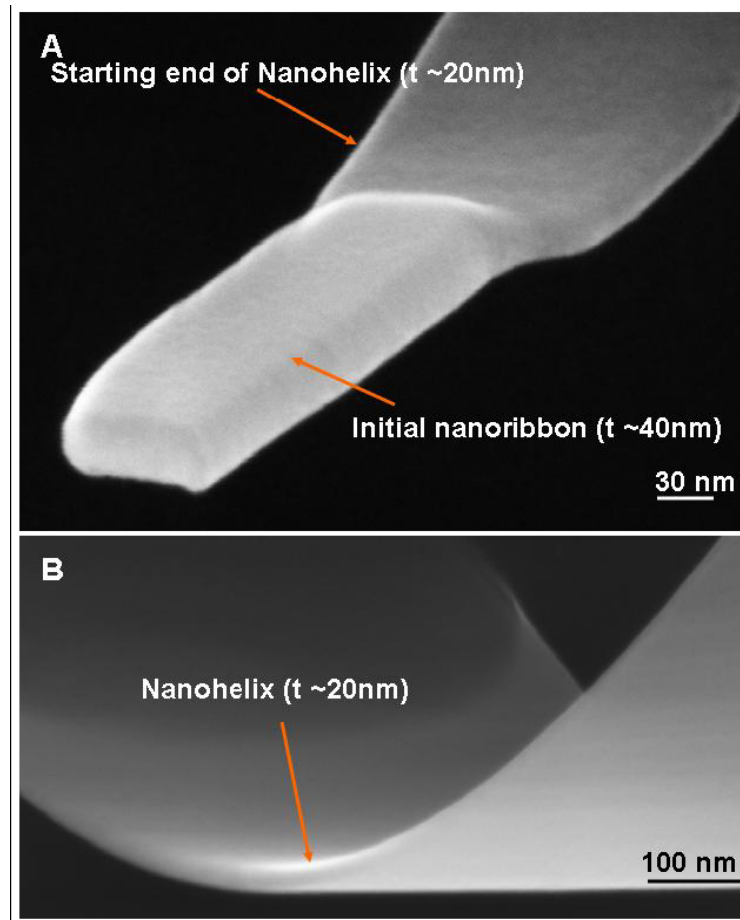


Figure 23: Detailed structural analysis of ZnO nanohelices.



**Figure 24:** Thickness and width change at the joining interface between initial nanoribbon and the nanohelix.

## **2.2. Low Temperature Wet Chemical Method**

### **2.2.1 Procedure of Experiment**

The other method that has been widely used for fabricating ZnO nanostructures is low temperature wet chemical method. Wet chemical methods exhibit tremendous advantages comparing to the high temperature vapor deposition method: low cost, high yield, less experimental parameters, easy scale up capability, polymer comparability, etc.

The ZnO nanowire arrays can be grown on a variety of substrates, such as plastic film, GaN, Si, etc, by wet chemical method at low temperature less than 100° C. The procedure is illustrated in Figure 26. A thin layer (20-100nm) seed layer (Au or ZnO) is coated on the substrate before the hydrothermal growth of ZnO nanowire arrays. The growth of ZnO nanowire is conducted by suspending the seed layer coated substrate faced down on the solution surface. The solution is a mix of equal molar aqueous solution of zinc nitrate ( $\text{Zn}(\text{NO}_3)_2 \cdot 6\text{H}_2\text{O}$ ) and hexamine ( $(\text{CH}_2)_6\text{N}_4$ ). Hexamine is a very unstable materials (see Figure 25), which can easily hydrolyze and produce ammonia.  $\text{Zn}^{2+}$  combines with  $\text{OH}^-$  and produces ZnO, which nucleates and precipitates on the seed layer. The chemical reaction formulas are listed below.

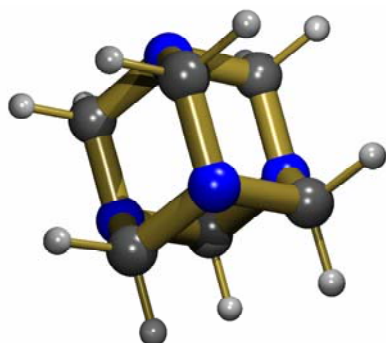
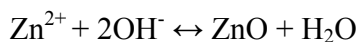
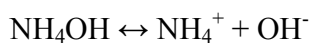


**Figure 25: cage-like structure Haxamine.**

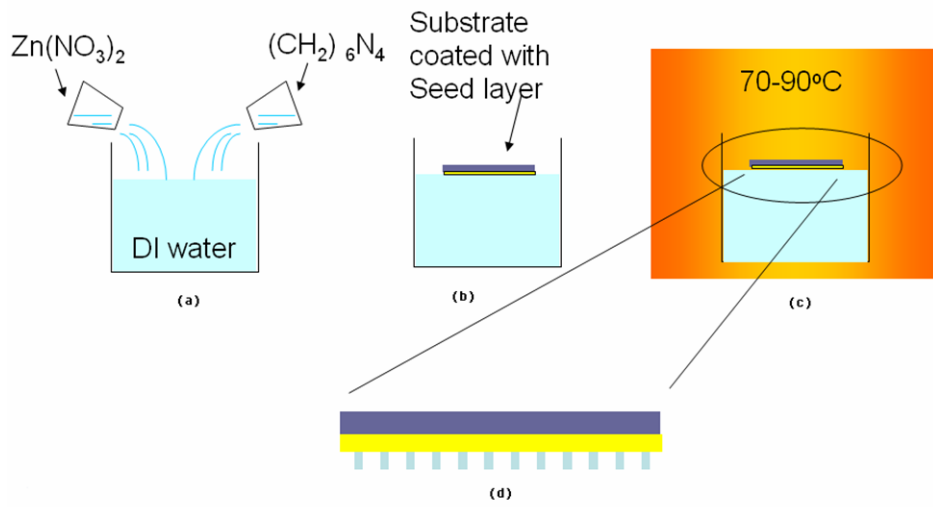


**Figure 26:** (a) Equal amount of Zinc Nitrate and Hexamine are mixed in DI water. (b) Substrate with seed layer is placed face down on mixture solution surface. (c) Beaker is transferred to box furnace and heated up to  $70-90^\circ\text{C}$ . (d) ZnO nanowires nucleate and grow on the seed layer at elevated temperature.

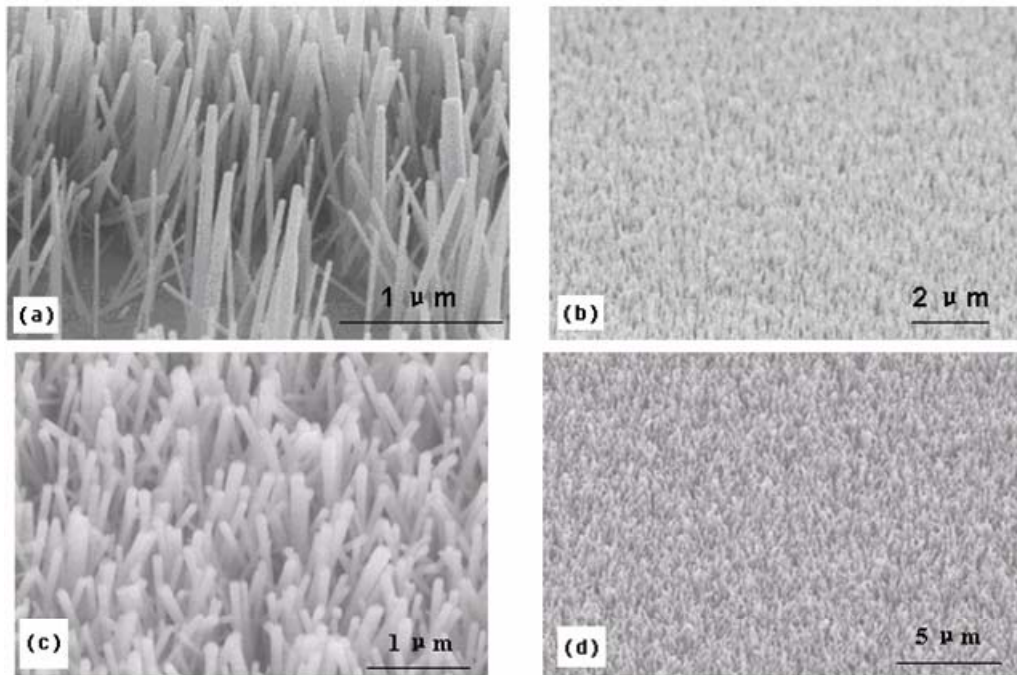


**Figure 27:** (a) low and (b) high magnification of ZnO nanowires on Si substrate. (c) low and (d) high magnification of ZnO nanowires on fluorine doped tin oxide (FTO) glass.

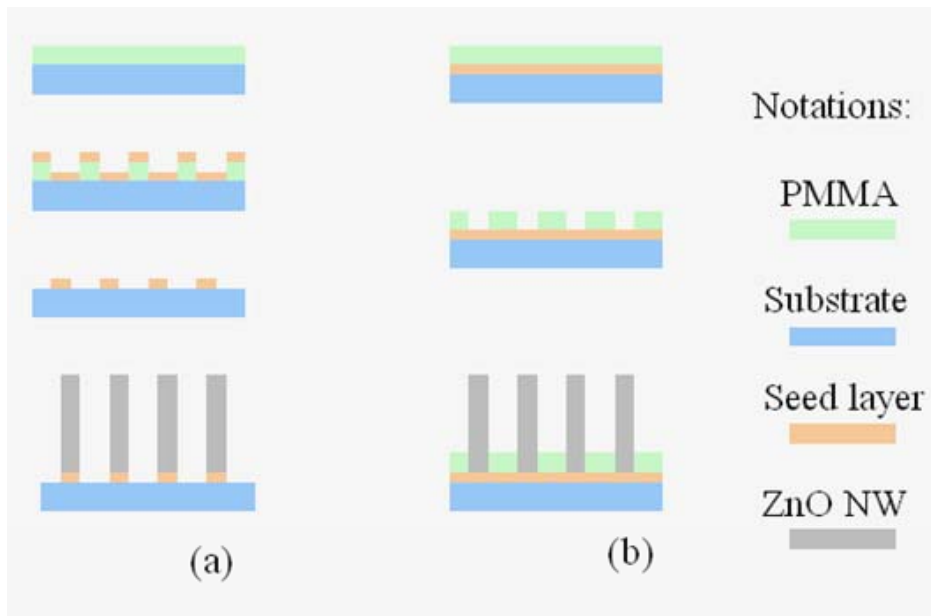


### 2.2.2 Approaches to Controlled Growth

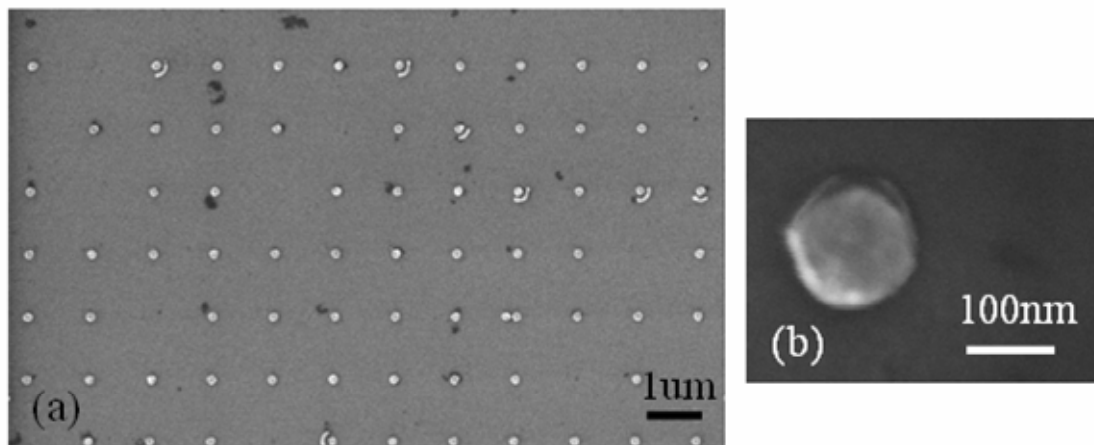
It is very challenging to achieve controllable growth of ZnO nanowires by high temperature vapor deposition method. Wet chemical method occurring at low temperature can preserve the original pattern and becomes a feasible way to control the synthesis. Two schemes, both involving the electron beam lithography (EBL) are proposed to fabricate patterns on the substrate. EBL is able to expose specific area of electron sensitive photoresist, which can be removed after develop process. EBL has been widely used in nanowire electronic device fabrication, and details will be explained in the next chapter. First scheme to control the nanowires is illustrated in Figure 28 a. Holes are fabricated on PMMA by electron beam exposure before Au deposition, thus leaving only patterned individual Au features on substrate after lift off process, and Au features serve as later ZnO nanowire growth location. Second scheme (see Figure 28b) aims to directly remove the specific PMMA and expose circular shape on the Au layer. The substrate is transferred for ZnO nanowire growth without lift off process. PMMA can endure the temperature that the wet chemical method requires, so exposed Au locations provide the nucleation sites.

Figure 29 shows the Au patterns fabricated by scheme 1. The originally designed Au features actually has the diameter 200nm. But during the lift off process, the outer edge of the Au circles can be torn off simultaneously because of poor adhesion with substrate, resulting in the smaller size of the final Au feature (~ 150 nm in diameter). Besides the size reduction, imperfect features such as disappearance of some Au circles and additional accompanying arcs are observed when the size approaches the limit of our

machine (~100nm). The synthesis on this kind of patterned substrate has been tried but not successful.



**Figure 28:** Two different patterning schemes. (a) is characterized with patterned individual Au features. (b) is characterized with patterned PMMA hollow features that are exposing the corresponding features on a layer of Au underneath.



**Figure 29:** Patterned individual Au features on Si substrate. Features are 100nm diameter Au circles with 1  $\mu\text{m}$  distance.

Experiment shows that scheme 2 without lift off process can produce better patterned features. Excellent results have been achieved on Si and GaN substrates even without seed layer in Z.L.Wang's group.<sup>61</sup> Figure 30 is the SEM images of patterned growth of ZnO nanowire arrays on GaN. GaN has the same crystal structure and small lattice mismatch with ZnO in c plane, ensuring the alignment of nanowires on GaN substrate. The size of the holes determines the diameters of the nanowires in some extent. As in Figure 30a, the 100 nm sized holes grow ~300nm nanowires in diameters. There should be significant lateral growth after nanowires grow out from the hole and lose confinement. Still, the combination of EBL and epitaxial growth can provide the control capability in location, orientation, density, diameter and length, which is crucial to future nanowire electronic device application.

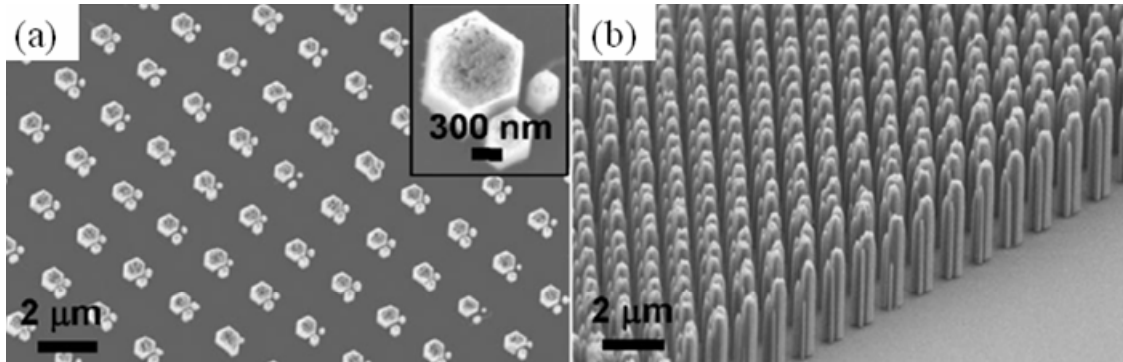


**Figure 30: (a) Vertical view and (b) tilted view of the patterned growth of nanowire arrays on GaN substrate without seed layer.**<sup>61</sup>

# **CHAPTER 3**

## **MANIPULATION METHODS**

In order to perform further investigation on as-synthesized nanowires, researchers usually need to transfer a small amount of nanowires or even a single nanowire from sample substrate to fabricate a single nanodevice. This is a very crucial step in building the devices and setting up the experiments. Several standard methods have been developed to perform this function and will be discussed below.

### **3.1 Electron Beam Lithography**

One of the most common methods is the electron beam lithography (EBL) <sup>62</sup>, which is the practice of scanning a beam of electrons in a pattern fashion across a surface covered with a film of resist, and of selectively removing either exposed or non-exposed region of the resist. This method involves several crucial steps, including electron-sensitive polymer coating, electron exposure, developing, metal coating and lift-off (see Figure 31). With EBL technique, it becomes possible to design a pattern, fabricate two metal pads at both ends of the nanowires, and measure electric and thermal transport properties of a single nanowire. Based on the current equipment, similar experiments can be performed with the LEO 1550 in the department. For more complex requirements, clean room facilities at Georgia Tech Microelectronics Research Center can be used. The problems related with this technique are time-consuming and cost expensive. The application of EBL is strictly limited in the academic research level.

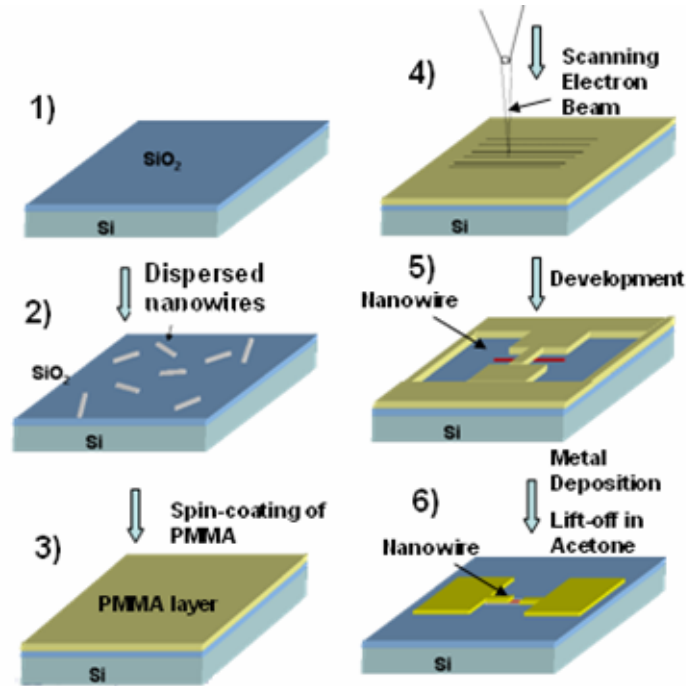


Figure 31: schematic diagram of the EBL procedures.<sup>63</sup>

### 3.2 Dielectrophoresis

Dielectrophoresis is another manipulation method, which has been extensively studied and widely used.<sup>29, 64, 65</sup> Patterned electrodes have to be fabricated at the beginning. The electrodes should be carefully designed to meet two requirements: firstly, a close distance ( $\sim$  a few microns) so that nanowires can be deposited between two electrodes, and secondly, sharp ends so that they could enhance the strength of local electric field and the chance of successful deposition. With the pattern designed, the next step is to fabricate the electrodes in cleanroom by standard lift-off process. Then, when the AC voltage generator at a specific frequency and amplitude is applied between two electrodes, semiconductor nanowires dispersed in solution will be stimulated by the electric field, move and bridge between two electrodes. After the solution evaporates, the

nanowires attach to the electrodes firmly and constitute a device. This method does not require a large amount of work in cleanroom and is easy to perform. The current biggest issue with this method is the unreliable contact, and contact problem will be discussed in detail in later chapters.

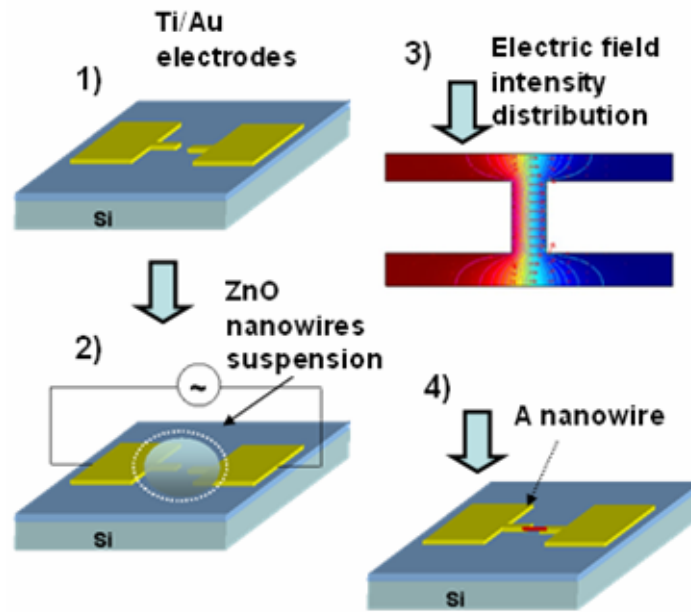


Figure 32: Schematic of the dielectrophoresis process. <sup>63</sup>

### 3.3 Direct Manipulation Technique

Direct manipulation technique has been developed and become a significant method in our group. Currently, two different sets of manipulation systems are available. One is the Kleindiek Micromanipulator installed inside the Nova system in Georgia Tech FIB2Center, the other is the Zyvex S100 manipulation system installed inside LEO 1550 in MSE department. The Kleindiek manipulator has extensive working range ( $100 \text{ cm}^3$ ) as well as sub-nanometer resolution (0.25nm). Since it is incorporated with a focus ion

beam (FIB), the combination of e-beam imaging and ion-beam imaging exhibit unique advantage because they can function as two human eyes and can facilitate the process of identifying spatial location. However, the Kleindiek manipulator operates in a spherical coordinate system, thus the operation is not convenient to perform. The other Zyvex system is more user-friendly since it is built in a Cartesian coordinate system and can move independently in x, y, and z directions. The Zyvex S100 has a coarse mode which provides controlled Cartesian motion over large distances (12 mm of travel with 100 nm resolution) and a fine mode for extremely smooth and precise motion (100 microns of travel with 5 nm resolution).



**Figure 33: Photo of Nova dual beam focus ion beam machine.**



**Figure 34: Photo of the micro-manipulator and the control electronic system from Kleindiek.**



**Figure 35: Controller and 4 probe manipulator system S100 from Zyvex.**

The standard transferring process can be separated into three steps: firstly, cautiously approach the tungsten probe to touch nanostructures, such as 1-D nanowires, 2-D nanocombs, and 3-D nanonetworks; secondly, pick up the nanostructures with the probe by electrostatic forces, e-beam-induced carbon deposition or FIB-induced Pt deposition; thirdly, transfer to other location and place them onto the targeted positions.



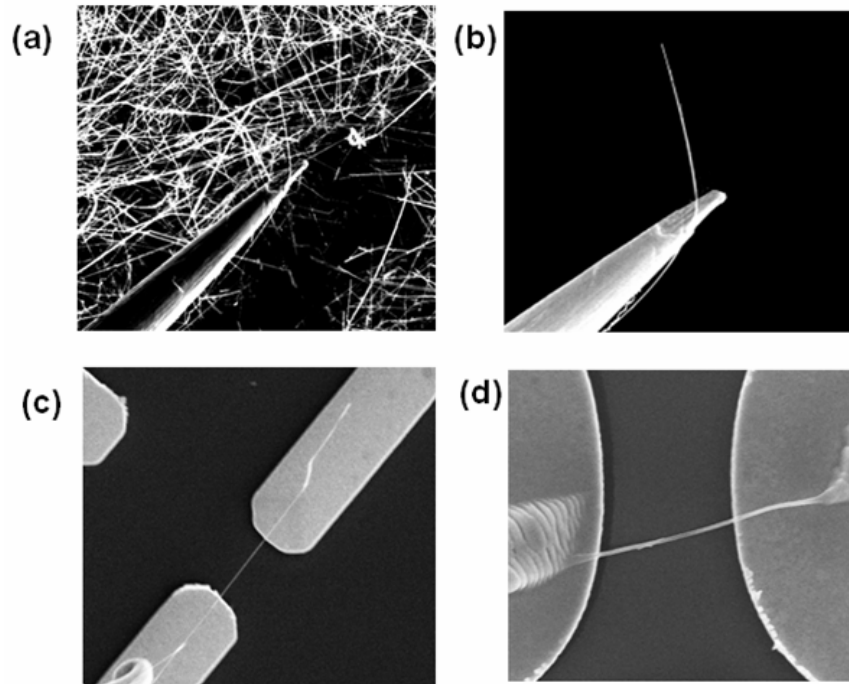


**Figure 36: Schematic of transferring a single nanowire from sample substrate to between two electrodes.**

One unique characterization of FIB system is that it can induce Pt deposition or mill the materials as specific location. The Pt deposition around the probe and the nanostructure can significant enhance the local mechanical adhesion force and reduce the difficulty in transferring nanomaterials. In another application as device fabrication, Pt deposition can work as the buffering layer, make a connection between nanomaterials, eliminate the Schottky barrier or improve the Ohmic contact behavior between them. In addition, the gallium beam could be used to cut unwanted electrical connections.

### **3.3.1 Example 1: Manipulation and Mechanical Measurement on Silicon Nanowires**

Silicon is the most important material for electronic industry. Its unique electronic, optoelectronic, thermal and mechanical properties have made Si an ideal choice for integrated circuits, memory devices, solar cells and microelectromechanical systems (MEMS).<sup>66-69</sup> As for one dimensional nanomaterials, carbon nanotubes, silicon nanowires and ZnO nanowires/nanobelts are the three dominant choices of structures, because of their largely improved, different and/or unique properties at nano-scale.<sup>6, 16, 70, 71</sup> As sizes of MEMS approaching nanoelectromechanical systems (NEMS)<sup>72</sup>, exploration of the change of mechanical properties at nano-scale is vitally important.<sup>22</sup> Silicon nanowires (NWs) are the key building blocks of future electronics. Several approaches have been developed to study mechanical behavior of Si nanowires (NWs).<sup>73-76</sup> These existing literatures have made progress on the phenomenal observations on plasticity and measurement of elastic modulus of single NW or NW arrays. In this paper, using a manipulation probe and an AFM tip in a scanning electron microscope (SEM), we have investigated the mechanical behavior of a single Si NW under buckling and bending conditions. Some of the mechanical properties of Si NW have been quantified. Our study has demonstrated the tough and robust behavior of Si NWs.

The Si NWs used for the experiments were fabricated by chemical vapor deposition via the vapor-liquid-solid (VLS) growth process.<sup>77</sup> Figure 37 shows a transmission electron microscopy (TEM) image of an as-grown Si NW to show its core/shell structure. The diameters of the NWs are 40-90 nm. The thickness of the outside

native oxide layer is about 5 nm. Inset shows a diffraction pattern, revealing the single crystalline structure of the NW.

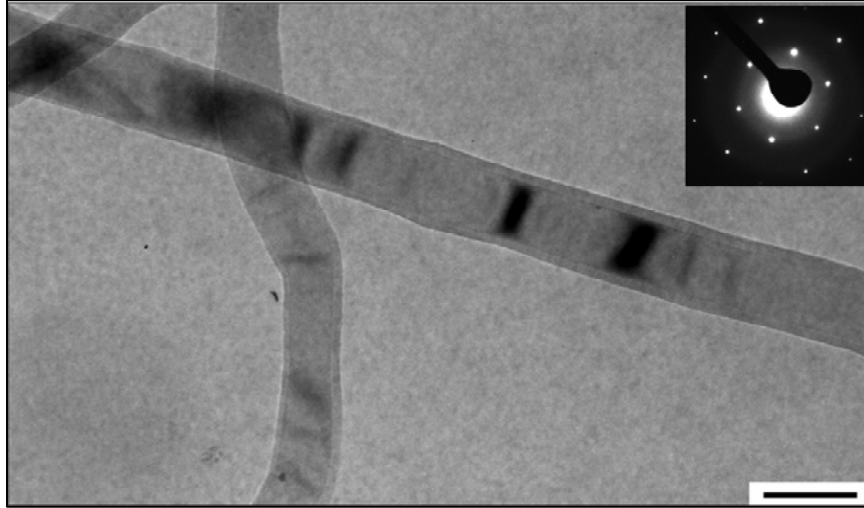


**Figure 37: TEM image of the SiNW with a 5-10 nm native oxide layer (scale bar 100nm). Inset: Selected area electron diffraction pattern.**

The manipulation of a Si NW was made using a tungsten probe, and the AFM cantilever was used to measure the force-displacement response of a single Si NW. Figure 38 (a) and (b) schematically illustrate the principle of the mechanical manipulation setup. At the beginning as shown in Figure 38 (a), the Si NW was attached to the probe. Then the Si NW was bent by pushing the probe against the AFM cantilever. The AFM cantilever would be deflected as shown in Figure 38 (b), from which the displacement and the applied force can be quantified, provided the mechanical behavior of the cantilever is well characterized. The displacement was characterized by the distance between the two ends of the NW.

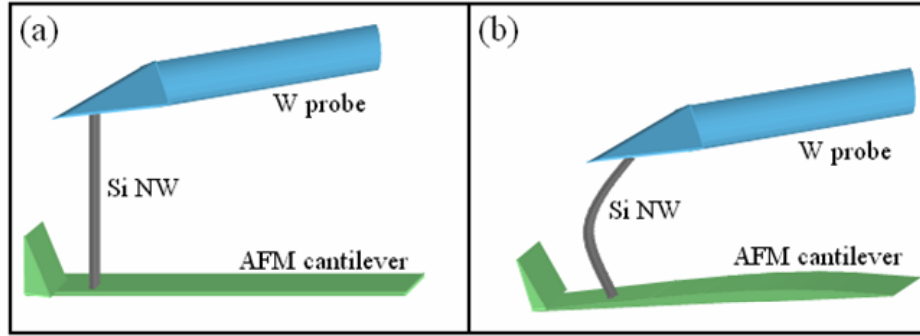


**Figure 38: Schematic diagram illustrating the experimental setup before (a) and after (b) the manipulation.**

Figure 39 shows a series of images and the corresponding bending curves measured from a single Si NW when it was buckled by the probe. It was important to make sure that the NW was oriented perpendicular to the direction of the electron beam to ensure there is no “hidden” displacement along the electron beam direction. This is important to precisely measure the displacement. From Figure 39 (a) to (f), the Si NW was pushed against the AFM cantilever, and the deflection of the cantilever is clearly presented in the image in reference to a stationary feature at the top of the images, which is disconnected to the cantilever and is out of focus in the image due to the difference in depth. By aligning this stationary object for each of the subsequent bending, the deflection can be quantified, thus is the bending force. The NW was affixed at the two ends to the tip and the cantilever. We used the straight distance between the two ends of the NW to characterize its buckling effect. Figure 39(g) shows a curve that presents the applied force, as measured from the deflection of the cantilever, versus the absolute value of the difference of the chord, i.e.,  $|L-L_0|$ . The curve presented a standard behavior of the buckling effect of the slender column under the action of an axial load.

Figure 39(h) shows the calculated curve of the stress and strain based on Figure 39(g). Under the approximation that the strain was homogeneous and the shape would become semicircle at the maximum deformation, we can solve the equations:  $R\alpha = L_0$  and  $R*\sin(\alpha/2) = L/2$ , as depicted in the inset of Figure 39(h). The stress was expressed as a function of the applied force  $F$  and the cross sectional area of the NW  $A$ : stress =  $F/A$ . Meanwhile, the strain was expressed as a function of diameter of the NW  $d$  and the radius of the curvature  $R$ : strain =  $d/2R$ . At the maximum elastic point in this experiment, the strain of the NW was  $\sim 1.5\%$ , much higher than the  $0.2\%$  for most of the typical metallic materials.<sup>78</sup>

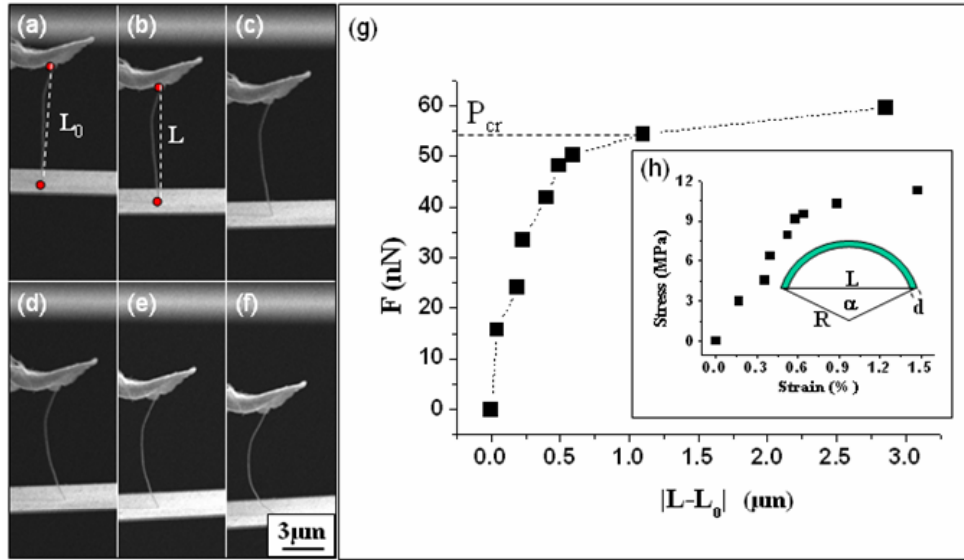


**Figure 39:** a-f) A series of snapshot SEM images showing the continuous buckling of the SiNW. g) Corresponding curve of the applied force  $F$  vs. change in chord length  $|L-L_0|$  when the NW was buckled. h) Calculated stress-strain curve of the buckling of the NW. Inset: Schematic diagram of the deformation approximation.

Figure 40 shows the experimental and the calculation of the strain vs  $|L-L_0|$  curve during the buckling. In the calculation, the relationship between the buckled chord length  $L$  and the strain  $\varepsilon$  is calculated with a thin rod model.<sup>79</sup> We suppose that the buckling

force applied by the AFM cantilever is parallel to the original unbuckled nanowire. The shape of the bent nanowire is described by a schematic model inset in Figure 40, which is given in the following form:

$$\begin{aligned} x &= \sqrt{2}\lambda \times [\sqrt{1 - \cos \theta_0} - \sqrt{\cos \theta - \cos \theta_0}] \\ y &= \frac{1}{\sqrt{2}}\lambda \int_0^\theta \frac{\cos \theta}{\sqrt{\cos \theta - \cos \theta_0}} d\theta \end{aligned} \quad \dots\dots(3.1)$$

where  $\theta$  is the local orientation of the tangent to the nanowire.  $\lambda$  is a characteristic length, defined as  $\lambda = \sqrt{EI_0 / f}$  where  $E$  is Young's modulus,  $I_0$  is the geometric moment of the cross section,  $f$  is the magnitude of the buckling force.  $\theta_0 = \theta(L_0)$  is the local orientation at the top of the nanowire, where  $L_0$  is the chord length of the unbuckled wire i.e. the length of the nanowire. The maximum strain occurs at the surface of the nanowire is:

$$\varepsilon_{\max} = r \frac{d\theta}{dl} = r \frac{1}{dl/d\theta} \quad \dots\dots\dots(3.2)$$

Where  $r$  is the radius of the nanowire,  $l = l(\theta) = \sqrt{1/2}\lambda \int_0^\theta \frac{d\theta}{\sqrt{\cos \theta - \cos \theta_0}}$  is the arc length from the bottom of the wire to the point  $(x, y)$  in discussion.<sup>79</sup>

The maximum strain is a function of  $l$ . We have calculated  $\varepsilon_{\max}$  for the place  $l = 1/2 L_0$ , i.e., at the middle of the wire. Then the strain vs chord length plot is given in Figure 40. The calculated curve matched well to the experimental data, indicating that the assumption made well for Figure 39(h). The results demonstrate that the strain of the NW would be larger than that of the conventional value of bulk materials.

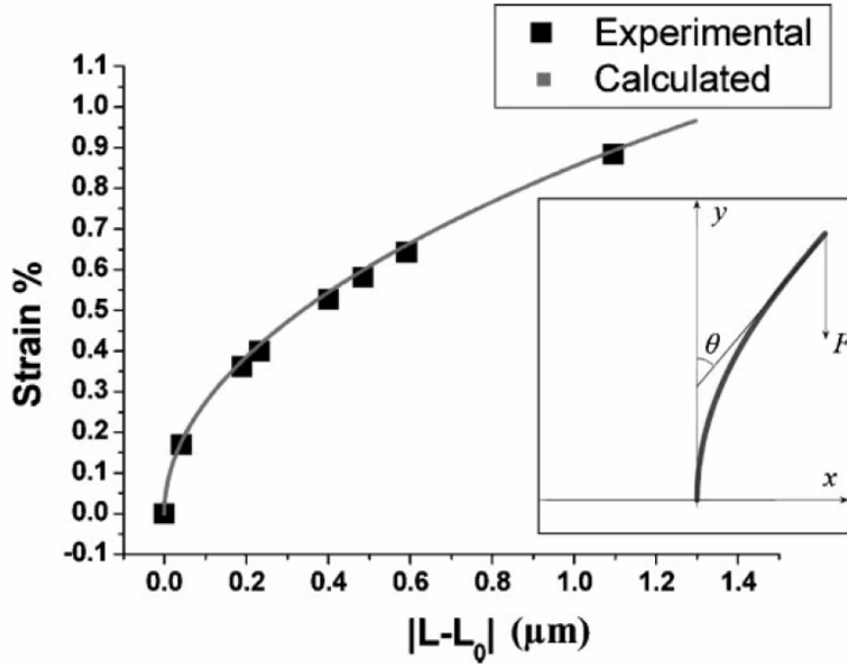
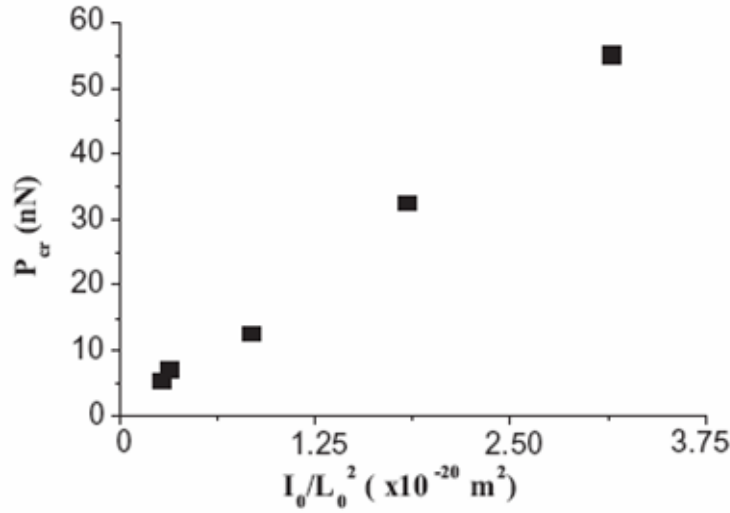


Figure 40: A comparison of the experimental results and the calculated curve of strain vs. change in chord length  $|L-L_0|$ . Inset: schematic model of the nanowire under buckling. The calculation was carried out for the middle point of the chord:  $I=L_0/2$ .

The critical load,  $P_{cr}$ , which is defined as a force larger than the value the NW would be at an unstable equilibrium state, is shown in the curve. After reaching the critical force, a slight increase of the force would cause the NW to buckle. The NW would restore the original shape once the load was retreated, showing the ultrahigh toughness of the NW. From the Euler formula<sup>80</sup>, which can be expressed as a function of the elastic modulus  $E$ , momentum of inertia  $I_0$ , length of the NW  $L_0$  and effective factor  $K$ :  $P_{cr} = \pi^2 EI_0 / (KL_0)^2$ , the critical load can be used to evaluate the elastic modulus of the NW. Because both of the ends of the NW were pinned, the effective factor  $K$  was equal to 1. Figure 41 shows the  $P_{cr}$  vs  $I_0/L^2$  curve for a few NWs. For the difference in diameters and lengths of the NWs, the linear relationship of the curve indicates that the mean elastic modulus of the NWs is 175 GPa, which is consistent with the bulk value.<sup>81</sup>

This result means that the elastic modulus of the NW is the same as the bulk value and is not changed by the nano-sized effect.



**Figure 41: Plot of the critical  $P_{cr}$  vs.  $I_0/L^2$  for several NWs that have been manipulated.**

The elastic modulus of the NW could also be measured by applying the force along different directions, similar to the principle of the AFM measurement.<sup>82</sup> Figure 42 (a) is a schematic diagram of the manipulation process. At the beginning, a Si NW was attached to the probe and the head of the AFM. Then the Si NW was bent by moving parallel to the AFM cantilever and then the AFM cantilever would bend due to a small vertical force created by the NW. Once again, we used the stationary feature at the bottom of the images as the reference to calculate the tangential force  $F_t$  along the vertical direction and the bending of the NW in vertical direction.

Figure 42(b) to (f) show snap shots of a Si NW when it was pushed against the head of the AFM cantilever, and the deflection of the cantilever is shown in the image in reference to the static feature. The elastic modulus  $E$  can also be expressed as  $E = kL_0^3/3I_0$



( $k$ : spring constant). Figure 42 (g) shows a curve that presents the tangential force, as measured from the deflection of the cantilever, versus the deflection distance. From the curve, the elastic modulus could be determined to be  $\sim 200$  GPa. In the regime of large deflection distances, the mechanical behavior of the NW is about the same as the linear part. This observation reveals that the linear regime of the NW is rather large. This could be helpful for the anticipation of mechanical response and the design of the mechanical devices in NEMS.

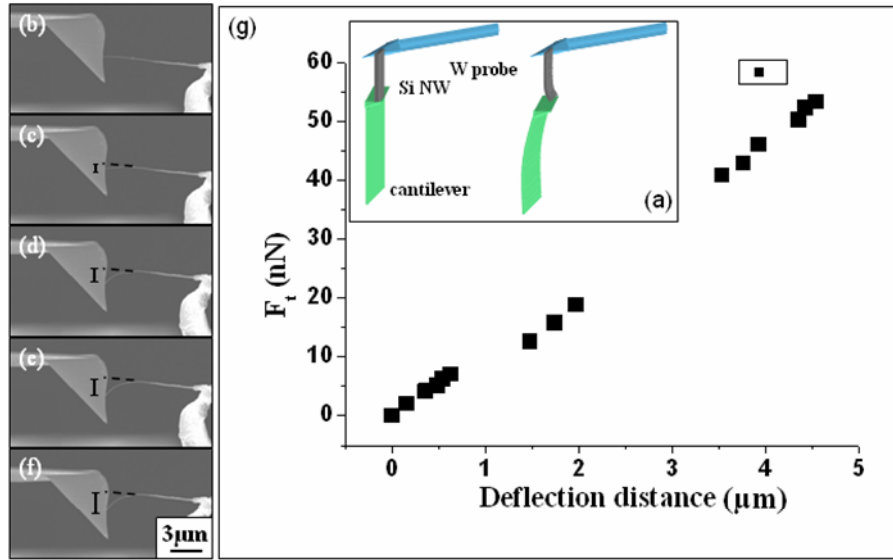


**Figure 42:** a) Schematic diagram illustrating the principle of bending and the setup. b-f) A series of snapshot SEM images showing the manipulation and deflection of a SiNW. g) Corresponding force-deflection distance curve of the NW.

For all of the Si NWs, the compressive load would buckle the NW but did not fracture it even under extremely large deformation. The dramatic increase in flexibility is the result of the decreased thickness of the object.<sup>74</sup> For a slab of a material that has a thickness of  $d$ , the elongation of the interatomic bond at the outer surface of the NW is  $d\alpha/2$ . If the critical bonding length before a bond breaks is  $s$ , under the condition of no generation of dislocation, the maximum bending angle of the slab would be  $\alpha = 2s/d$ . This

means that the degree of bending is determined by the thickness of the object rather than its aspect ratio. For a NW of diameter  $\sim 20$  nm, its bending angle is 1000 times of that of a silicon wafer of thickness 20  $\mu\text{m}$ . At the maximum elastic point in this experiment, the strain of the NW was  $\sim 1.5\%$ , much larger than the conventional value of 0.2%. In addition, a change in elastic constant for nanowires may also contribute to its much enhanced flexibility.

In summary, we have investigated the mechanical properties of single Si NWs using an in-situ technique in SEM. The Si NW showed ultrahigh flexibility and strong toughness. The force-deflection distance curve at the large displacement regime demonstrated that the mechanical behavior of the NW would still follow the Hook's law. The experimental data and simulation result show that the NW can bear a large strain of 1.5%, much larger than that of a bulk material. The elastic constant of the NW was determined to be 175-200 GPa. This study clearly demonstrates the flexibility and mechanical toughness of Si NWs.

### **3.3.2 Example 2: Electrical Measurement on ZnO Tetrapod Nanostructures**

Tetrapod nanostructures have been widely found in ZnO, CdTe, CdS, ZnS, etc<sup>83-85</sup>. ZnO tetrapod nanostructures were synthesized by a typical thermal vapor deposition process. The TEM characterization revealed the zinc-blende ZnO core among four wurtzite legs<sup>86</sup>. The favorable choice of wurtzite nanostructures is probably due to the surface energy minimization. Bonding density calculation indicates that the surface with

lowest energy is wurtzite with  $\{01\bar{1}0\}$  side surface. Figure 43 shows the SEM image of the ZnO tetrapod nanostructures laying on a clean silicon substrate with 200 nm  $\text{SiO}_2$  insulating layer. The legs of the tetrapod nanostructures are about 0.5-5  $\mu\text{m}$  in length. The width of the leg is usually not uniform along the leg, which is much sharper at the end. The cores are about 0.2-1  $\mu\text{m}$  in diameter.

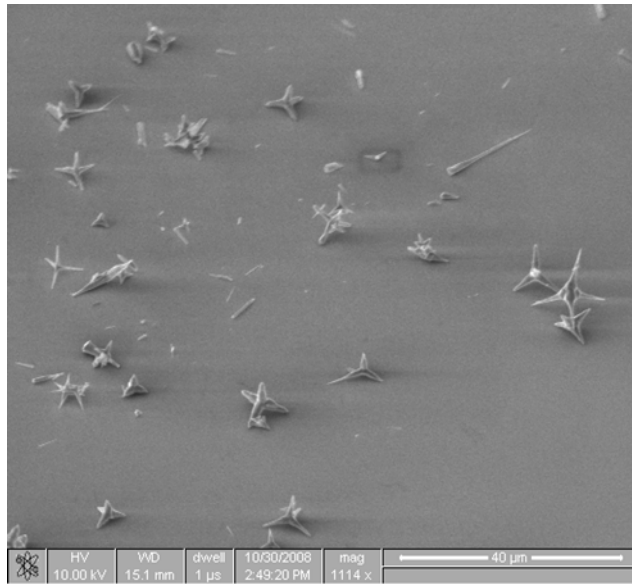


**Figure 43:** ZnO tetrapod nanostructures were dispersed on a clean 200nm- $\text{SiO}_2$  coated Si substrate.

Due to the branched morphology, the EBL and dielectrophoresis process will easily damage the tetrapod nanostructures. Therefore, the direct manipulation provides a convenient way to measure the electrical transport of ZnO tetrapod nanostructures. The independent four probes can move separately in a Cartesian coordinate system. With the careful manipulation, three of the tungsten probes were placed on three different legs of a tetrapod, as illustrated in Figure 44.

The typical I-V curve between two direct ZnO/W contacts indicates a back-to-back Schottky behavior, as illustrated in Figure 45. The curve increases dramatically in

an exponential fashion when the voltage increases, no matter positive or negative biased. The maximum current at 1V is  $1\sim 10E-8$  A.

FIB-induced Pt deposition has been proven to be able to eliminate the Schottky barriers and enhance the conductivity. Thus, a 200 nm thick Pt pad were deposited at the ends of three legs of the ZnO tetrapod nanostructure, and the tungsten probes were place on the Pt pads instead of ZnO legs. The typical I-V curves between two ZnO/Pt/W contacts show ideally linear behavior as illustrated in Figure 46.

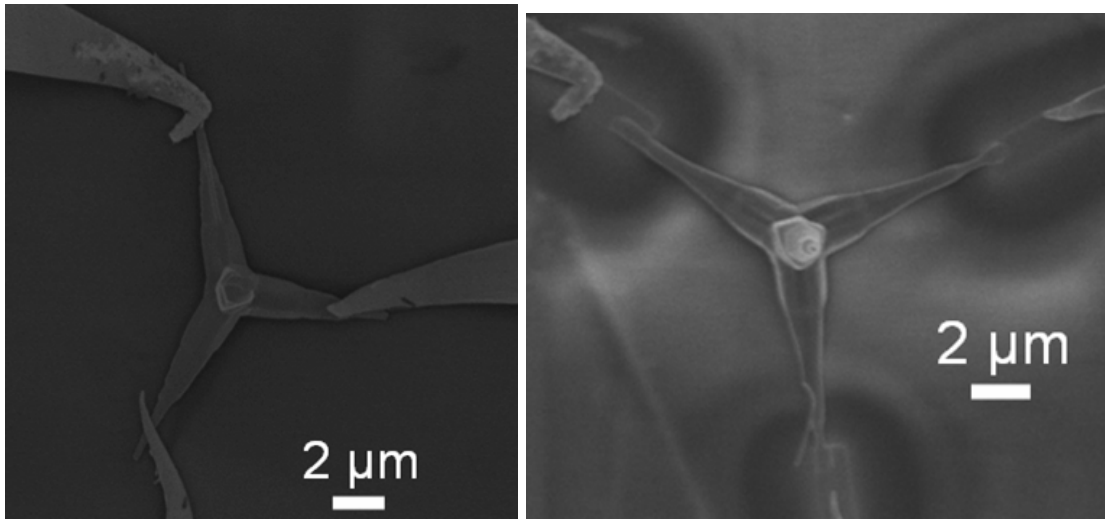


**Figure 44: (a) three tungsten probes were directly placed on three legs of a ZnO tetrapod nanostructure, respectively. (b) the three legs had been modified by FIB-induced deposition of a 200 nm thick Pt, and three tungsten probes were placed on the Pt pads connecting to the legs of the tetrapod nanostructure.**

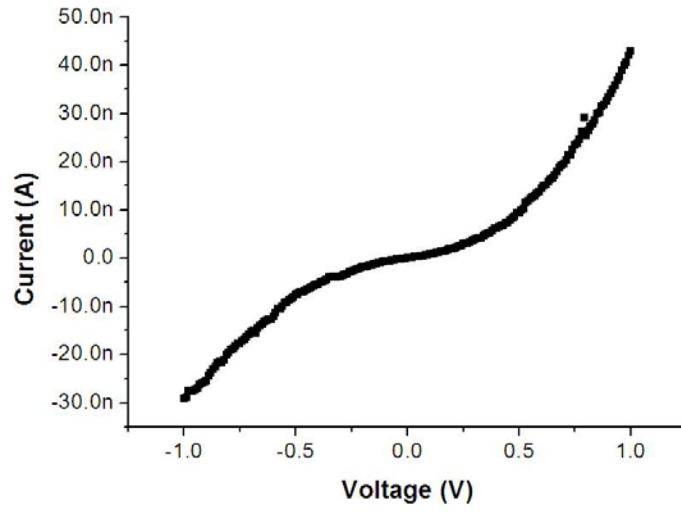


**Figure 45:** A typical I-V curve obtained by directly placing tungsten probes on a ZnO tetrapod nanostructure.

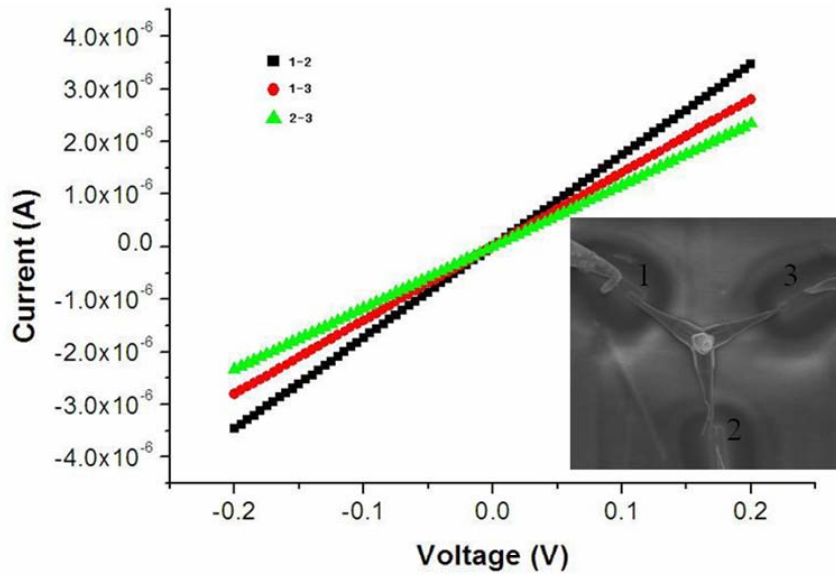


**Figure 46:** Three I-V curves measured at ZnO/Pt/W contacts.

The calculation reveals the resistances of three different legs of the tetrapod are 22, 37, 50 k $\Omega$ , corresponding to legs 1, 2 and 3, respectively. The difference in resistance results from the non-uniformity of the four legs. The unique structure of tetrapod

nanostructures provides a possibility of application as a new electrical component. The three legs were used as source, drain and gate, respectively. This gate is not an insulating gate as commonly seen in microelectronics. Instead, this gate will pump or inject electrons into the device and modify its electrical behavior, as illustrated in Figure 47.

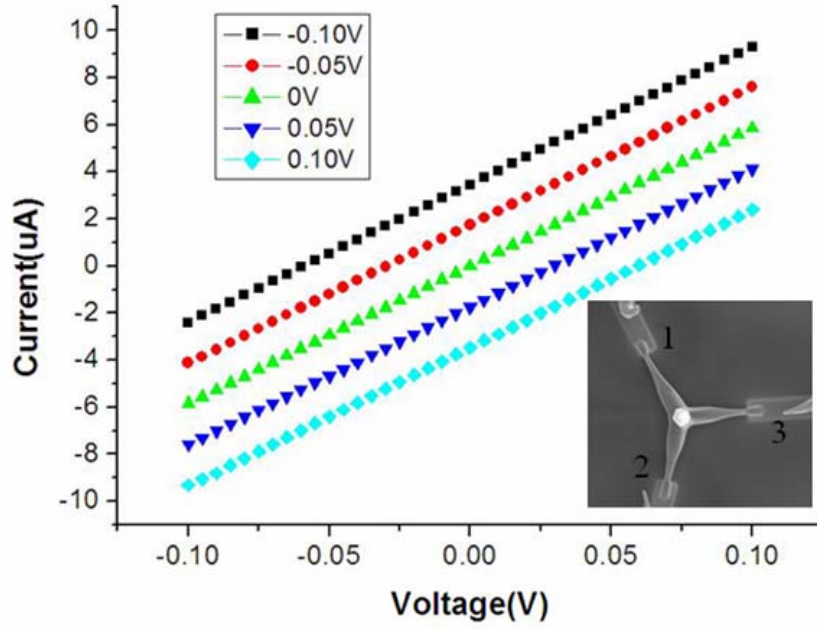


Figure 47:  $I_2$ - $V_2$  curves when  $V_1$  remains 0V and  $V_3$  follows -0.10, -0.05, 0, 0.05, 0.10V steps.

# CHAPTER 4

## MACHANICAL PROPERTIES OF NANOHELICES

### 4.1 Motivation

Helical structures have been observed for a number of inorganic materials. For example, nanocoils of carbon nanotubes are created owing to paired pentagon-heptagon atom-rings arranged periodically in the hexagon carbon network.<sup>87, 88</sup> Formation of nanosprings of amorphous silica was suggested due to a perturbation during the growth of a straight nanowires.<sup>89</sup> Helical structure of SiC is suggested to be a result of screw-dislocation-driven growth process.<sup>90</sup> Utilizing the difference in surface strain on the two surfaces, rings of strained bi-layer thin films, such as Si/SiGe, have been demonstrated.<sup>91</sup>

Zinc oxide, an important semiconductive and piezoelectric material with huge applications in optoelectronics, electronics, optics and sensors, can form single-crystal nanosprings<sup>20</sup>, nanorings<sup>23</sup>, and nanobows<sup>19</sup>, created by bending and folding of nanobelts that are dominated by c-plane polar-surfaces. This process is dominated by a minimization of electrostatic energy contributed by the surface ionic charges. The splendid structural configurations of ZnO nano-object are likely to be the fundamental building blocks and units for fabricating nano-scale sensors, transducers and resonators. In the previous chapter, we report a new and distinctive helical structure of ZnO, formed by a superlattice-structured nanobelt formed spontaneously in a solid-vapor growth

process. The superlattice nanobelt is a periodic, coherent, epitaxial and parallel assembly of two types of one-dimensional nano-stripes of zinc oxide crystals oriented with c-axis perpendicular with each other. The formation process of the nanohelix has been fully investigated in the previous chapter. In this chapter, the nanohelix is manipulated by atomic force microscopy and its elastic spring constant is measured. In addition, the fracture phenomenon is investigated by AFM and underlying fracture mechanism is proposed. The nanohelix is likely to be an ideal structure for fabricating electromechanical coupled nano-scale devices.

## 4.2 Young's Modulus Measurements

The nanohelix is a rigid structure with little stored elastic energy. The nanohelix is formed by rigid structural alteration. Our data first rule out the possibility of the dominated role played by the bi-layer surface strain in the formation of the nanohelix for two reasons. One, there is no bi-layer strained structure in our system; and secondly, the difference in surface stress on the (0001)-Zn and (000 $\bar{1}$ )-O of ZnO, if any, has negligible effect on the formation of nanorings or nanobows. The nanohelix is likely to be formed by two processes: the rigid structural alteration due to the formation of the superlattice, and the spontaneous polar charge induced bending.<sup>20</sup> On the other hand, the thickness ( $t$ ) of the nanobelt is  $\sim 20$  nm and the typical radius ( $R$ ) of the nanohelix is  $\sim 150$ -350 nm, thus,  $t/R \sim 6$ -13%, much larger than the threshold value ( $\sim 3\%$ ) permitted for forming a nanoring by electrostatic polar charges. With consideration the great reduction ( $\sim 50\%$ ) in surface area of the polar surface after forming the superlattices as well as the helical



shape of the structure, the role played by polar charges in forming the helix is dramatically reduced. Therefore, the dominant mechanism for forming the nanohelix is owing to rigid lattice distortion/rotation as a result of superlattice formation.

A nanohelix has been sectioned by FIB into a short segment of one periodicity (Figure 50A), but the shape of the segment is still preserved and shows no visible relaxation, indicating that the nanohelix is a rigid structure without storing elastic energy. A nanohelix has been cut by an AFM tip at two consecutive cycles (Figure 50 C and D), and a detailed image from the same region by SEM (Figure 50E) indicates the preservation of the rigid shape of the helix by the single cycle.

The schematic diagram of AFM is shown in Figure 48. AFM is composed of four key parts: laser diode, cantilever, sample, and photo-detector. The laser strikes on the top side of cantilever, and then reflects to the position-sensitive photo-detector. The change of local property can cause the different amount of bending of cantilever, which can be recorded by the photo-detector.

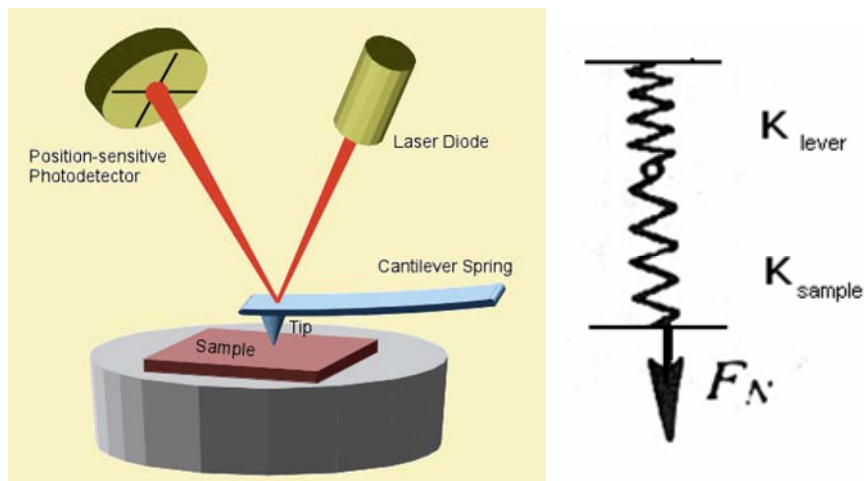


**Figure 48: Schematic of the AFM.**

The transverse spring constant of the nanohelix, which is a quantity for describing the stiffness of the nanohelix perpendicular to its axial direction, has been measured by AFM using the force curve. In the AFM contact mode, the force curve is a plot of the deflection of the AFM cantilever versus the extension of the piezoelectric scanner. The deflection of the cantilever can be measured by using a position-sensitive photo-detector, which supplies a voltage signal proportional to the deflection of the cantilever; the control of extension of piezoelectric scanner is accurate after the AFM scanner is calibrated.

The sensitivity (S) is determined from the inverse of the slope of the voltage-extension curve ( $S = \Delta Z / \Delta V$ ), and S is in units of nm/V. Local variations in S indicate variations in the local elastic properties.

Force curves are important feature in AFM mechanical measurement. For contact mode AFM, a standard calibration is a necessary step for accurate force. For example, a silicon substrate can be regarded as a perfect substrate that won't have any deformation when force is applied. Thus, the extension of the piezotube of the AFM equals to the deflection amplitude of the AFM cantilever. The sensitivity of displacement (S) is determined from the inverse of the slope of the voltage-extension curve ( $S = \Delta Z / \Delta V$ ), and S is in units of nm/V. The sensitivity of force is obtained by multiplying S and K (spring constant of the cantilever), in unit of nN/V.

When the tip and the sample surface are in contact, the AFM cantilever and the sample can be regarded as two spring in series, and we could have formulas:

$$F_N = K_{\text{lever}} \Delta Z_{\text{lever}} = K_{\text{sample}} \Delta Z_{\text{sample}} = K_{\text{total}} \Delta Z_{\text{total}}$$

$$\Delta Z_{\text{lever}} + \Delta Z_{\text{sample}} = \Delta Z_{\text{total}} \quad \text{.....(4.1)}$$

where  $\Delta Z_{\text{total}}$  is the extension of the piezoelectric scanner, and this is what AFM can control.  $\Delta Z_{\text{lever}}$  is the deflection of the cantilever, which is proportional to the voltage strength ( $\Delta Z_{\text{lever}} = b * \Delta V$ ,  $b$  is a constant number).  $\Delta Z_{\text{sample}}$  is the deformation of the sample surface. The sensitivity  $S$  (nm/V)  $= \Delta Z_{\text{total}} / \Delta V = b * \Delta Z_{\text{total}} / \Delta Z_{\text{lever}}$ . Strictly speaking, when doing the sensitivity  $S$  calibration, a stiff sample surface is required, meaning that  $\Delta Z_{\text{total}} = \Delta Z_{\text{lever}}$ , so that  $S$  equals constant  $b$ . In our experiment, the sensitivity on stiff Silicon substrate ( $S_{\text{si}}$ ), and the sensitivity on ZnO nanospring ( $S_{\text{ZnO}}$ ) were both obtained.

$$S_{\text{si}} = b * \Delta Z_{\text{total}} / \Delta Z_{\text{lever}} = b$$

$$S_{\text{ZnO}} = b * \Delta Z_{\text{total}} / \Delta Z_{\text{lever}} = S_{\text{si}} * \Delta Z_{\text{total}} / \Delta Z_{\text{lever}} = S_{\text{si}} * K_{\text{lever}} / K_{\text{total}} = S_{\text{si}} * K_{\text{lever}} / (K_{\text{ZnO}}^{-1} + K_{\text{lever}}^{-1})^{-1} = S_{\text{si}} * (K_{\text{ZnO}} + K_{\text{lever}}) / K_{\text{ZnO}} \quad \text{.....(4.2)}$$

So, the local elastic spring constant can be obtained by

$$K_{\text{ZnO}} = K_{\text{lever}} * S_{\text{si}} / (S_{\text{ZnO}} - S_{\text{si}}) \quad \text{.....(4.3)}$$

The actual experiment was performed in contact mode AFM. Firstly, the sensitivity  $S_{\text{si}}$  on Silicon substrate, then go back to the top surface of nanospring was measured, then the sensitivity  $S_{\text{ZnO}}$  on nanospring, lastly the sensitivity  $S_{\text{si}}$  on Silicon substrate again. There should be no obvious change (less than 1%) between the two values of  $S_{\text{si}}$ , which means that the laser, the cantilever and the photo-detector are all

working stably during the whole experiment. In order to minimize the random error, average method over sensitivity measurements is adopted.

Difficulties in this experiment are 1) the poor adhesion of the nanospring on silicon substrate, 2) the easy fracture during motional imaging, though the ZnO nanospring can undertake up to 600nN normal force without fracture.

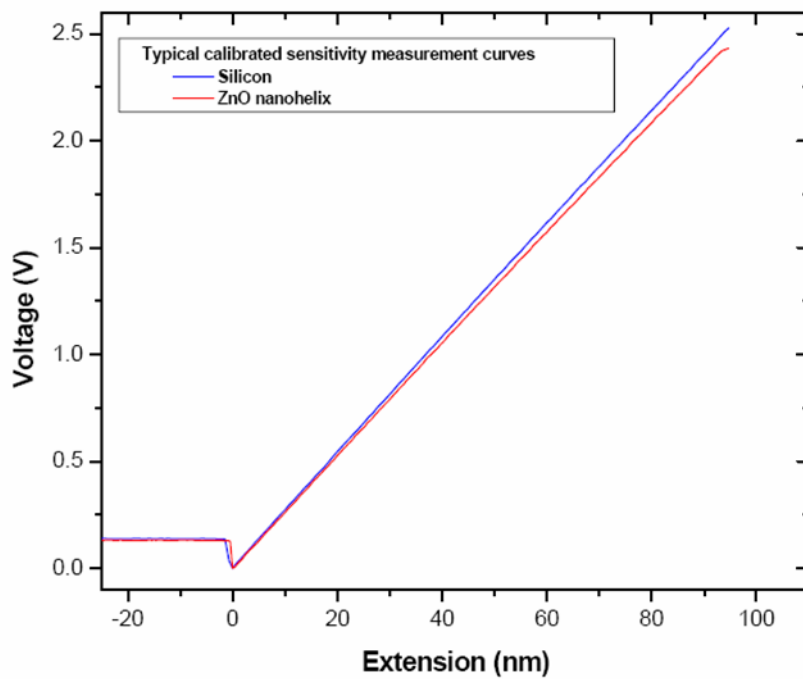


**Figure 49: Typical calibrated sensitivity measurement curves on silicon substrate (blue) and ZnO nanohelix (red).**

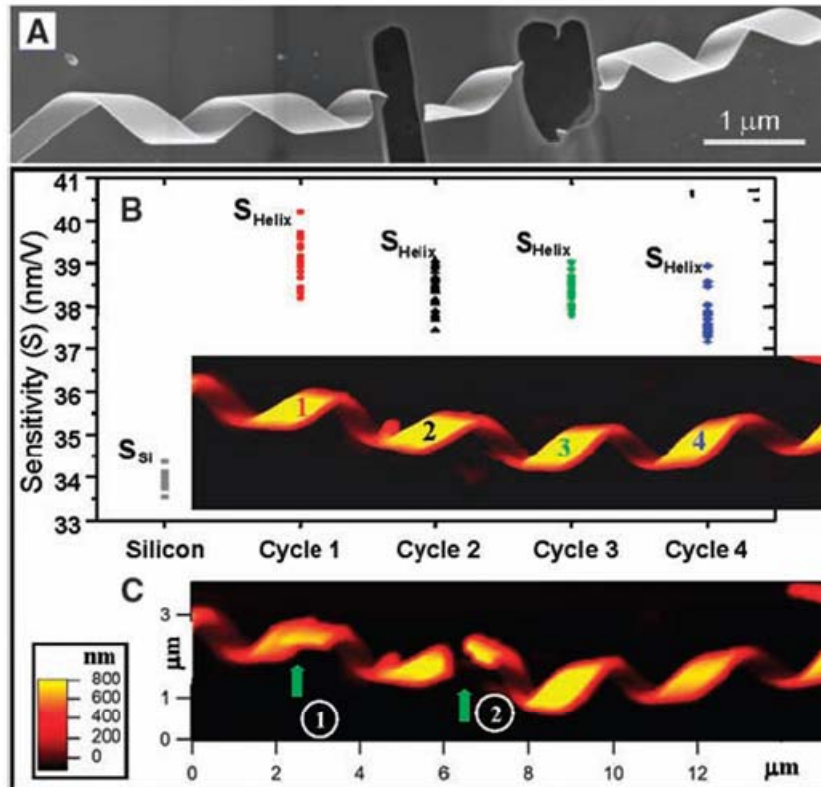


**Figure 50: Manipulation of a nanohelix and measurement of its elastic properties. (A)** SEM image of a nanohelix that was cut by a FIB microscope shows the preservation of the rigid geometrical shape after the cut, which suggests there is minimal stored elastic energy. **(B)** AFM contact mode measurement of the sensitivity ( $S$ ) of the photodetector for the silicon substrate and the four turns of a ZnO nanohelix, as indicated by 1 to 4 in the inserted AFM image. The sensitivity  $S$  of the photodetector is the inverse of the slope of the voltage-extension curve, which is directly related to the elastic property. The measurement was done by positioning the tip on the surface of the upmost middle point of the turn of the helix. Each dot represents one measurement. The sensitivity  $S_{\text{Si}}$  for silicon is substantially lower than that for the ZnO nanohelix ( $S_{\text{Helix}}$ ). **(C)** Fracture of the nanohelix at two consecutive turns of the nanohelix by the AFM tip, showing a preservation of helical shape in the sectioned region.

Several effective spring constant measurements on the same ZnO nanospring (different winding) have been performed, and each of them is an average of 10 experiments. The results of sensitivity measurement are plotted in Figure 50b and the calculated effective spring constants are listed in Table 2.

**Table 2: Calculated effective spring constant on different circles of nanohelices.**

Measurement	1	2	3	4
K(N/m)	21	22	24	16

According to B.M.Fraeijs de Veubeke's book <sup>92</sup> and A.Volodin's paper<sup>93</sup>, using circular beam approximation, the local spring constant of the middle point of the top surface of the nanospring can be calculated by

$$K = \frac{2\pi EI}{(4 - \pi)R^3} \dots\dots\dots(4.4)$$

E is the Young's modulus of ZnO nanospring, R is the radius of the nanospring, I is the inertia of the cross section of nanobelt.

Therefore, the elastic modulus E of the nanohelix is derived from the measured spring constant to be 42, 49, 48 and 57 GPa, respectively. These values are lower than the ZnO bulk value 140-160 GPa. However, we later realized that the effect of the boundary conditions for mechanical measurement is extremely crucial. For suspended ZnO nanobelt over trenches, the mismatch between actual boundary conditions and the calculation model can contribute up to 4 times difference in calculated young's modulus. The details will be discussed more in next chapter.

### 4.3 Fracture Mechanism

This part of the experiments was still carried out using an atomic force microscope, which was used to transversely compress a nanohelix until fracture occurred (AFM images of a nanohelix before and after fracture as shown in Figure 51). Figure 52 a

and b are respectively an AFM topography image of a nanohelix after being compressed by the AFM tip and a corresponding SEM image. The measured force-displacement curves for a group of nanohelices are shown in Figure 52c. A common factor for the fracture of the nanohelices is that the force-displacement presents two sharp drops at  $F_1$  and  $F_2$ . A complete fracture of the nanohelix follows the sharp drop at  $F_2$ .

We have found that a nanoscale elastic buckling deformation is possible upon compression. In the buckling process of a thin millimeter scale elastic plate arch, the fracture mechanics has suggested a force drop to a smaller value due to a transition from elliptical shape to heart shape. For a transverse compression of the nanohelix, a two-step fracture process involving a nanoscale buckling phenomenon can be proposed for explaining the experimental data shown in Figure 52a-c.

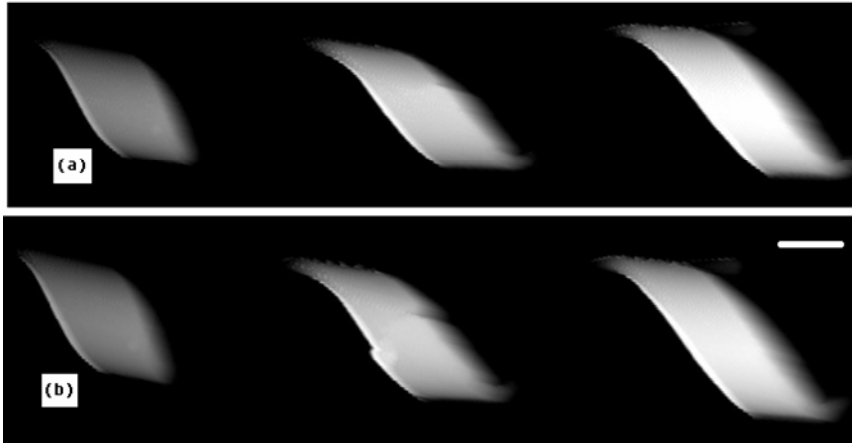


**Figure 51:** AFM images of the same nanohelix (a) before and (b) after fracture. Scale bar indicates 400nm.

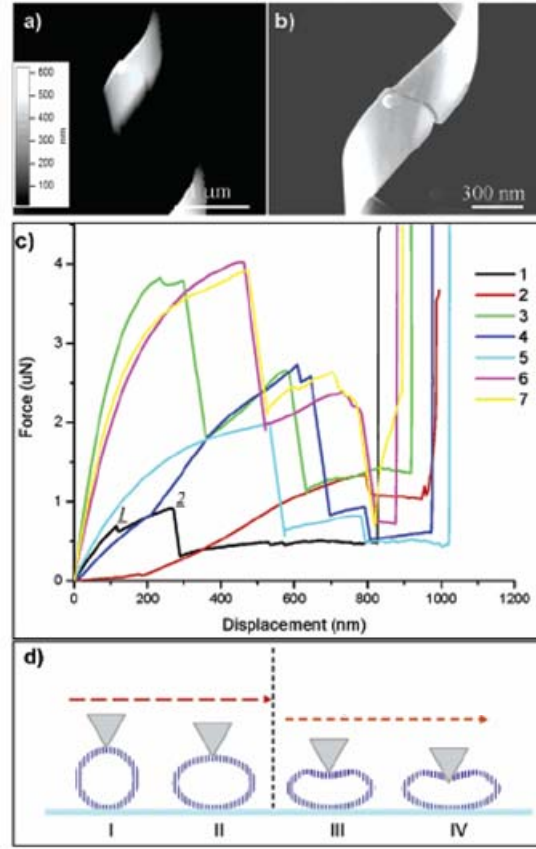


**Figure 52: Two-step fracture process of nanohelices upon transversal compression by an AFM tip. a) and b) are, respectively, an AFM topography image after the tip-induced fracture over a nanohelix and the corresponding SEM image of the fractured part. (c) Force displacement curves for 7 nanohelices recorded during AFM tip compression and fracture process. (d) A schematic model of the two-step fracture process of the nanohelix upon transverse compression by an AFM tip.**

Table 3 lists the characteristic forces for the 7 sets of transverse compression and fracture experiments conducted for the nanohelices of different dimensionality as plotted in Figure 52 c. These nanohelices have a belt width ranging of 380-600 nm (much larger than the AFM tip size of  $\sim 100$  nm), a diameter ranging of 900-1100 nm and a pitch ranging of 1700-3800 nm. During the experiments, except the nanohelix #2 ( $N_2 = 2$ ), all of the other nanohelices have found the second jump in force, corresponding to the final fracture.



**Table 3: Characteristic parameters of nanohelices used for transverse fracture measurements by AFM.**

$N_2$	$F_1$ (mN)	$F_2$ (mN)	$2r_0$ (um)	$H_0$ (nm)	$a$ (nm)	$b$ (nm)
1	0.69	0.91	950	2200	20	380
2	1.34	-	960	1700	20	400
3	3.8	2.7	1200	3800	20	570
4	2.8	2.5	1000	3700	20	570
5	2.0	0.8	1100	2500	20	590
6	4.0	2.4	1100	2100	20	590
7	4.0	2.7	1100	2200	20	590

The proposed fracture process is presented in Figure 52d. The nanohelix deformation process was represented by four instant cross-sectional views perpendicular to the axis of the nanohelix upon the AFM tip compression, a deformation process with four stages I, II, III and IV. The four stages illustrate a two-step fracture process, i.e., a pre-buckling and then buckling process. The pre-buckling step is an elastic compression from stage I to stage II, representing compressing a circular nanohelix into an elliptical cross-section shape. Further compression will likely result in the initiation of the buckling. The buckling stage is the step III and IV. As the deformation transitioned from a stretching energy dominant to bending energy dominant, there is a sudden softening of the nanohelix, leading to a force drop at a steep rate at the vicinity of  $F_1$ . A continuous compressing leads to the eventual fracture of the nanohelix at the tip contact point at a force  $F_2$ . Because of the pyramid shape of the AFM tip with a tip size of  $\sim 100$  nm, a local fracture resulted from the buckled plastic deformation by the tip is revealed in Figure 52 b. Take nanohelix #1 ( $N_2=1$ ) as an example (dark-lined force-displacement curve in Figure 52c) at  $F_1=0.61$   $\mu$ N with a displacement of 115 nm, the force drop occurred as a buckling deformation being initiated (from stage II to III) as a result of transition from

stretching resistant deformation to bending dominant. The bending resistance will lead to a later sustained force curve until the tip displacement reached 270 nm, then an eventual fracture occurred at 0.91  $\mu\text{N}$  (IV stage of Figure 52 d).

#### 4.4 Super-elasticity

In-situ manipulation of nanohelices was performed inside the FIB as explained in chapter 3. Figure 53 shows a series of snap shot SEM images showing a mechanical loading process by the nanoprobe onto a nanohelix. In Figure 53 a, two nanohelices have been transferred on a Si substrate and entangled to each other with a cross-knot position, as indicated by an arrowhead. The white arrowhead points to one end of a nanohelix that was welded onto the tungsten nanoprobe using the ion beam induced Pt deposition. To avoid or reduce the damage from the ion beam, the lowest current available for Pt deposition was used. Despite the entanglement between the two nanohelices, the two nanohelices can be easily distinguished in Figure 53a. The dimensions of the welded nanohelix are approximately 1  $\mu\text{m}$  in diameter, 2.2  $\mu\text{m}$  a pitch, and 220 nm in width. To pull the welded nanohelix out of the cross-knot, the nanoprobe gradually extended the welded nanohelix away from the other nanohelix. In reference to the position marked by the arrowhead, it is amazing to find that the welded nanohelix can be pulled to almost straightened shape, while its twist cycles are preserved. The enlarged image in Figure 53 c reveals that the extended nanohelix has reached an extreme extension, for which the width of the nanobelt decreased to  $\sim 190$  nm, less than the original width of 220 nm, indicating a curly bending of the nanobelt across its width under external mechanical stretching.

A continued stretching manipulation of the nanoprobe has led to the sliding of the cross-knot from its original position in Figure 53b to an un-knotted position as marked in Figure 53d. The entangled position was pointed by a dashed arrowhead. Obviously the stretched nanohelix has begun to recover its shape from the extreme extension displayed in Figure 53b-c. Further manipulation has pulled the welded nanohelix completely away from the unwelded one, as shown in Figure 53e. A careful comparison with the nanohelix dimensions presented in Figure 53a indicates that the nanohelix has an almost identical dimensionality including pitch and radius, which suggested a complete elastic recovery, i.e, a super-elasticity (shape memory) effect.

To see if a compression load would lead to a similar mechanical behavior, a compression manipulation by a nanoprobe was conducted on another welded nanohelix. The nanohelix had a dimension of 300 nm in diameter, 1  $\mu\text{m}$  a pitch, and 380 nm in width. Figure 54 records the sequential images of the nanohelix during compression loading and after releasing on the load. With the gradual increase of the loading by the nanoprobe, compression deformation produced a shortening and twisting of the nanohelix (Figure 54 a to d). When the contact adhesion between the nanohelix and the carbon film could not bare the load from the nanoprobe, the nanohelix broke off from the substrate and remained free in air (Figure 54e). The deformed nanohelix eventually restored its original shape (Figure 54f), suggesting an elastic deformation during the compression.

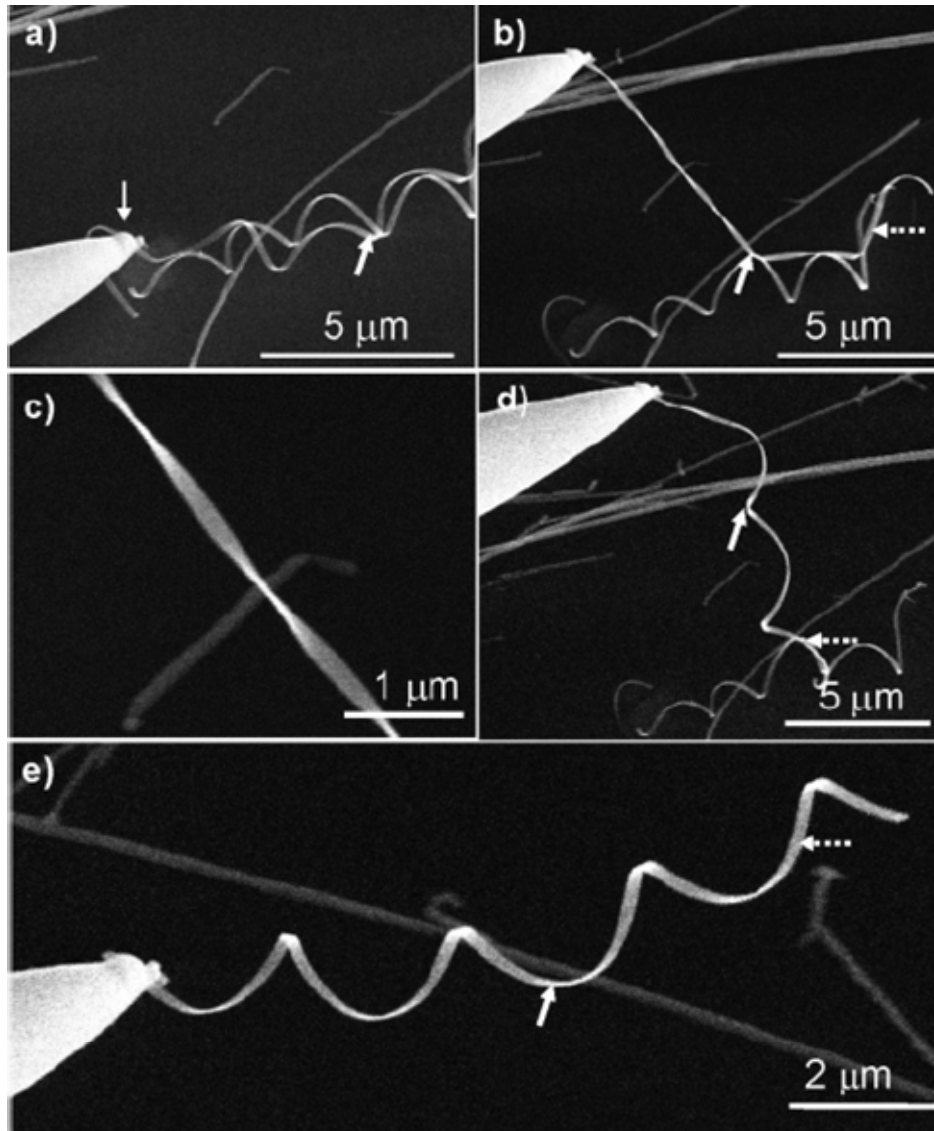


**Figure 53: Manipulation process of a nanohelix upon an extremely large axial stretching and shape-recovery process. The nanohelix was deposited on silicon substrate. (a) One end of a nanohelix was welded with Pt onto a tungsten nanoprobe. (b) An attempt for extracting the welded nanohelix out of the entangled nanohelices. (c) An enlarged SEM image showing the extremely stretched nanohelix. (d) Continued extraction led to an initial release of the welded nanohelix from the entangled point and a recovery of the nanohelix shape. (e) A complete restoring of the nanohelix shape after the manipulation in b and c, suggesting a superelasticity (shape memory) behavior.**

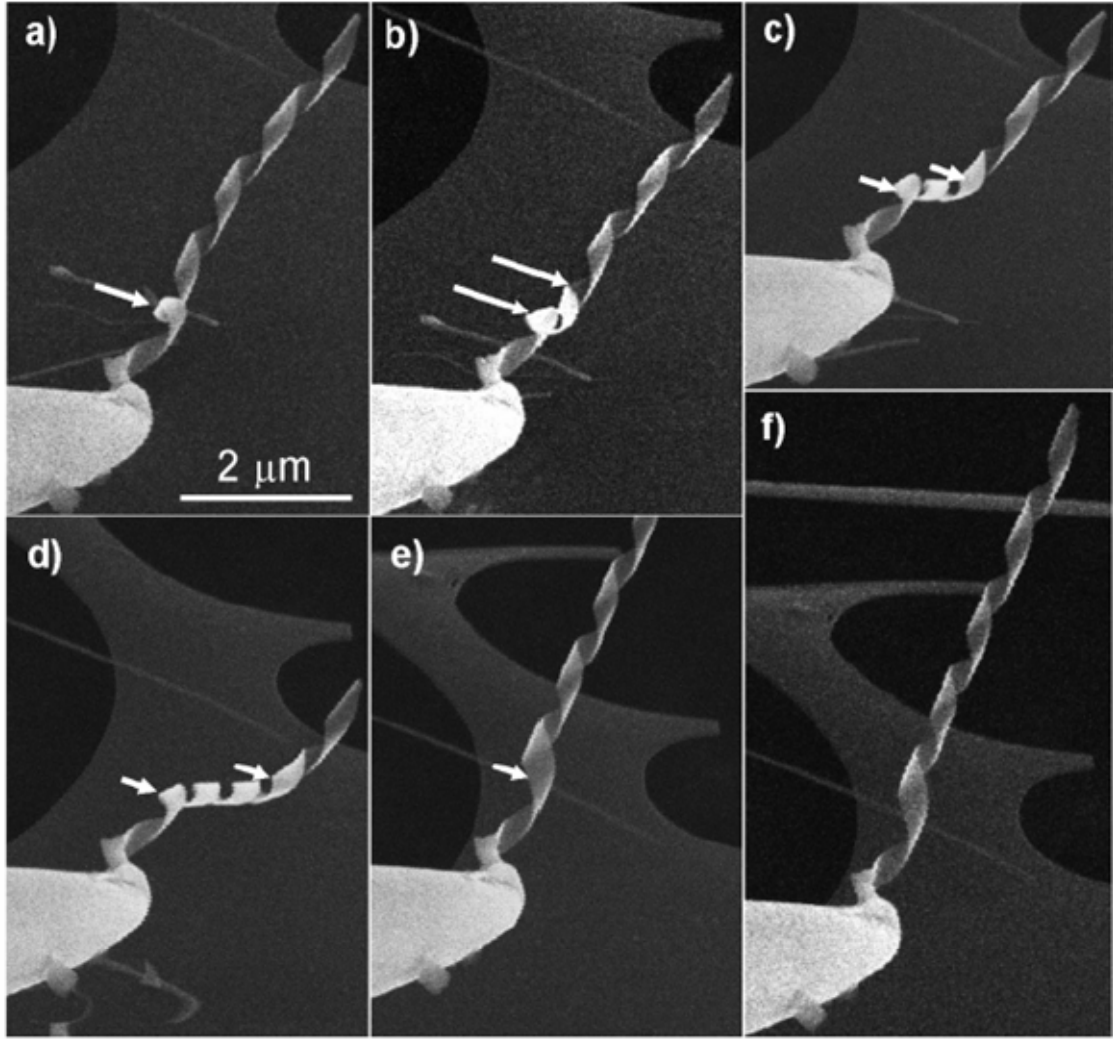


**Figure 54:** Compressed deformation process of a nanohelix induced by the nanoprobe. The compression-led shortening and twisting are indicated by arrowheads, starting from (a) a half-turn of the nanohelix; (b) one and half turns; (c) two turns; and (d) two and a half turns. (e) The nanohelix elastically jumped away from the contact point with the other end free because of an overload by the probe. (f) The nanohelix eventually restored its original shape, suggesting an elastic deformation during the compression.

The origins that are responsible for the observed super-elasticity can be suggested as two. One, the small thickness of the nanobelt making the nanohelix allows a large degree of deformation possible without introducing dislocation.<sup>19</sup> The small size leads to large degree of flexibility and elasticity. This is likely a common phenomenon at nano-scale. Lastly, the nanohelix is made of two types of parallel running stripes of  $\sim 3.5$  nm in

width<sup>21</sup>, which are ZnO but with different crystal orientation. The interface formed between the two types of stripes can absorb large degree of deformation by atomic scale twisting and bending. Such a process may not need to introduce dislocations.

# **CHAPTER 5**

## **QUANTIFYING ELASTIC DEFLECTION OF BRIDGED NANOWIRES**

### **5.1 Motivation**

One-dimensional (1D) nanomaterials, such as carbon nanotubes<sup>9, 10, 12</sup>, semiconductor nanowires<sup>6</sup> and oxide nanobelts<sup>16</sup>, are the fundamental building blocks for constructing nanodevices and nanosystems that exhibit superior performances. Mechanical behavior of 1D nanomaterials is one of the most important properties that dictate their applications in nanotechnology. Various methods have been developed for quantifying the mechanical property of 1D nanomaterials, and they may be classified into three categories. The first approach is based on dynamic resonance of a 1D nanostructure that is affixed at one end and free at the other; the mechanical resonance is excited by an externally applied oscillating electrical field, and the observation is made through electron microscope.<sup>11, 94</sup> The second approach is quantifying the static axial tensile stretching of a 1D nanostructure using the AFM tip, which is installed inside a scanning electron microscope (SEM).<sup>12</sup> The third approach is based on atomic force microscopy (AFM) and nano-indenter.<sup>13, 82, 95-97</sup> One of the most important and common strategies is deforming a 1D nanostructure that is supported at the two ends using an AFM tip, which pushes the 1D nanostructure at its middle point. Quantifying the middle-point force-displacement curve gives the elastic modulus. The accuracy of this measurement is

limited, however, by the size of the tip and the accuracy of positioning the AFM tip right at the middle of the 1D nanostructure due to the unavoidable hysteresis of the piezoceramic actuator of the AFM cantilever.

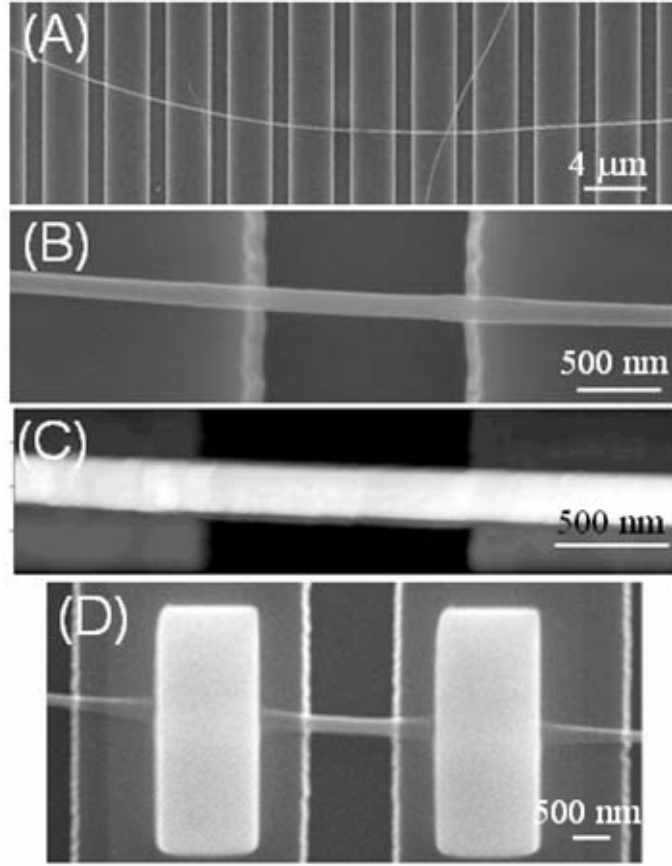
In this chapter, we present a new approach for quantifying the elastic deformation behavior of a 1D nanostructure. Our approach is based on a continuous scan of a ZnO nanobelt (NB) that is supported at the two ends by an AFM tip in contact mode; a quantitative fitting of the elastic bending shape of the NB as a function of the bending force provides a reliable and accurate method for measuring the elastic modulus of the NB. The NB is one special category of nanowires with rectangular cross section, and the following method can wider applied to nanowires.

## **5.2 Experimental Details**

The ZnO NBs used for this study were prepared by physical vapor deposition. A silicon substrate is prepared with long and parallel trenches caved at its surface by nanofabrication. The trenches are about 200 nm deep, 1.25  $\mu\text{m}$  wide (Figure 55A). Long ZnO NBs were manipulated across the trenches over many periods. The morphology and dimensions of the NB were captured by SEM and AFM. The SEM image gives the width of the trench, the length and width of the NB, and the AFM image gives the thickness of the NB (Figure 55B and C). The measurement was done by scan the NB along its length direction using an AFM tip in contact mode at a constant applied force. A series of bending images of the NB were recorded by changing the magnitude of the contact force, from which the elastic deformation behavior of the NB is derived based on model calculation. The AC240 cantilevers (spring constant of  $\sim 2$  N/m) from Asylum Research



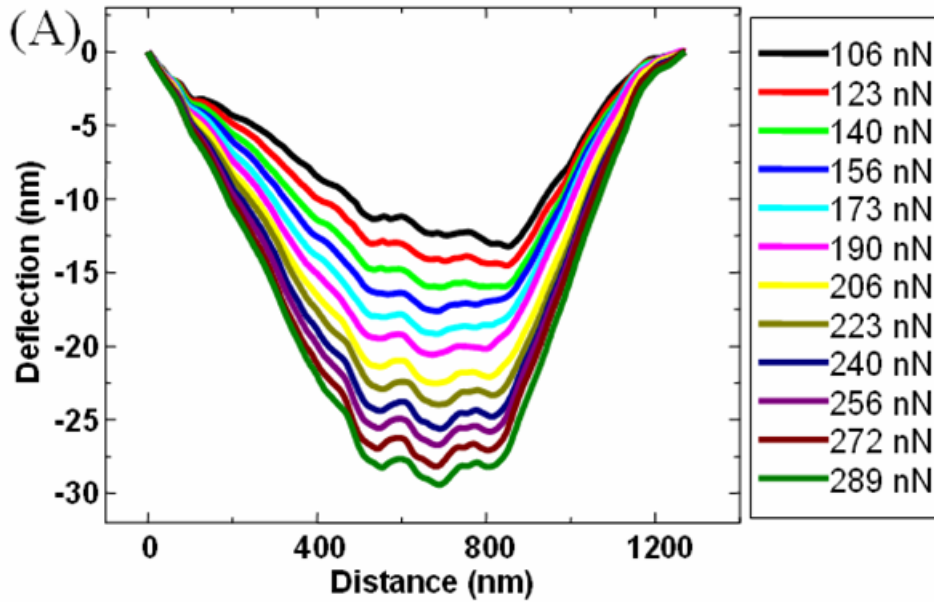
were used in our research, and each cantilever was carefully calibrated using the Sader's method<sup>98</sup>, so that the AFM contact forces could be calculated.



**Figure 55: (a) Low-magnification SEM image of a silicon substrate with parallel trenches. Long nanobelts (NBs) are lying on the trenches. (b) SEM image of one NB bridged over a trench (c) and the corresponding AFM image of the bridged NB over the trench. (d) The corresponding SEM image of the same NB in (b) after depositing Pt pads at the two ends.**

The profiles of a suspend NB along length direction under different contact force are showed in Figure 56A. Each curve was received by an average of 10 consecutive measurements along its length under the same loading force. Due to a small surface roughness ( $\sim 1$  nm) of the NB, the curves are not perfectly smooth. In addition, the as-attached NB on the trenches is not perfect straight, possibly due to its own weight and initial bending during the sample manipulation. In order to eliminate the effect of the

surface roughness and initial bending of the NB on force curve quantification, deflection curves are calibrated by subtracting the profile measured under low applied force ( $\sim 100$  nN) from those measured at higher applied forces. Due to the presence of the trench, a reasonable force has to be applied to make the tip in contact with the NB. To obtain a good image under common AFM, the set point was chose to be  $\sim 0.5$  V, which corresponded to  $\sim 100$  nN. As a result a normalized force is also defined by subtracting the 106 nN from the applied force, and the final results are shown in Figure 56B. Some small ripples appear at the middle of the NB and become pronounced with the increase in contact force. This may be due to the rippling effect of the NB with a compressed top surface in contacting with the AFM tip, because the ZnO NB cannot easily create and preserve edge dislocations to accommodate the deformation.



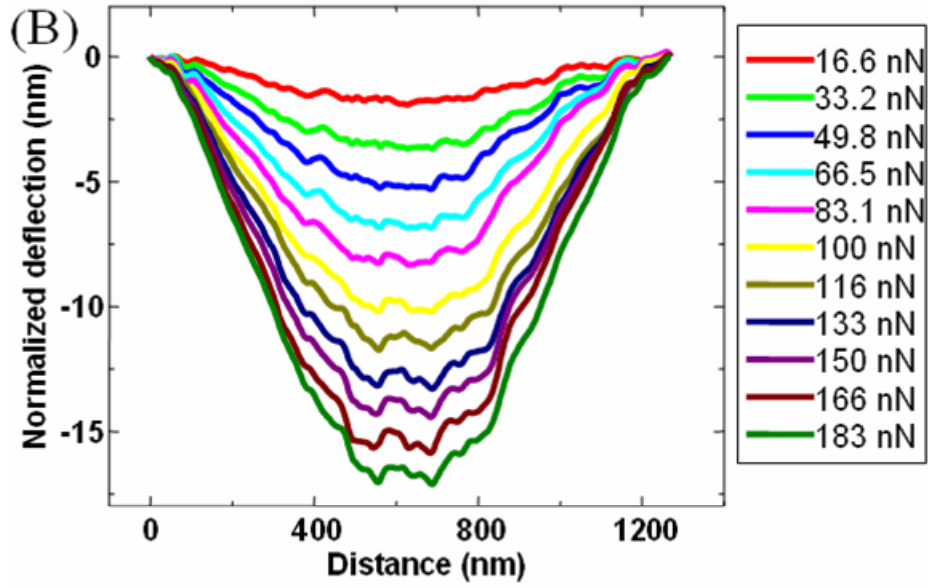


**Figure 56: (a) As-received AFM image profiles of one suspended NB under different load forces in contact mode. (b) The normalized AFM image profile after removing the surface roughness by subtracting the image acquired at 106 nN from the data in (a). The force is also normalized in reference to the “zero setting point” of 106 nN.**

For all of the measurements, the load was kept small so that the maximum deflection of the NB is less than half thickness of the NB. It is very reasonable to assume that the deformation process is elastic. The AFM scanning rate was kept at 0.5~1 Hz, thus, the measurement is static. The measurements were repeated by increasing and decreasing the load to ensure the reproducibility in the profile (within 1 nm) and negligible hysteresis. This is important for the data analysis using elastic deformation theory.

The profile images of the NB recorded the deformation of all of the points along its length under different applied forces. One profile could contain up to 650 points. Every point on the suspended portion of NB in the images can be regarded as a mechanical measurement done using the approaches in the literature.<sup>99, 100</sup> By fitting the shapes of all of the curves measured at different applied forces, the elastic modulus can

be derived reliably and precisely. The question now is what model will be used to quantify the data.

### 5.3 Physical Modeling

There are two typical models derived under different boundary conditions. One is the clamped-clamped beam model (CCBM) (Figure 57A), in which the two ends of the NB are affixed, so that deflection  $v$  and its first derivative  $dv/dx$  are both 0 at  $x = 0$  and  $x = L$ , where  $L$  is the width of the trench. The other is the free-free beam model (FFBM) (Figure 57B), in which the two ends of the NB can freely slide, which means that only the support force exists and there is no force moment, thus, only  $v = 0$  at  $x = 0$  and  $x = L$ . When a concentrated load  $F$  is applied at point  $a$  away from the A end, the differential equation that determines the deflection of the entire beam under small angle deformation is:

$$EI \frac{d^2v}{dx^2} = -N_A x + F[x - a] + M_A, \quad \dots\dots\dots (5.1)$$

where  $E$  is the bending modulus,  $I$  the moment of inertial given by  $wh^3/12$  for the rectangular beam,  $N_A$  the support force and  $M_A$  the force moment at the A end, and  $[x-a]$  is a special function, which means that  $[x-a]=x-a$  when  $x \geq a$  and  $[x-a]=0$  when  $x < a$ . In the CCBM, the solution of equation (5.1) is:

$$v = \frac{Fa^3(L-a)^3}{3EIL^3}, \quad \dots\dots\dots (5.2)$$

This equation gives the deflection of the NB at the contact point  $a$  of the AFM tip under a constant applied force  $F$ . In FFBM, the deflection of the NB at the contact point  $a$  is:

$$v = \frac{Fa^2(L-a)^2}{3EIL}, \quad \dots\dots\dots (5.3)$$

Also, it is also possible to have clamped-free mixed case, and the  $v$  will have an asymmetric form. But such a case was not detected in our experiment.

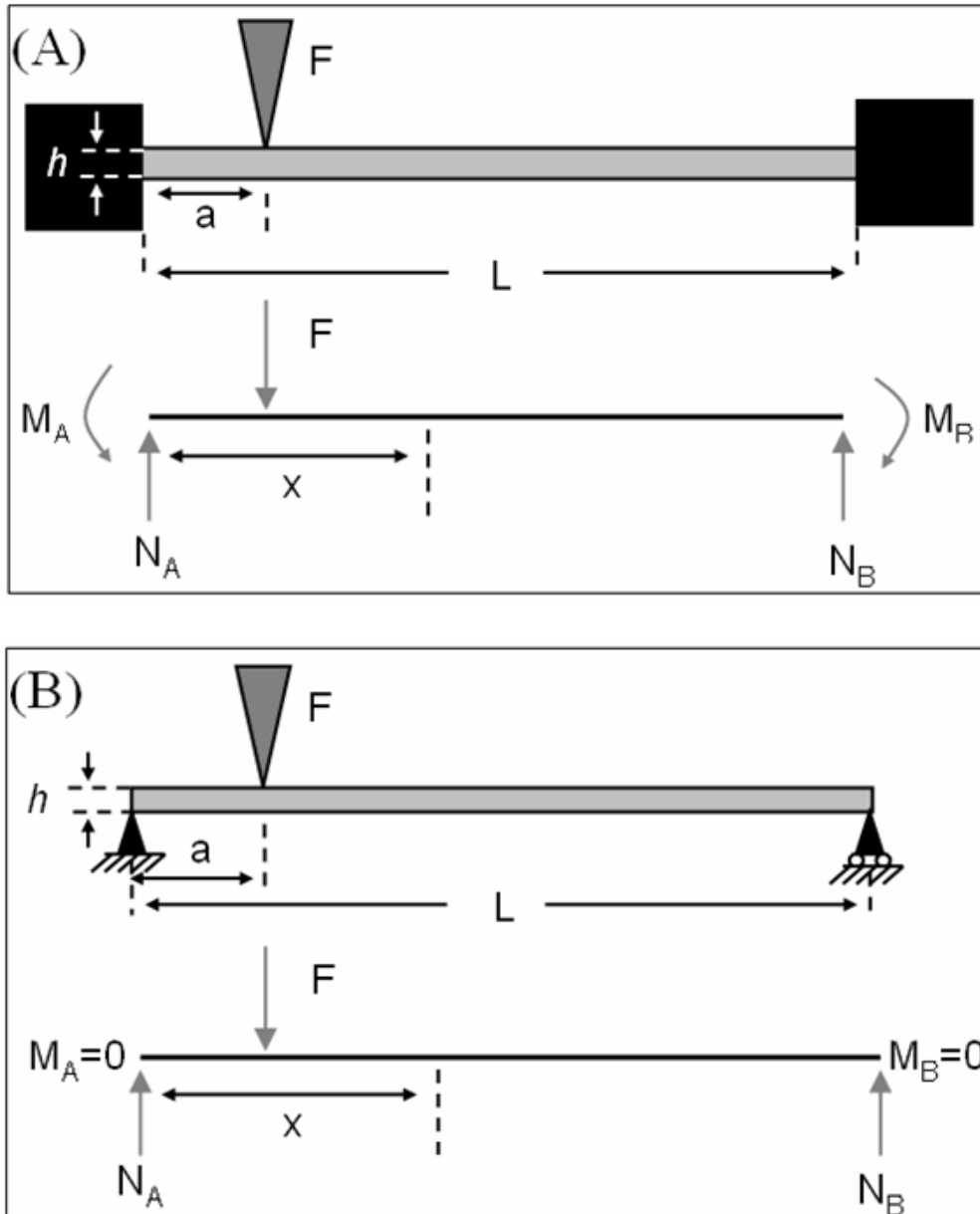


Figure 57: Schematic diagrams of the (a) clamped-clamped beam model (CCBM) and (b) the free-free beam model (FFBM).

## 5.4 Discussions

In the literature<sup>13, 97, 101</sup>, the CCBM theory was assumed because it was assumed that the adhesion force between the 1D nanostructure and the substrate was strong enough to clamp the two ends of the nanostructure. The argument was that the nanostructure could bear a relative large lateral force without any observable movement. Some researchers begin to deposit some metal pads to satisfy CCBM conditions.<sup>97</sup> From the discussion given above, the two different models give totally different results. For instance, at the middle point  $a=L/2$ ,  $E=FL^3/192Iv$  for CCBM, and  $E=FL^3/48Iv$  for FFBM, which are different by a factor of four in the measured elastic modulus. But one is unable to truly identify the model for data analysis if the measurement is made only at one contact point, such as the middle point, of the 1D nanostructure.

From equations (5.2) and (5.3), it is apparent that the shapes of two deformation curves for the two models are different and the slopes of the curves are dramatically different. Therefore, by fitting the shape of the curve measured experimentally under different applied forces, it will be unique to determine which model is more precise to quantify the elastic deformation behavior of the NB. This is our principle for data analysis. Figure 58A shows an example of curve fitting based on the two models. The FFBM is found to fit much better than that of the CCBM, especially when the applied force is large ( $>190$  nN). Under lower applied force, the surface roughness of the NB and the noise from the AFM system make it more difficult to judge the best fit.

To examine the validity of the FFBM for modeling the results presented in Figure 58A, elastic deformation was made from a NB before and after affixing the two ends. Figure 55D shows an SEM image of a NB after depositing two Pt pads at the two ends by

focus ion beam (FIB) microscopy. Before Pt deposition, the maximum relative deflection of the NB at the middle point was measured to 5.4 nm at a normalized force of 117 nN. After Pt deposition, the maximum relative deflection of the NB decreased to 1-1.5 nm at a normalized force of 119 nN. The ratio is  $\sim 4$ , in agreement with the expected result from the theory. This test indicates that the elastic deformation behavior of a bridged NB with two ends “free” can be reliably modeled using FFBM.

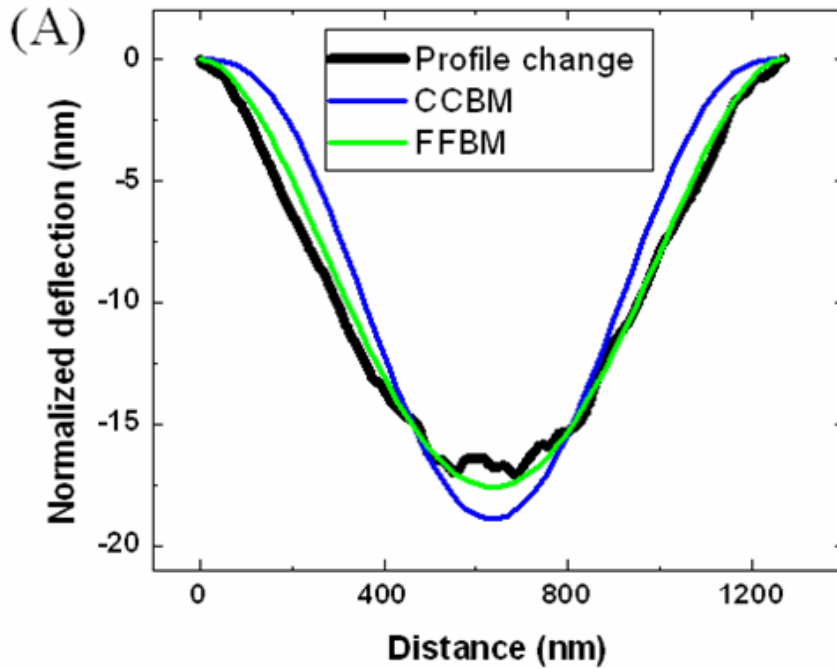
From a general understanding that, at a large load force, the friction between the NB and the edge of the trench may be large enough to prevent the sliding of the NB, thus, the result could be approximately modeled by the CCBM although the two ends are unfixed. In contrast, we found that the adhesion between the ZnO NB and the silicon substrate is weak, possibly due to the incompatible crystal structure systems and the large lattice mismatch. ZnO NBs can often be displaced by AFM tip during imaging, although the scanning direction is along the NB for minimizing the possibility of large impact from the AFM tip. In our case, the adhesion force and the force moment at each side of the NB can be regarded as zero, so that the FFBM is the most reasonable model.

We now consider the local deformation induced by the contact between the AFM tip and the NB. When the tip touches the segment of the substrate supported NB, the contact deformation can be determined by the Hertz model in the standard elasticity theory.<sup>102, 103</sup> Considering the contact between a sphere and an infinite plane corresponding to the tip and the NB, respectively, the Hertz model gives a stiffness of:

$$K_{\text{contact}} = 2E^*r, \quad \dots\dots\dots (5.4)$$

with effective modulus  $E^* = [(1-\nu_1^2)/E_1 + (1-\nu_2^2)/E_2]^{-1}$  and contact radius  $r = [3RF/4E^*]^{1/3}$ , where  $\nu_{1,2}$  and  $E_{1,2}$  are, respectively, the Poisson ratios and bending modulus of the silicon

tip and the ZnO NB;  $R$  is the tip radius, which becomes stable at about 60 nm after several initial scans. For the case of silicon AFM tip pushing on ZnO NB #1 in Figure 58B, the Poisson ratios and bending moduli for both Si and ZnO are  $\sim 0.3$  and  $\sim 160$  GPa, respectively. The contact radius  $r$  is calculated to be 5.5 nm at load  $F = 300$  nN. The contact radius is small comparing to the length dimension of the NB, which is  $1.27\text{ }\mu\text{m}$ , so that the concentrated load condition is valid for bending model analysis. At first glance, the contact deformation should be considered, but in fact, from equation (4), the contact deformation keeps constant under a fixed load, so this local deformation will act as an offset and will not be reflected in the images of the NB. In fact, this offset has been corrected after taking the force and displacement normalization as presented in Figure 56B.





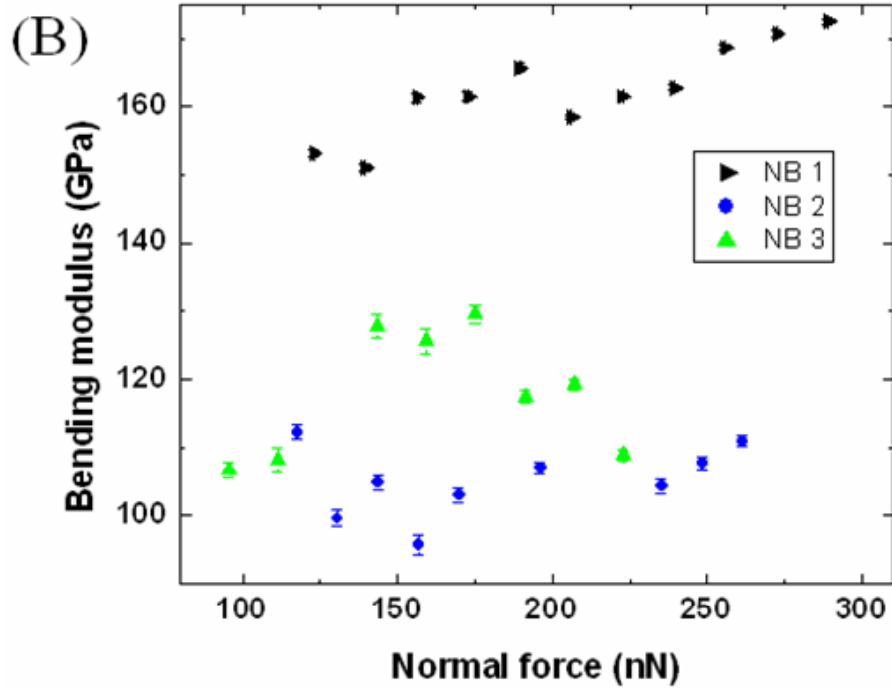


Figure 58: (a) Curve fitting using the CCBM and FFBM for the image profiles of NB 1 acquired under normalized force of 183 nN. (b) The bending modulus from the FFBM fitted curves under different load forces. The error bars are introduced with consideration of the uncertainty in curve fitting. The dimensions of NB 1 are 1.270  $\mu\text{m}$  in length, 90 nm in width, and 70 nm in thickness; the dimensions of NB 2 are 1.253  $\mu\text{m}$  in length, 115 nm in width, and 95 nm in thickness; and the dimensions of NB 3 are 1.232  $\mu\text{m}$  in length, 125 nm in width, and 115 nm in thickness.

Figure 58B shows the bending modulus derived from the curve fitting at different loads for three different NBs. The elastic moduli for NB #1, #2 and #3 remain consistent, respectively, under different loaded forces, indicating that the deformation is elastic although ripples have been observed from the deformation curve (Figure 56 B). The elastic moduli for NB #1, #2, #3 are  $162 \pm 12$ ,  $105 \pm 10$ ,  $118 \pm 14$  GPa, respectively. The difference for the three NBs is likely related to their sizes. The bending modulus presented here is larger than that measured by mechanical resonance measured by in-situ TEM.<sup>27</sup>

The current measurement technique has overcome the difficulty of precisely identifying the middle point of the NB during AFM measurement, which was difficult and imprecise in the reported AFM based measurements. Most AFMs have problems to perform accurate repositioning after imaging, because the AFM piezoceramic actuator has unavoidable hysteresis phenomenon, so a deviation from the target point is expected. From our analysis above, a small deviation from the evaluation of the exact middle point of the 1D nanostructure results in an overestimation of the bending modulus. For a NB with bending modulus  $E = 100$  GPa, width  $w = 100$  nm,  $h = 100$  nm,  $L = 1.25$   $\mu$ m,  $a=L/2$ , the error in  $E$  could be calculated as a function of deviation from the middle point of the NB, as presented in the Table 4. CCBM is more sensitive to the deviation in defining the middle-point than the FFBM. It is apparent that narrow gap trench gives the larger error.

**Table 4: Elastic modulus derived from the two models as a function of deviation in defining the true middle point along the suspended portion of the NB.**

	Middle point	When $\Delta a=0.05L$	When $\Delta a=0.10L$	When $\Delta a=0.15L$
CCBM	$K=81.9$ N/m	$\Delta E/E=3.1\%$	$\Delta E/E=13\%$	$\Delta E/E=33\%$
FFBM	$K=20.5$ N/m	$\Delta E/E=2.0\%$	$\Delta E/E=8.5\%$	$\Delta E/E=21\%$

In summary, we have presented a new approach that is based on the fit of the measured deflection curve along the entire length of the bridged NB under different applied forces. Fitting the measured deformation profile can uniquely determine if the measured data are best explained by either the clamped-clamped beam model (CCBM) or the free-free beam model (FFBM) without pre-assumption, greatly increased the precision and reliability of the measurements. By curve fitting of the experimental profile, we take the advantage of every point along the NB as a single mechanical measurement.

Our method greatly improves the efficiency and minimizes possibility of deviation from hysteresis of the piezoceramic actuator. It is important to find out that the CCBM, most commonly used in data quantification in the literature, might not be valid at least in the case we have presented here. The methodology presented here is a general method and may be applicable to quantifying the static mechanical behavior of any one-dimensional nanostructures.

### **5.5 Statistical Adjustment for Better Estimation**

The set of curves shown in Figure 56, in fact, is the best result that can be obtained. Usually, nano-measurments will encounter a lot of noise coming from many sources: the mechanical vibration, the electrical interference, the wear and tear at nano-scale, etc. These noise, coupled with the poor controllable propertied of nanomaterials, affects the measured data strongly. The elastic deflection curves for another bridged nanobelt display a much larger inconsistence, as illustrated in Figure 59.

How to deal with the data and calculate the best value is always a challenge to nanoscience. In the previous section, a simple approach is adopted as abandoning the curves with obvious large deviation such as obtained at by 92, 105, 183, 209, 222 nN. However, it is quite objective to depend purely on human's judgment. Here, a new physical-statistical model that integrates FFBM with a regression model is proposed as an outcome of a broad and deep cooperation with Dr. Jeff Wu's research group. The regression model captures the initial bias and potential systematic biases introduced during measurement. We use model selection to identify terms associated with the systematic biases and adjust the profiles by subtracting these terms from the original

profiles. This provides a better estimate of the elastic modulus  $E$ . We call the method sequential profile adjustment by regression (SPAR).

As shown in Figure 59, suppose there are  $K$  image profiles, i.e., the nanobelt is scanned sequentially under  $K$  different applied forces  $F_1, F_2, \dots, F_K$ . The experimenter usually changes the magnitude of applied force  $F$  from low to high, i.e.,  $F_1 < F_2 < \dots < F_K$ . Each profile contains  $n$  points which are recorded at the distances of  $x_1, x_2, \dots, x_n$ . We denote the deflection at the distance  $x$  under the applied force  $F$  as  $v(x, F)$ . Then the FFBM can be written as

$$v(x, F) = \beta(x)F, \quad \dots\dots\dots (5.5)$$

where  $\beta(x) = x^2(L-x)^2/(-3EIL)$ . Let  $\delta_0(x)$  be the initial bias and  $\delta_k(x)$  for  $k \geq 1$  be the systematic bias introduced when an AFM tip scans the NB along its length at the applied force  $F_k$ . The initial bias can be due to the surface roughness and initial bending. The systematic biases can be due to the occasional stick-slip events that occur at the ends of the nanobelt, the wear and tear of AFM tip and the nanobelt surface, the lateral shifting and sliding, and other artifacts. Such causes can occur at any stage of the experiment. These random causes cannot be effectively captured using deterministic mechanistic models, whereas they can be easily incorporated using statistical models. Thus we propose to model the deflection at  $x$  scanned under the  $k$ th applied force  $F_k$  as

$$v(x, F_k) = \beta(x)F_k + \delta_0(x) + \delta_1(x)I(k > 1) + \dots + \delta_{K-1}(x)I(k > K-1) + \varepsilon(x, F_k), \quad \dots\dots\dots (5.6)$$

where  $I(\cdot)$  is an indicator function and  $\varepsilon(x, F_k)$  is the error term. Note that the indicator function is to model the sequential nature of the experiment. The bias introduced during the  $k$ 'th experiment will only affect the subsequential experiments, but not the previous ones. Specifically, when the force  $F_k$  is applied to make the AFM tip in

contact with the nanobelt, the proposed approach models the deflection as  $v(x, F_k) = \beta(x)F_k + \delta_0(x) + \delta_1(x) + \dots + \delta_{k-1}(x) + \varepsilon(x, F_k)$ . In reality, there may or may not be a bias at stage  $k$ , i.e., some of the  $\delta_k$ 's may be zero. We therefore use a model selection technique to identify the significant  $\delta_k$ 's and include only them in the final model.

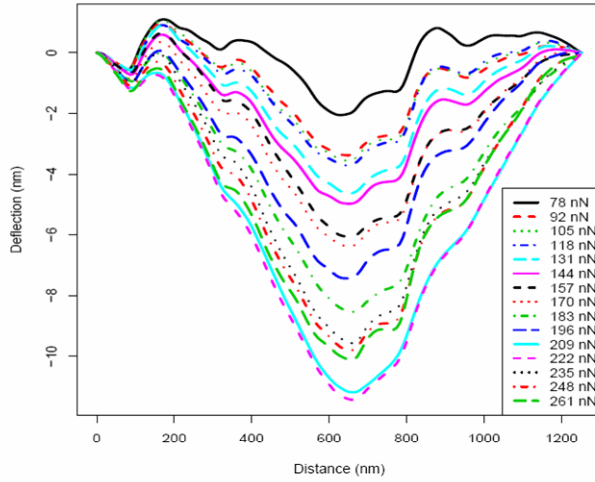


**Figure 59: Another set of deflection curves with large deviation.**

The model selection is actually a complicate process and requires a lot of work. The detailed of the calculation and discussion can be found in another work <sup>104</sup>. In simple words, there are some statistical criteria, such as smallest root mean square error (RMSE) or Bayesian information criterion (BIC), that can determine if a curve fitting is satisfying or not. Therefore, the computer can provide an objective way to distinguish the curves with larger deviation and even determine the amplitude of the deviation. The calculation indicates that the only three  $\delta_k$  ( $\delta_0$ ,  $\delta_{10}$ , and  $\delta_{12}$ ) are statistically significant. Thus, the chosen model is

$$v(x, F_k) = \beta(x)F_k + \delta_0(x) + \delta_{10}(x)I(k > 10) + \delta_{12}(x)I(k > 12) + \varepsilon(x, F_k) \dots\dots\dots (5.7)$$

Clearly, the new model can give us a better curve fitting results than the original FFBM, as shown in Figure 60. It solved the inconsistent pattern, while the physical model FFBM does not recognize this inconsistent pattern. In terms of RMSE or std(E), the value from the proposed method is about 50% for those from FFBM. The new estimate of E increases slightly from 94.34 to 101.52 GPa, closer toward the values from the other two nanobelts.

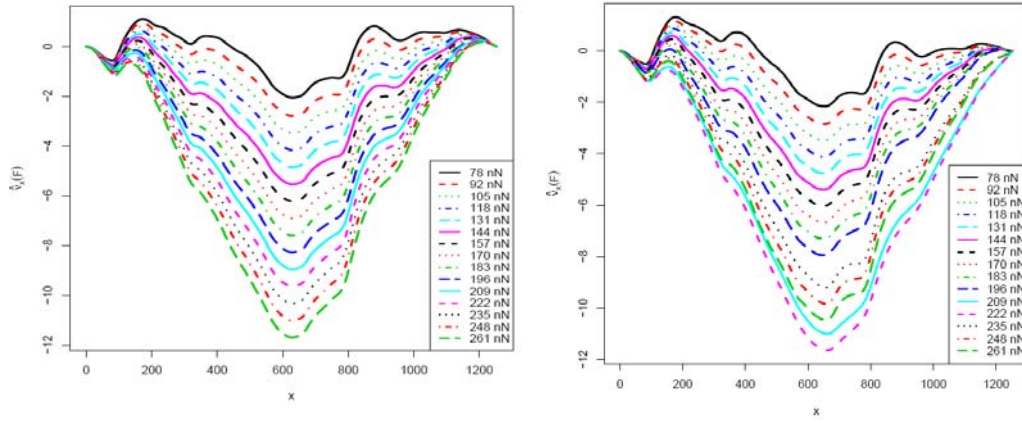


**Figure 60: (a) Curve fitting results with only FFBM. (b) Curve fitting results with the SPAR model, which introduces the statistical approach to capture the bias/noise.**

**Table 5: Comparison of estimators from the previous FFBM and the new SPAR.**

	RMSE	$1/\hat{E}$	Std(1/E)	$\hat{E}$	Std(E)
FFBM	0.86	1.06e-02	1.77e-04	94.34	1.58
SPAR	0.37	9.85e-03	7.63e-05	101.52	0.79

The SPAR method is proposed and its performance studied for a specific experiment on nanobelts. It can, however, have broad applications in the quantification of

the mechanical properties of 1-D nanomaterials. For example, San Paulo et al. studied the mechanical elasticity of single and double clamped nanowires<sup>81</sup>. The deflection of nanowires is measured by the controlled application of different normal forces with AFM. There is an initial variation in the growth of nanowires. Systematic bias can occur during the measurement under different applied forces. Therefore, SPAR can be used to get a better estimate of the elastic modulus. This new development demonstrates a statistical approach for quantifying the mechanical properties of 1-D nanomaterials by comprehensively analyzing the acquired data and filtering out systematic artifacts. The demonstrated methodology can be extended to other fields in nanotechnology.

# **CHAPTER 6**

## **ELECTRICAL PROPERTIES AND DEVICE APPLICATIONS OF BRIDGED NANOWIRES**

### **6.1 Enhanced Electrical Properties of ZnO Nanowires**

The full investigation of electrical properties of ZnO nanowires is the key for the future industrial applications. Due to the high surface to volume ratio in nanomaterials, the surface states are playing a very important role in sensor and device application. For example, if the sensing target is a chemical species, when the chemical species physically approaches or absorbs onto the nanowires, it alters the local electrical field around nanowires and in turn transport properties.

The issues related to the electrical transport of ZnO nanowires are challenging because of several reasons. Firstly, the concentration of electron carriers varies significantly in nanowires fabricated by different methods and different groups. The conducting electrons come from oxygen vacancies and zinc interstitial atoms. However, the concentration of these point defects is very sensitive to the fabrication process, and the control of oxygen vacancies and zinc interstitial atoms in ZnO nanowires has not been well understood and achieved yet. Secondly, n-type semiconductor ZnO forms either Ohmic or Schottky contacts with metals, depending on the difference of work function between semiconductor and metal. Ideally, the contact between ZnO and common metal



electrodes such as Au and Pt are Schottky type, which greatly impede the wide application of ZnO. Metals with low work function, such as Al and Ti, are able to form Ohmic contact with ZnO, but the problem is that these metals can easily oxidize in air, and thus, the process requires high vacuum environment, which significantly increases the complexity and the cost.

Figure 61(a) illustrates the nanowire bridging between two electrodes. Before Pt deposition, the I-V curve is quasi-linear and current is  $\sim 2.0 \times 10^{-10} \text{ A}$  at 1V, as shown in Figure 61 (b). We believe this configuration is a back-to-back Schottky barrier device. No matter whether the device is positive or negative biased, there is always a Schottky barrier at reverse bias and this limits the current of device but still remain somewhat symmetry. After the Pt deposition, the conductance of the device is greatly enhanced and I-V curve exhibits the perfect linearity, as illustrated in Figure 61(c). Experimental results indicate that the Pt deposited by FIB is able to destroy the Schottky barriers and tune the device to Ohmic region. The conductance is improved to  $8 \times 10^{-6} \text{ A}$  at 1V, which is about 4~5 orders of magnitude increase.

Although Pt deposition has been proven to be able to improve the Ohmic contact, the two problems related to Pt deposition severely limit the broad application of this approach. One problem is that Pt deposition is a slow and non-scalable process. Current application of Pt is still limited within the lab. Second problem is contamination recently discovered by researchers.<sup>105, 106</sup> The Pt deposition process is performed inside the FIB machine, and the procedure is explained as follows: After obtaining a good focus in ion image mode, define a specific area such as a circle or a square on the ion image, then heat the Pt source to working temperature and open the valve, and start deposition. Although

the deposition occurs mainly in the predefined area, as shown in SEM image, in fact, the deposition covers a much larger area and can not be easily observed by SEM. It has been observed that nanoparticles of Pt scatter outside the predefined area and sometime it can cause the current leaking and make the problem complicate. Besides, the Ga atoms from the ion gun are believed to contaminate the nanowire sample by doping effect. Furthermore, the Pt deposition process by FIB is a slow process, and probably won't have real application in microelectronic industry. Thus, if we can eliminate the Pt and still maintain the Ohmic contact, this will be of great practical importance.

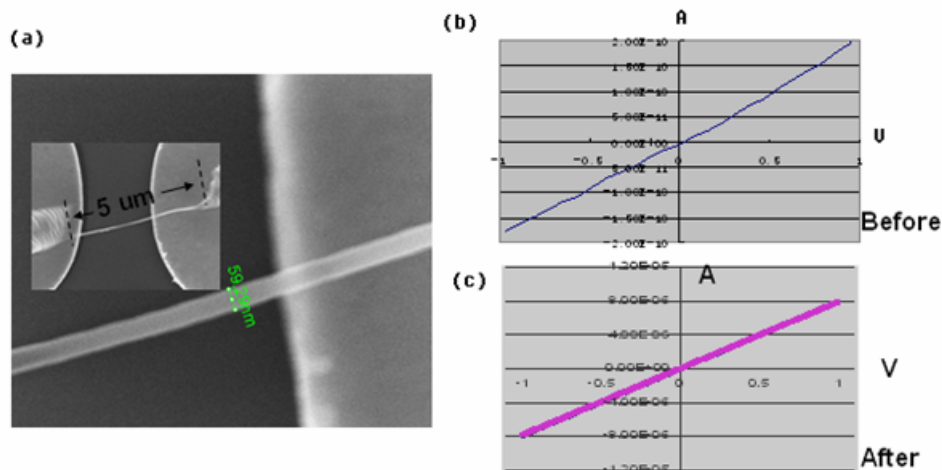


**Figure 61:** (a) The SEM image of the nanowire bridging between two electrodes; inset is the overall image of nanowire device after the Pt deposition by FIB. (b) The I-V curve obtained before the Pt deposition. (c) The I-V curve obtained after the Pt deposition.

One approach to solve the problem is to functionalize the electrodes. The fact that self-assembly molecules (SAM) have been able to tune the work function of the metal has been well known.<sup>107-109</sup> We specifically chosen three molecules, MBA, ODT, and MDA (see Figure 62). All these three molecules have quasi-linear shape: one end of the molecule has a functional group which can form good binding with Au electrodes; the other end of the molecule has a functional group which can form good binding with ZnO

nanowires. Therefore, these kinds of molecules can work as glue that can enhance the mechanical affinity and electrical contact.

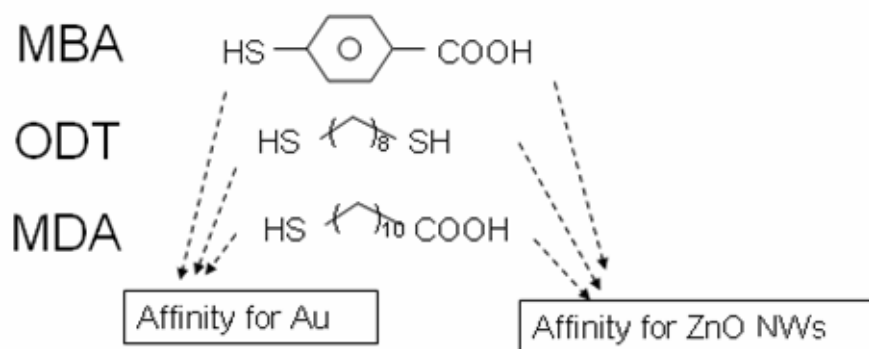


**Figure 62: Schematic diagrams of molecules: MBA, ODT and MDA.**

The procedure to coat these SAM is illustrated as follows (see Figure 63). The substrates with Au electrodes are mixed with 5mM MBA (or ODT, or MDA) in ethanol solution. The samples are kept in dark for 24 hours and then taken out and measured with contact angle to confirm the formation of the SAM because the SAM can significant change the hydrophobia/hydrophilic properties of the surface. Experiment shows that only the ODT and MDA can form prefer SAM layer on Au, but MBA can not probably because of the large phenyl. After the SAM coating, ZnO nanowire could be manipulated to bridge between two electrodes, and ethanol was applied on the substrate. With the ethanol evaporation, the nanowire will bind to the Au electrodes and SAM acts as glue to improve the mechanical and electrical properties of the contact.

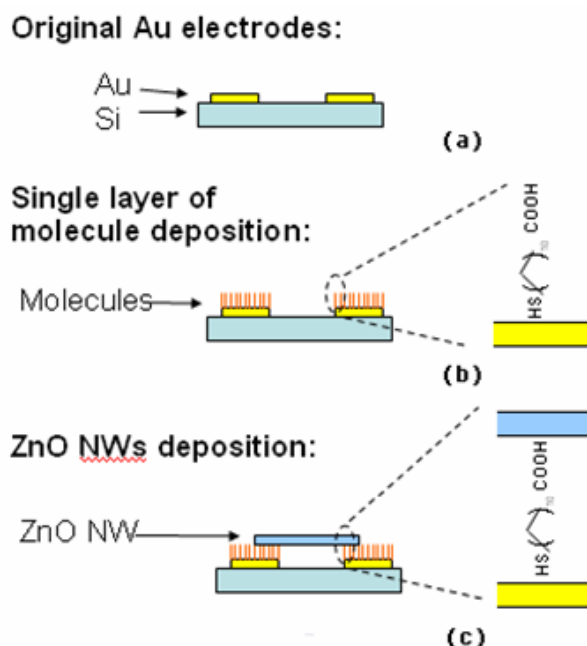
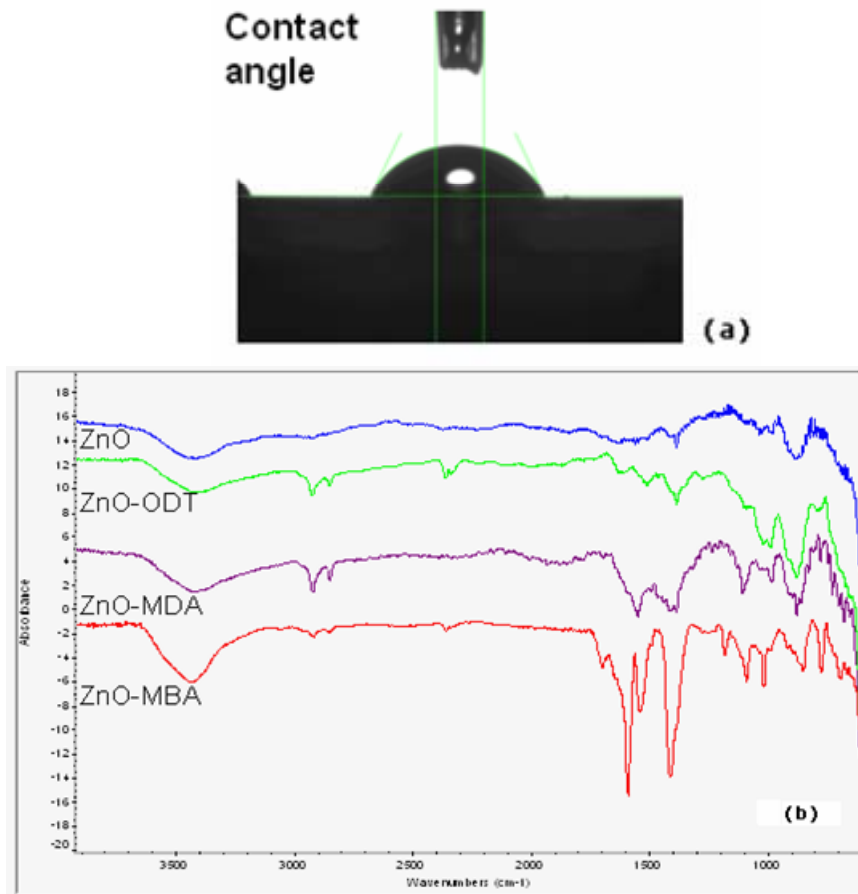


Figure 63: Procedure of SAM coating.

The confirmation of the binding between SAM and ZnO nanowires is not easy because of the small amount of nanowires and the non-transparency of the substrate. A simulated experiment has been performed. 0.03 g ZnO was mixed with 5mM MBA, (or ODT, or MDA) in ethanol, sonicated for 1 hour and purged with N<sub>2</sub>. The samples were kept in dark for 24 hours. After the samples were centrifuged, the supernatant were decanted and then the particles were re-dispersed in ethanol with sonication. The cycle repeated for 4 times. Then the residue was dried in vacuum before FT-IR measurements. FT-IR (Nicolet, Magna IR 560) were used to characterize the interaction between the molecules and ZnO particles. The samples were mixed with KBr and pressed to make a pellets. All of the spectra were collected at room temperature with 128 scans at a resolution of 4 cm<sup>-1</sup>.

The FT-IR results (see Figure 64b) indicate that the SAM has been successfully bonded to the ZnO. For all three molecules, peaks from HS- groups disappear, and a broad peak from HO- at  $\sim 3400\text{cm}^{-1}$  and two small peaks from  $-\text{CH}_2-$  at  $2800\sim 3000\text{ cm}^{-1}$  remain. This indicates that the HS- groups will also bind to ZnO, but in the serial coating, HS- groups should prefer to bind to Au, thus leave no chance to bind ZnO later. Peaks from  $-\text{COO}-$  at  $\sim 1550$  and  $1400\text{ cm}^{-1}$  are observed and proved of the binding of  $-\text{COOH}$  to ZnO.



**Figure 64: (a) Contact angle measurement of the SAM coated Au surface. (b) FT-IR results of the simulated experiment, confirming the bonding between SAM and ZnO nanowires.**

The conductance measurement results are illustrated in Figure 65. The conductance of control group without SAM layer mainly falls between  $1\text{E-}11\text{A}$  and  $1\text{E-}10\text{A}$ . The conductance of MBA coated samples slightly shifts toward  $1\text{E-}10\text{A}$  and  $1\text{E-}9\text{A}$  level. As stated before, the MBA monolayer is found not well organized on Au and aggregation of MBA molecules probably inhibit the further electrical transport. MDA and ODT coated samples show a significant increase in conductance, which is about 2 orders of magnitude.

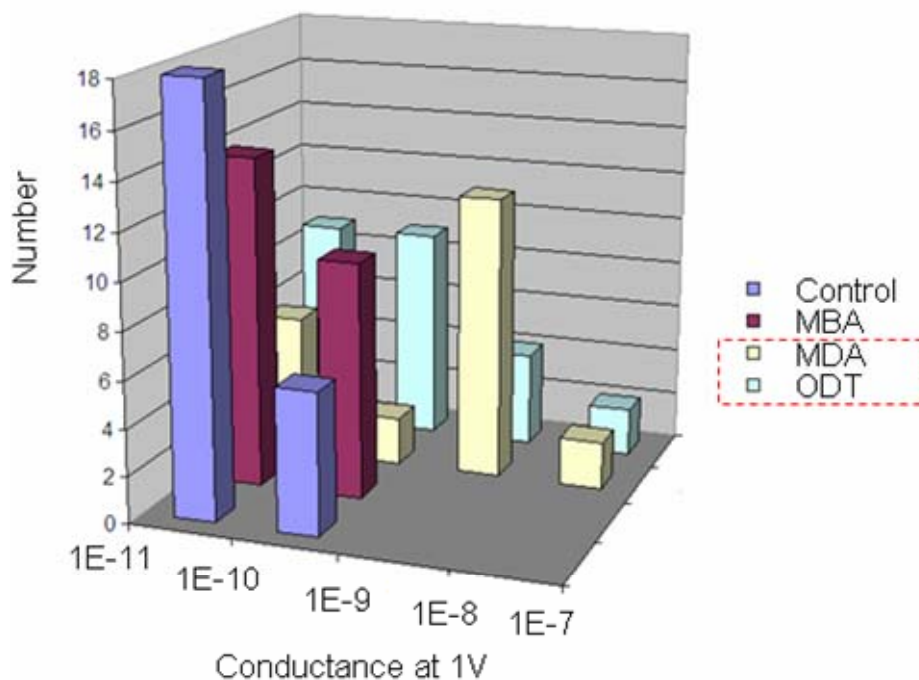


**Figure 65: Histogram of the conductance of the devices, which shows the MDA and ODT treated samples have a better electrical conductivity than the control samples.**

This increase in conductance is encouraging because the observed phenomenon directly prove that the SAM is indeed able to enhance the contact area and tune the work function of the metal and enhance the conductivity to some extent. But the conductance

measurement indicates that the enhancement is not enough to boost the current to Ohmic region. However, Schottky type nanowire devices sometimes could have better performance than Ohmic type devices.

## 6.2 UV Sensors

The Ohmic type ZnO nanowires based UV sensors have been fabricated by both dielectrophoresis and direct manipulation. Usually, the contacts of the devices by these two methods are not very reliable, because of the poor physical contact as well as the local heating effect<sup>29</sup>. Many researchers use focus ion beam (FIB) to deposit Pt on both ends to improve the contact. I-V measurement indicates that the electrical device displays perfect linear Ohmic behavior (see Figure 66).

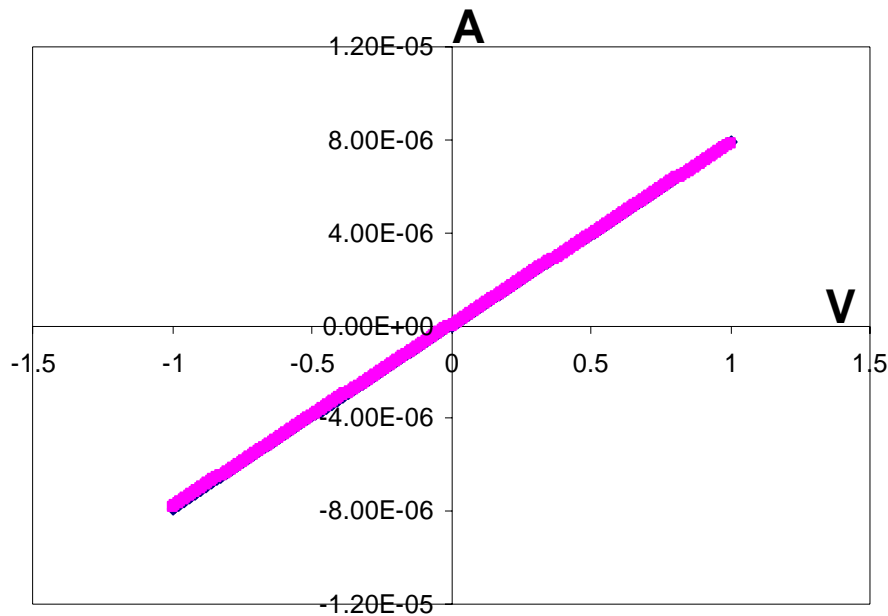


**Figure 66: Perfect linear Ohmic behavior of the nanowire with Pt deposition on both ends.**

This single nanowire is  $\sim 5$   $\mu\text{m}$  in length and  $\sim 60$  nm in diameter. Therefore, the calculated resistivity is  $\sim 7 \times 10^{-2}$   $\Omega\cdot\text{cm}$ , 3 orders of magnitude smaller than the common bulk materials, because of a large amount of point defects introduced during the nanowire synthesis.

The corresponding UV sensing I-V curves are displayed in Figure 67, which shows that the UV conductance is  $\sim 33\%$  increase and decay time is long up to thousands of seconds.

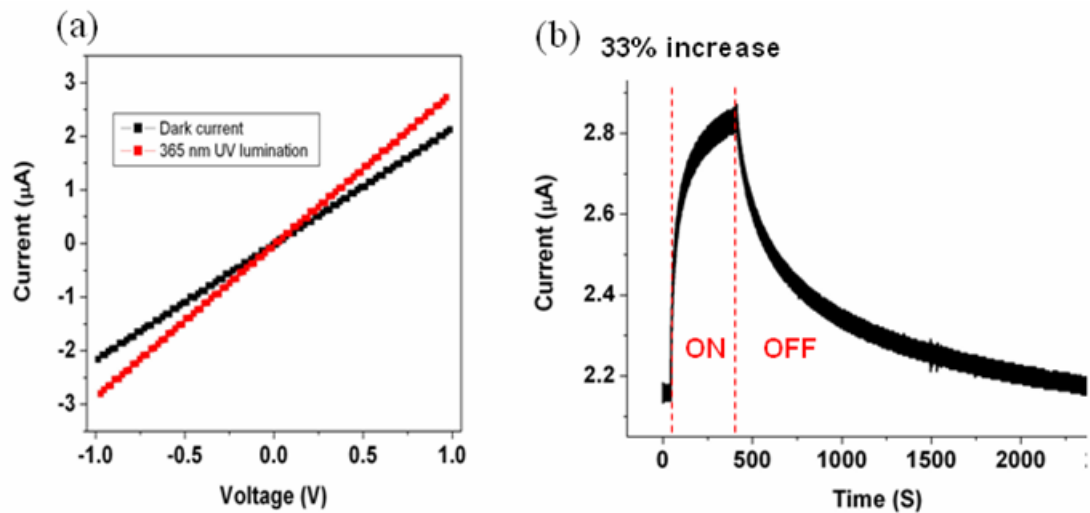


**Figure 67:** UV sensing properties of the Ohmic type device.

In order to eliminate the Pt deposition, which brings extra procedures and possible contamination, functionalization of electrodes is a new perspective and worth of our attention. The goal of functionalization is to coat a layer of self assembly molecules on electrodes to function as glues. Three different species of molecules have been chosen: MBA, ODT, and MDA. All three species of molecules have linear shapes and two functional groups at both ends: one binds to Au electrodes, and the other binds to ZnO



nanowires (see Figure 62). The binding will improve the physical and electrical contact of the nanowire devices.

The original I-V curves of these devices with SAM layer are much smaller (2-4 orders of magnitude) than those of devices treated with Pt deposition. The back-to-back two Schottky barriers configuration is believed to exist. Thus the conductivity here is much smaller than the usual Ohmic type electrical device.

UV measurement shows that the UV sensitivity of Schottky type devices shows a significant increase, as illustrated in Figure 68. Conductance of these devices increases up to 2 orders of magnitude, much better than Ohmic type devices (a few times increase). The decay time also significantly decreases. It is well known that the dipoles in SAM can alter the work function of the metal, but in our cases, they are not enough to lower the work function smaller than ZnO, thus they improve the contacts while retain the Schottky behavior. The Schottky barrier at reverse bias consumes the majority part of the applied voltage and exhibits high resistance. The UV lights generate electron-hole pairs not only at the nanowire body, but also at the contact region. The sudden appearance of extra charge carriers can largely improve the local conductance at Schottky contact, leading to a significant increase in the conductivity of the entire device. When the UV lights are turned off, this generation process ceases and contributes to the relatively fast decay.

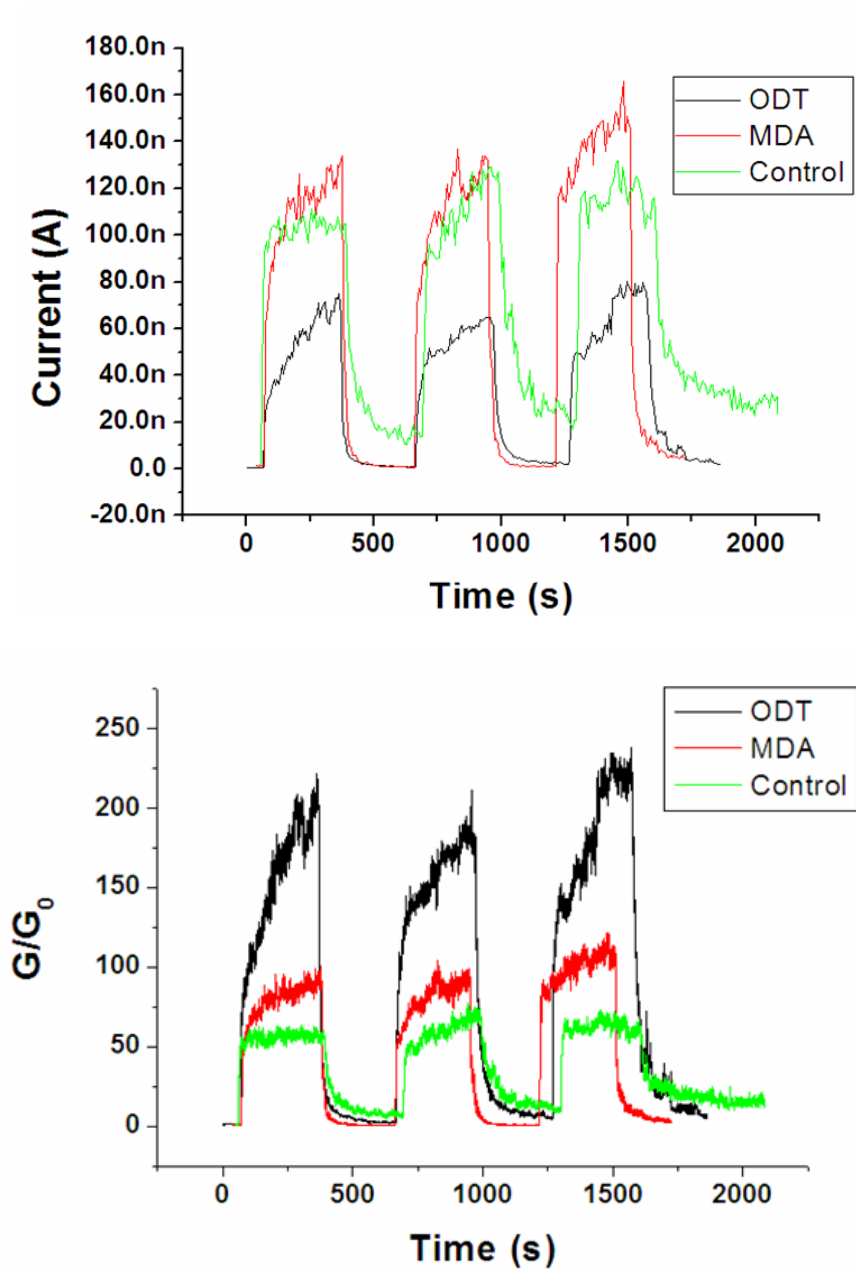


Figure 68: (a) Original and (b) normalized UV sensing properties of the Schottky back-to-back ZnO nanowire devices.

### 6.3 Strain Sensors

Recent research in the field of micro- and nano-electromechanical system (MEMS) and NEMS is rapidly growing with considerable potential for ultra fast, high-sensitivity

and low-power consumption devices. As for nano- and micro-scale strain/stress and pressure measurements, various sensors have been fabricated based on nanowires and carbon nanotubes (CNTs).<sup>110-114</sup> Commonly, these devices utilize the piezoresistance property of the material, i.e., under small strain, the conductance of the material changes with strain following a linear relationship. CNT is the most intensively studied material in this area, and sensor device based on CNTs with gauge factor up to 850 have been achieved.<sup>113</sup> However, studies have shown that the piezoresistance property depends on the electronic structure of CNTs, which can be metallic or semiconducting depending on their structures.<sup>113</sup>

Here, we present the fabrication and application of an alternative design of a fully packaged strain sensor device based on a single ZnO piezoelectric fine wire (PFW) (nanowire, microwire). The strain sensor was fabricated by bonding a ZnO PFW laterally on a polystyrene (PS) substrate. The I-V behavior of the device was modulated by strain due to the change in Schottky-barrier height (SBH). The combined effects from strain induced band structure change and piezoelectricity result in the change of SBH. The working principle of the new type strain sensor has been presented in comparison to theoretical model.

The schematic of the strain sensor device is shown in Figure 69a. Ultra-long ZnO PFWs were synthesized by a high temperature physical vapor deposition process, and they typically have diameters of 2-6  $\mu\text{m}$  and lengths of several hundred micrometers to several millimeters. We choose large size wires for easy of manipulation under optical microscope. The same principle and methodology applies to nanowires. The typical PS substrate has a length of  $\sim 3$  cm, width of  $\sim 5$  mm and thickness of 1 mm. The substrate

was sequence washed with deionized water and ethanol under sonication. After drying with flowing nitrogen gas and placing in a furnace at 80°C for 30 minutes, the PS substrate was ready to be used as the substrate. ZnO PFW was placed on the PS substrate by using a probe station under optical microscopy. Silver paste was applied at both ends of the ZnO PFW to fix its two ends tightly on the substrate, silver paste was also used as source and drain electrodes. A thin layer of polydimethylsiloxane (PDMS) was used to package the device. The thickness of the PDMS layer is much thinner than the thickness of the PS substrate. The PDMS thin layer not only enhances the adherence of the silver paste to the PS substrate, but also prevents the ZnO wire from contamination or corrosion when it was exposed to atmosphere. Then the entire device was annealing at 80°C for 12 hours. Finally, a flexible, optically transparent, and well packaged strain sensor device was fabricated. Figure 69b shows an optical image of the strain sensor device, indicating a smooth ZnO wire was placed on the substrate with two ends fixed.

The characterization of the I-V behavior of the sensor device with strain was carried out in atmosphere at room temperature, and the measuring system is schematically shown in Figure 69c. One end of the device was affixed on a sample holder that was fixed tightly on an optical air table, with another end free to be bent. An x-y-z mechanical stage with movement resolution of 1  $\mu\text{m}$  was used to bend the free end of the sensor device to produce a compressive or tensile strain. Meanwhile continuously triangle sweeping voltage was applied through the ZnO wire to measuring its I-V characteristics during deformation. To study the stability and response of the sensor devices, a resonator with controlled frequency and amplitude was used to periodically bend the sensor device. At the same time, a fixed bias voltage was applied between the source and drain.

Since the thin PDMS layer has a much smaller young's modulus ( $E=360\text{-}870\text{ KPa}$ ) than that of PS substrate ( $E=3\text{-}3.5\text{ GPa}$ ), and the silver paste electrodes have a much smaller area and thickness in comparison to those of the PS substrate, the PDMS layer and silver paste electrodes, which are bond on the outer surface of the PS substrate, do not alter the mechanical properties of the PS film at any significant level. Therefore, the strain in the PFW is either purely tensile or compressive depending on the bending direction of the PS substrate. The strain in the PFW is approximately equal to the strain of the site  $z$  where it was placed at on the outer surface of the PS substrate. With consideration the extremely small diameter of the PFW in comparison to the thickness of the PS substrate, the axial strain  $\epsilon_{zz}$  along the length of the PFW is approximately 20-22

$$\epsilon_{zz} = 3 \frac{a}{l} \frac{D_{\max}}{l} \left(1 - \frac{z}{l}\right) \dots\dots\dots(6.1)$$

where  $z$  is the vertical distance measured from the fixed end of the PS substrate to the middle of the PFW;  $a$  is the half thickness of the PS substrate;  $l$  is the length of PS film from the fixed end to the free end; and  $D_{\max}$  is the maximum deformation of the free end of the PS substrate, which has a negative or positive sign depending the PFW is under compressive or tensile strain, respectively. Equation 7.1 indicates that the strain  $\epsilon_{zz}$  has a linear relationship with the maximum deformation  $D_{\max}$ . In practice, since the length of the substrate is much larger than the length of the PFW ( $l \gg L$ ), the strain in the PFW is uniform to an excellent approximation.

Before the electromechanical measurements, we have first measured the original I-V characteristic of the sensor device. We found various I-V characteristics for over 250 devices. The nonlinear I-V characteristics are commonly observed in measuring

semiconductor devices.<sup>115, 116</sup> Generally the nonlinearity is caused by the Schottky barriers formed between the semiconductor and metal electrodes in the semiconductor device, and the shape of the I-V curve depends on the heights of the Schottky barriers formed at the source and drain due to different interface properties.<sup>116</sup> In this study, we only focused on the devices that have Schottky contacts at the two ends of the PFW, but with distinctly different barrier heights (see Figure 69d). The I-V curve shape is quite asymmetric. Typical I-V characteristics under various strains (Device #1) are shown in Figure 70a. The I-V curves shift upward with tension strain and downward with compressive strain. The I-V curve fully recovered when the strain was relieved.

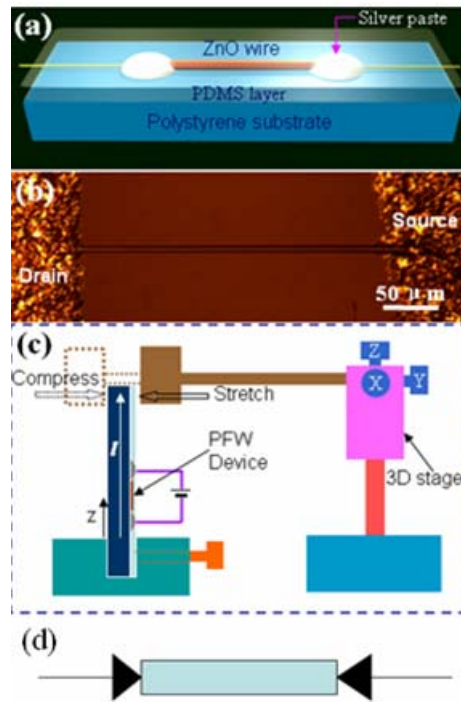


**Figure 69: (a) Schematic of a single ZnO PFW based strain sensor device. (b) Optical image of a strain sensor. (c) Schematic of the measurement system to characterize the performance of the strain sensor. (d) Proposed electric circuit diagram for the strain sensor.**

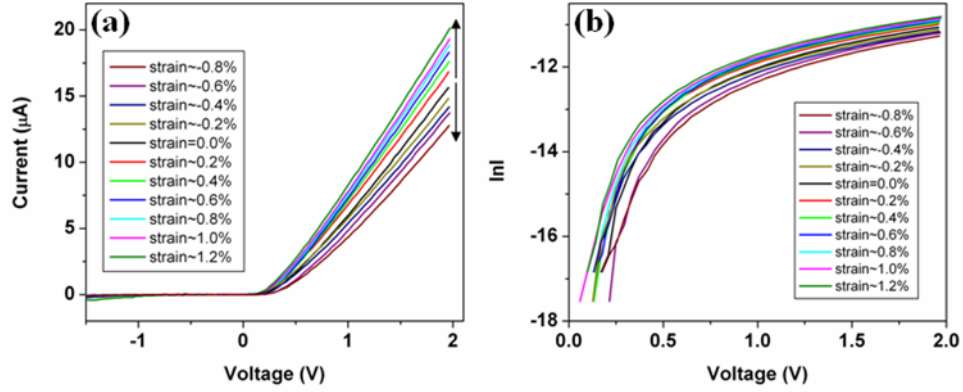


**Figure 70: (a) Typical I-V characteristics of the strain sensor at different strain. (b) Logarithm plot of the current under positive bias by using the data in (a)**

The I-V curve shown in Figure 70a clearly demonstrates that there were Schottky barriers present at the contacts but with distinctly different barrier heights. The presence of a Schottky barrier at the metal/semiconductor interface plays a crucial role in determining the electrical transport property of the metal-semiconductor-metal (M-S-M) structure.<sup>117</sup> By simply looking at the I-V curve one is unable to identify the nature of the barriers either reversely biased or forward biased. It is important to quantitatively simulate the shape of the I-V curve in order to determine the nature of the electric transport across the M-S-M structure.<sup>115, 116</sup> After carefully studying the shape of the I-V curve, our device is considered as a single ZnO wire sandwiched between two opposite Schottky barriers, as shown in Figure 69d. We assume that the barrier height at the drain side  $\phi_d$  (eV) is significantly higher than that at the source side as in Figure 71a. At a fixed bias voltage  $V$ , the voltage drop occurs mainly at the reversely biased Schottky barrier according to the measurement by in-situ scanning surface potential microscopy.<sup>118</sup> In our case, when a relatively large positive voltage  $V$  is applied across the drain and source with the drain positive, the voltage drop occurs mainly at the reversely biased Schottky

barrier  $\phi_s$  (eV) at the source side, and it is denoted by  $V_s$ . Here we assume  $V_s \approx V$ . With consideration that our measurements were made at room temperature and the ZnO PFW had a low doping, the dominant transport property at the barrier is thermionic emission and diffusion, while the contribution made by tunneling can be ignored. Thus, as inspired by the shape of the  $\ln I - V$  curve in Figure 70b, and according to the classic thermionic emission-diffusion theory (for  $V \gg 3kT/q \sim 77$  mV) for a reversal bias voltage  $V$  and at temperature  $T$ , the current through the reversely biased Schottky barrier  $\phi_s$  is given by<sup>117</sup>

$$I = SA^{**}T^2 \exp\left(-\frac{\phi_s}{kT}\right) \exp\left(\frac{\sqrt[4]{q^7 N_D (V + V_{bi} - kT/q) / (8\pi^2 \epsilon_s^3)}}{kT}\right) \dots\dots\dots(6.2)$$

where  $S$  is the area of the source Schottky barrier,  $A^{**}$  is the effective Richardson constant,  $q$  is the electron charge,  $k$  is Boltzman constant,  $N_D$  is the donor impurity density,  $V_{bi}$  is the build in potential at the barrier, and  $\epsilon_s$  is the permittivity of ZnO. The  $\ln I - V$  curve shown in Figure 71b qualitative indicates that variation of  $\ln I$  can be described by  $V^{1/4}$  for reversely biased Schottky barrier instead of  $\ln I \sim V$  as for forward biased Schottky barrier. Therefore, Equation 7.2 can be used to precisely fit the experimentally observed  $\ln I - V$  curve, from which the corresponding parameters can be derived. This not only indicates that the thermionic emission – diffusion model is the dominant process in our device, but also can be applied to derive the SBH as described in follows.

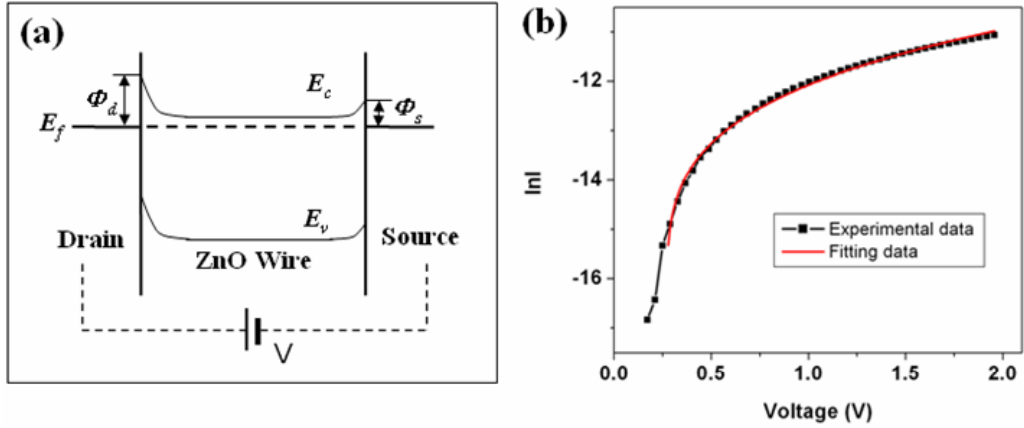
By assuming that  $S$ ,  $A^{**}$ ,  $T$ ,  $N_D$  are independent of strain for small deformation,  $\phi_s$  can, in principle, be derived from the logarithm of the current ( $\ln I$ )- $V$  plot, which is shown in Figure 71b. Subsequently, the change of SBH can be determine by

$$\ln[I(\epsilon_{zz}) / I(0)] = -\Delta\phi_s / kT \dots\dots\dots(6.3)$$



where  $I(\varepsilon_{zz})$  and  $I(0)$  are the current measured through the PFW at a fixed bias with and without being strained, respectively. The results are plotted in Figure 71c for two biases of 1.5 and 2 V, indicating that the change of SBH  $\Delta\phi_s$  has an approximately linear relationship with strain, which is consistent with the previous reports.<sup>119-122</sup> We also notice that the  $\Delta\phi_s$  is not very sensitive to the choice of bias voltage  $V$ .

In the calculation presented above, we assumed that the applied voltage was totally consumed at the reversely biased Schottky barrier formed at the source electrode. In reality,  $V_s < V$ , thus the calculated  $\Delta\phi_s$  value may be slightly affected by the choice of  $V$ , but the linear dependence of  $\Delta\phi_s$  on strain will not be affected much. Figure 71d shows the change of  $\ln I$  at fixed bias of  $V = 1.5$  V and 2.0 V as a function of strain (Device #1). The change of  $\ln I$  varies approximately linear with the applied strain.



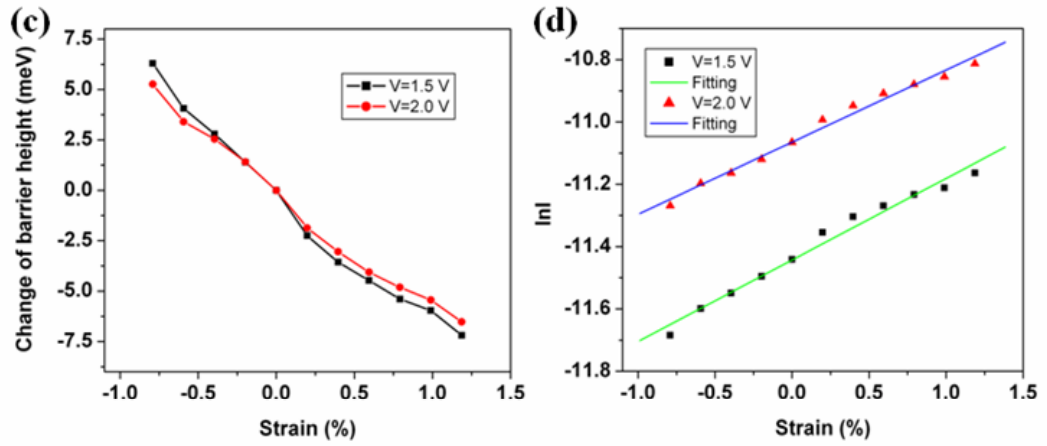


**Figure 71:** Energy band diagram illustrates the asymmetric Schottky barrier heights at the source and the drain contacts of a PFW, where the offset by the applied drain-source voltage  $V$  was not included for easy discussion. (b) Fitting the  $\ln I$ - $V$  data using the thermionic emission – diffusion theory at a given strain for a reversely biased Schottky barrier. The black dotted are experimental data points from Figure 70(a) for stain=0, and the red line is the theoretical fit. (c) The derived change in SBH based on the thermionic emission – diffusion model, as a function of strain at a drain-source bias of  $V=1.5\text{V}$  and  $2.0\text{V}$ , respectively. (d) Logarithm plot of the current (in unit of A) at fixed bias of  $V=1.5\text{V}$  and  $2.0\text{V}$  as a function of strain.

In summary, a new type fully packaged strain sensor device based on a single ZnO PFW has been demonstrated. The strain sensor was fabricated by bonding a ZnO PFW laterally on a flexible PS substrate and packaged by a PDMS thin film. A simplified model from thermionic emission-diffusion model has been deduced to explain the current response from the Schottky barrier height change. The strain sensor developed here based on a flexible substrate has application in strain and stress measurements in cell biology, biomedical sciences, MEMS devices, structure monitoring and even earthquake monitoring.

# **CHAPTER 7**

## **CONCLUSION**

Nanoscience and nanotechnology are still at their early stages as a field. Extensive works have been performed and people have understood better about the phenomena occurring at nanoscale. The current research focus has been moved from the materials synthesis to their promising properties. Without superior performance and novel application, the nanoscience and nanotechnology will go nowhere. Fortunately, series of breakthroughs closely related to quantum dots, carbon nanotubes, ZnO nanowires, etc, in broad areas such as medical imaging, drug transport, electronic device, and energy storage have proven the bright future in nanoscience and nanotechnology.

This dissertation is based on the previous research work on synthesis of ZnO nanowires and nanobelts. PVD method has been further investigated to synthesize nanomaterials. PVD method can produce a lot of different morphology, among which is a newly discovered superlattice-structured nanohelix. The nanohelix is made of two types of alternating and periodically distributed long crystal strips, resulting in the rigid rotation of the nanobelt. The other widely studied nanomaterial is vertically aligned ZnO nanowire array, which was epitaxially grown on GaN and SiC substrates. Manipulation of the nanomaterials and integration of them into electronic devices remain challenging issues in the bottom up nanotechnology. To answer these challenges, several manipulation methods, such as EBL, dielectrophoresis, and direct in situ manipulation, have been developed, so that the mechanical and electrical properties of single nanostructure can be characterized. The nanohelix was manipulated and showed super-

elasticity. The axial or transversal effective spring constants have been calculated or measured, suggesting possible uses in electromechanically coupled sensors and transducers. Bridged nanowire configuration is the most important configuration that spurs numerous research interests. The AFM scanning the suspended part with different loads provides a deep insight for mechanics in bridged nanowires. The boundary conditions for ZnO nanowires have been determined to be free instead of clamped boundary conditions; therefore the free-free beam model has been used to calculate the elastic modulus. For electrical properties, direct contact of bridged ZnO nanowire over Au electrodes displays a back-to-back Schottky behavior. SAM can tune the work function of metal electrode in small extend and enhance the contact area, thus altering the barrier height of the contact and increase the conductance. The performance of back-to-back Schottky type UV sensors had been proven much better than that of the Ohmic type UV sensor. Investigations of bridged ZnO nanowire based and strain sensors have also show promising practical applications of nanomaterials.

The future work of continuous research should be focused on novel device fabrication and application. With more efforts on the optimization and improvement, ZnO nanowire based devices, such as nanogenerators, solar cells, and strain sensors, should significantly enhance the understanding of the physical phenomenon at nanoscale and potentially change the future life style.

## REFERENCES

- <sup>1</sup> H. W. Kroto, J. R. Heath, S. C. O'Brien, et al., *Nature* **318**, 162 (1985).
- <sup>2</sup> S. Iijima, *Nature* **354**, 56 (1991).
- <sup>3</sup> A. P. Alivisatos, *Science* **271**, 933 (1996).
- <sup>4</sup> A. P. Alivisatos, A. L. Harris, N. J. Levinos, et al., *Journal of Chemical Physics* **89**, 4001 (1988).
- <sup>5</sup> R. C. Ashoori, *Nature* **379**, 413 (1996).
- <sup>6</sup> Y. Cui and C. M. Lieber, *Science* **291**, 851 (2001).
- <sup>7</sup> W. C. W. Chan and S. M. Nie, *Science* **281**, 2016 (1998).
- <sup>8</sup> Z. L. Wang and J. H. Song, *Science* **312**, 242 (2006).
- <sup>9</sup> S. Frank, P. Poncharal, Z. L. Wang, et al., *Science* **280**, 1744 (1998).
- <sup>10</sup> T. W. Odom, J. L. Huang, P. Kim, et al., *Nature* **391**, 62 (1998).
- <sup>11</sup> P. Poncharal, Z. L. Wang, D. Ugarte, et al., *Science* **283**, 1513 (1999).
- <sup>12</sup> M. F. Yu, O. Lourie, M. J. Dyer, et al., *Science* **287**, 637 (2000).
- <sup>13</sup> J. P. Salvetat, G. A. D. Briggs, J. M. Bonard, et al., *Physical Review Letters* **82**, 944 (1999).
- <sup>14</sup> X. D. Wang, J. H. Song, J. Liu, et al., *Science* **316**, 102 (2007).
- <sup>15</sup> W. J. Mai, P. X. Gao, C. S. Lao, et al., *Chemical Physics Letters* **460**, 253 (2008).
- <sup>16</sup> Z. W. Pan, Z. R. Dai, and Z. L. Wang, *Science* **291**, 1947 (2001).
- <sup>17</sup> P. X. Gao and Z. L. Wang, *Applied Physics Letters* **84**, 2883 (2004).
- <sup>18</sup> C. S. Lao, P. M. Gao, R. Sen Yang, et al., *Chemical Physics Letters* **417**, 358 (2006).

- <sup>19</sup> W. L. Hughes and Z. L. Wang, Journal of the American Chemical Society **126**, 6703 (2004).
- <sup>20</sup> X. Y. Kong and Z. L. Wang, Nano Letters **3**, 1625 (2003).
- <sup>21</sup> P. M. Gao, Y. Ding, W. J. Mai, et al., Science **309**, 1700 (2005).
- <sup>22</sup> P. X. Gao, W. J. Mai, and Z. L. Wang, Nano Letters **6**, 2536 (2006).
- <sup>23</sup> X. Y. Kong, Y. Ding, R. Yang, et al., Science **303**, 1348 (2004).
- <sup>24</sup> Q. X. Zhao, M. Willander, R. E. Morjan, et al., Applied Physics Letters **83**, 165 (2003).
- <sup>25</sup> W. I. Park, J. S. Kim, G. C. Yi, et al., Applied Physics Letters **85**, 5052 (2004).
- <sup>26</sup> F. Krumeich, H. J. Muhr, M. Niederberger, et al., Journal of the American Chemical Society **121**, 8324 (1999).
- <sup>27</sup> X. D. Bai, P. X. Gao, Z. L. Wang, et al., Applied Physics Letters **82**, 4806 (2003).
- <sup>28</sup> S. X. Mao, M. H. Zhao, and Z. L. Wang, Applied Physics Letters **83**, 993 (2003).
- <sup>29</sup> C. S. Lao, J. Liu, P. X. Gao, et al., Nano Letters **6**, 263 (2006).
- <sup>30</sup> R. F. Pierret, *Semiconductor Device Fundamentals* (Addison-Wesley, 1996).
- <sup>31</sup> Q. Kuang, C. S. Lao, Z. L. Wang, et al., Journal of the American Chemical Society **129**, 6070 (2007).
- <sup>32</sup> L. Liao, H. B. Lu, J. C. Li, et al., Applied Physics Letters **91** (2007).
- <sup>33</sup> E. K. Kim, H. Y. Lee, S. E. Moon, et al., Journal of Nanoscience and Nanotechnology **8**, 4698 (2008).
- <sup>34</sup> T. J. Hsueh, S. J. Chang, C. L. Hsu, et al., Applied Physics Letters **91** (2007).
- <sup>35</sup> X. D. Wang, C. J. Summers, and Z. L. Wang, Nano Letters **4**, 423 (2004).
- <sup>36</sup> C. Soci, A. Zhang, B. Xiang, et al., Nano Letters **7**, 1003 (2007).
- <sup>37</sup> Y. W. Heo, B. S. Kang, L. C. Tien, et al., Applied Physics a-Materials Science & Processing **80**, 497 (2005).
- <sup>38</sup> Q. H. Li, Q. Wan, Y. X. Liang, et al., Applied Physics Letters **84**, 4556 (2004).

- 39 M. S. Arnold, P. Avouris, Z. W. Pan, et al., *Journal of Physical Chemistry B* **107**, 659 (2003).
- 40 E. Comini, G. Faglia, G. Sberveglieri, et al., *Applied Physics Letters* **81**, 1869 (2002).
- 41 Y. Cui, Q. Q. Wei, H. K. Park, et al., *Science* **293**, 1289 (2001).
- 42 M. H. Zhao, Z. L. Wang, and S. X. Mao, *Nano Letters* **4**, 587 (2004).
- 43 Y. Qin, X. D. Wang, and Z. L. Wang, *Nature* **451**, 809 (2008).
- 44 X. D. Wang, J. Zhou, J. H. Song, et al., *Nano Letters* **6**, 2768 (2006).
- 45 S. M. Arnold and S. E. Koonce, *Journal of Applied Physics* **27**, 964 (1956).
- 46 Z. R. Dai, Z. W. Pan, and Z. L. Wang, *Advanced Functional Materials* **13**, 9 (2003).
- 47 R. S. Wagner and W. C. Ellis, *Jom-Journal of Metals* **16**, 761 (1964).
- 48 R. S. Wagner and W. C. Ellis, *Applied Physics Letters* **4**, 89 (1964).
- 49 A. M. Morales and C. M. Lieber, *Science* **279**, 208 (1998).
- 50 M. H. Huang, S. Mao, H. Feick, et al., *Science* **292**, 1897 (2001).
- 51 X. D. Wang, J. H. Song, C. J. Summers, et al., *Journal of Physical Chemistry B* **110**, 7720 (2006).
- 52 M. Kirkham, X. D. Wang, Z. L. Wang, et al., *Nanotechnology* **18** (2007).
- 53 H. S. Liu, K. Ishida, Z. P. Jin, et al., *Intermetallics* **11**, 987 (2003).
- 54 Y. W. Wang, V. Schmidt, S. Senz, et al., *Nature Nanotechnology* **1**, 186 (2006).
- 55 K. A. Dick, K. Deppert, T. Martensson, et al., *Nano Letters* **5**, 761 (2005).
- 56 A. I. Persson, M. W. Larsson, S. Stenstrom, et al., *Nature Materials* **3**, 677 (2004).
- 57 X. D. Wang, J. H. Song, P. Li, et al., *Journal of the American Chemical Society* **127**, 7920 (2005).
- 58 J. H. Song, X. D. Wang, E. Riedo, et al., *Journal of Physical Chemistry B* **109**, 9869 (2005).

- 59 G. Ziegler, P. Lanig, D. Theis, et al., IEEE Transactions on Electron Devices **30**, 277 (1983).
- 60 I. Ichimura, F. Maeda, K. Osato, et al., Japanese Journal of Applied Physics Part 1-Regular Papers Short Notes & Review Papers **39**, 937 (2000).
- 61 S. Xu, Y. Wei, M. Kirkham, et al., Journal of the American Chemical Society **130**, 14958 (2008).
- 62 Y. Huang, X. F. Duan, Q. Q. Wei, et al., Science **291**, 630 (2001).
- 63 C. S. Lao, in *Materials Science and Engineering* (Georgia Institute of Technology, Atlanta, 2007).
- 64 S. Y. Lee, J. H. Hyung, and S. K. Lee, Electronics Letters **44**, 695 (2008).
- 65 S. Y. Lee, T. H. Kim, D. I. Suh, et al., Physica E-Low-Dimensional Systems & Nanostructures **36**, 194 (2007).
- 66 G. Stollwerck, S. Reber, and C. Hassler, Advanced Materials **13**, 1820 (2001).
- 67 T. M. Mayer, J. W. Elam, S. M. George, et al., Applied Physics Letters **82**, 2883 (2003).
- 68 Y. C. Lin, K. C. Lu, W. W. Wu, et al., Nano Letters **8**, 913 (2008).
- 69 H. T. Chen, S. I. Hsieh, C. J. Lin, et al., IEEE Electron Device Letters **28**, 499 (2007).
- 70 C. M. Lieber and Z. L. Wang, Mrs Bulletin **32**, 99 (2007).
- 71 Z. H. Chen, J. Appenzeller, Y. M. Lin, et al., Science **311**, 1735 (2006).
- 72 K. L. Ekinici, X. M. H. Huang, and M. L. Roukes, Applied Physics Letters **84**, 4469 (2004).
- 73 X. X. Li, T. Ono, Y. L. Wang, et al., Applied Physics Letters **83**, 3081 (2003).
- 74 S. Hoffmann, I. Utke, B. Moser, et al., Nano Letters **6**, 622 (2006).
- 75 A. San Paulo, N. Arellano, J. A. Plaza, et al., Nano Letters **7**, 1100 (2007).
- 76 A. Heidelberg, L. T. Ngo, B. Wu, et al., Nano Letters **6**, 1101 (2006).
- 77 C. T. Huang, C. L. Hsin, K. W. Huang, et al., Applied Physics Letters **91** (2007).



- 78 B. E. Schuster, Q. Wei, M. H. Ervin, et al., *Scripta Materialia* **57**, 517 (2007).
- 79 L. D. Landau and E. M. Lifshitz, *Course of Theoretical Physics* (Pergamon, Oxford, 1959).
- 80 S. P. Timoshenko and J. M. Gere, *Theory of Elastic Stability* (McGraw-Hill, New York, 1961).
- 81 A. San Paulo, J. Bokor, R. T. Howe, et al., *Applied Physics Letters* **87** (2005).
- 82 J. H. Song, X. D. Wang, E. Riedo, et al., *Nano Letters* **5**, 1954 (2005).
- 83 Y. Dai, Y. Zhang, Q. K. Li, et al., *Chemical Physics Letters* **358**, 83 (2002).
- 84 D. J. Milliron, S. M. Hughes, Y. Cui, et al., *Nature* **430**, 190 (2004).
- 85 Y. W. Jun, Y. Y. Jung, and J. Cheon, *Journal of the American Chemical Society* **124**, 615 (2002).
- 86 Y. Ding, Z. L. Wang, T. J. Sun, et al., *Applied Physics Letters* **90** (2007).
- 87 S. Amelinckx, X. B. Zhang, D. Bernaerts, et al., *Science* **265**, 635 (1994).
- 88 R. P. Gao, Z. L. Wang, and S. S. Fan, *Journal of Physical Chemistry B* **104**, 1227 (2000).
- 89 H. F. Zhang, C. M. Wang, E. C. Buck, et al., *Nano Letters* **3**, 577 (2003).
- 90 H. F. Zhang, C. M. Wang, and L. S. Wang, *Nano Letters* **2**, 941 (2002).
- 91 O. G. Schmidt and K. Eberl, *Nature* **410**, 168 (2001).
- 92 B. M. F. de Veubeke, *A Course in Elasticity* (Springer-Verlag, New York, 1979).
- 93 A. Volodin, M. Ahlskog, E. Seynaeve, et al., *Physical Review Letters* **84**, 3342 (2000).
- 94 A. P. Suryavanshi, M. F. Yu, J. G. Wen, et al., *Applied Physics Letters* **84**, 2527 (2004).
- 95 E. W. Wong, P. E. Sheehan, and C. M. Lieber, *Science* **277**, 1971 (1997).
- 96 X. D. Li, X. N. Wang, Q. H. Xiong, et al., *Nano Letters* **5**, 1982 (2005).
- 97 B. Wu, A. Heidelberg, and J. J. Boland, *Nature Materials* **4**, 525 (2005).

- 98 J. E. Sader, J. W. M. Chon, and P. Mulvaney, Review of Scientific Instruments **70**, 3967 (1999).
- 99 J. M. Gere, *Mechanics of Materials* (Brooks-Cole, Boston, 2001).
- 100 P. P. Benham, R. J. Crawford, and C. G. Armstrong, *Mechanics of Engineering Materials* (Essex, England, 1996).
- 101 G. Y. Jing, H. Ji, W. Y. Yang, et al., Applied Physics a-Materials Science & Processing **82**, 475 (2006).
- 102 I. Palaci, S. Fedrigo, H. Brune, et al., Physical Review Letters **94** (2005).
- 103 A. P. Borelli and O. M. Sidebottom, *Advanced Mechanics of Materials* (John Wiley & Sons, New York, 1993).
- 104 X. W. Deng, V. R. Joseph, W. J. Mai, et al., In preparation.
- 105 O. Yavas, C. Ochiai, M. Takai, et al., Applied Physics Letters **76**, 3319 (2000).
- 106 C. R. Perrey, C. B. Carter, J. R. Michael, et al., Journal of Microscopy-Oxford **214**, 222 (2004).
- 107 G. Heimel, L. Romaner, J. L. Bredas, et al., Physical Review Letters **96** (2006).
- 108 J. G. Wang and A. Selloni, Journal of Physical Chemistry A **111**, 12381 (2007).
- 109 G. Heimel, L. Romaner, E. Zojer, et al., Accounts of Chemical Research **41**, 721 (2008).
- 110 T. Toriyama, D. Funai, and S. Sugiyama, Journal of Applied Physics **93**, 561 (2003).
- 111 R. R. He and P. D. Yang, Nature Nanotechnology **1**, 42 (2006).
- 112 C. Stampfer, T. Helbling, D. Obergfell, et al., Nano Letters **6**, 233 (2006).
- 113 R. J. Grow, Q. Wang, J. Cao, et al., Applied Physics Letters **86** (2005).
- 114 N. K. Chang, C. C. Su, and S. H. Chang, Applied Physics Letters **92** (2008).
- 115 Z. Y. Zhang, C. H. Jin, X. L. Liang, et al., Applied Physics Letters **88** (2006).
- 116 Z. Y. Zhang, K. Yao, Y. Liu, et al., Advanced Functional Materials **17**, 2478 (2007).

- <sup>117</sup> S. M. Sze, *Physics of semiconductor devices* (John Wiley & Sons, New York, 1981).
- <sup>118</sup> Z. Y. Fan and J. G. Lu, *Applied Physics Letters* **86** (2005).
- <sup>119</sup> Y. Liu, M. Z. Kauser, P. P. Ruden, et al., *Applied Physics Letters* **88** (2006).
- <sup>120</sup> Y. Liu, M. Z. Kauser, M. I. Nathan, et al., *Applied Physics Letters* **84**, 2112 (2004).
- <sup>121</sup> W. Shan, M. F. Li, P. Y. Yu, et al., *Applied Physics Letters* **53**, 974 (1988).